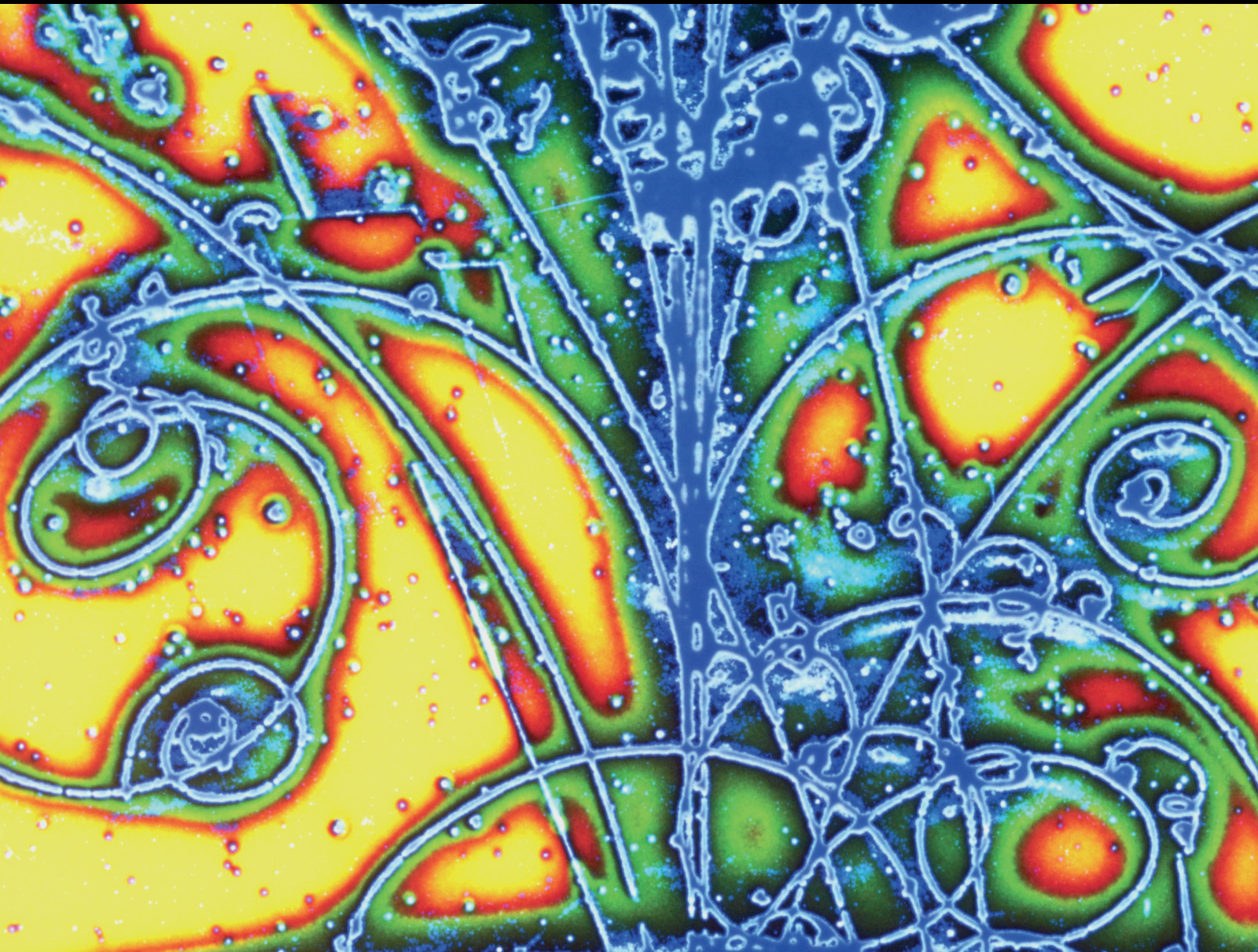


Advances in High Energy Physics

# Particle Production in Small and Large Systems at High-Energy and High-Density Frontiers

Lead Guest Editor: Fu-Hu Liu

Guest Editors: Sakina Fakhraddin, Raghunath Sahoo, Edward Sarkisyan-Grinbaum, and Bhartendu K. Singh





---

**Particle Production in Small and Large Systems  
at High-Energy and High-Density Frontiers**

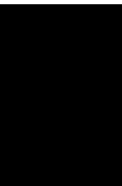
Advances in High Energy Physics

---

**Particle Production in Small and Large  
Systems at High-Energy and High-  
Density Frontiers**

Lead Guest Editor: Fu-Hu Liu

Guest Editors: Sakina Fakhraddin, Raghunath  
Sahoo, Edward Sarkisyan-Grinbaum, and  
Bhartendu K. Singh



---

Copyright © 2021 Hindawi Limited. All rights reserved.

This is a special issue published in "Advances in High Energy Physics." All articles are open access articles distributed under the Creative Commons Attribution License, which permits unrestricted use, distribution, and reproduction in any medium, provided the original work is properly cited.

# Chief Editor

Sally Seidel, USA

## Editorial Board

Antonio J. Accioly, Brazil  
Luis A. Anchordoqui, USA  
Michele Arzano, Italy  
Torsten Asselmeyer-Maluga, Germany  
Marco Battaglia, Switzerland  
Lorenzo Bianchini, Switzerland  
Roelof Bijker, Mexico  
Burak Bilki, USA  
Rong-Gen Cai, China  
Anna Cimmino, Czech Republic  
Osvaldo Civitarese, Argentina  
Andrea Coccaro, Italy  
Shi-Hai Dong, Mexico  
Mariana Frank, Canada  
Ricardo G. Felipe, Portugal  
Chao-Qiang Geng, Taiwan  
Xiaochun He, USA  
Luis Herrera, Spain  
Filipe R. Joaquim, Portugal  
Aurelio Juste, Spain  
Theocharis Kosmas, Greece  
Ming Liu, USA  
Enrico Lunghi, USA  
Salvatore Mignemi, Italy  
Omar G. Miranda, Mexico  
Grégory Moreau, France  
Piero Nicolini, Germany  
Carlos Pajares, Spain  
Sergio Palomares-Ruiz, Spain  
Yvonne Peters, United Kingdom  
Alexey A. Petrov, USA  
Luciano Petruzzello, Italy  
Thomas Rössler, Sweden  
Diego Saez-Chillon Gomez, Spain  
Takao Sakaguchi, USA  
Juan José Sanz-Cillero, Spain  
Edward Sarkisyan-Grinbaum, Switzerland  
Muhammad Farasat Shamir, Pakistan  
George Siopsis, USA  
Luca Stanco, Italy  
Jouni Suhonen, Finland  
Mariam Tórtola, Spain  
Smarajit Triambak, South Africa  
Jose M. Udías, Spain

Elias C. Vagenas, Kuwait  
Sunny Vagnozzi, United Kingdom

# Contents

## **Particle Production in Small and Large Systems at High-Energy and High-Density Frontiers**

Fu-Hu Liu , Sakina Fakhraddin , Raghunath Sahoo , Edward K. Sarkisyan-Grinbaum, and Bhartendu K. Singh

Editorial (3 pages), Article ID 9792509, Volume 2021 (2021)

## **Centrality Dependence of Chemical Freeze-Out Parameters and Strangeness Equilibration in RHIC and LHC Energies**

Deeptak Biswas 

Research Article (15 pages), Article ID 6611394, Volume 2021 (2021)

## **Transverse Momentum and Pseudorapidity Spectrum of the Top Quark, Lepton, and Jet in Proton-Proton Collisions at LHC**

Li-Na Gao  and Er-Qin Wang 

Research Article (20 pages), Article ID 6660669, Volume 2021 (2021)

## **Calculation of Binding Energy and Wave Function for Exotic Hidden-Charm Pentaquark**

F. Chezani Sharahi and M. Monemzadeh 

Research Article (6 pages), Article ID 2861214, Volume 2021 (2021)

## **Study of Production of (Anti-)deuteron Observed in Au+Au Collisions at , 62.4, and 200 GeV**

Ying Yuan 

Research Article (10 pages), Article ID 9305605, Volume 2021 (2021)

## **Event Shape and Multiplicity Dependence of Freeze-Out Scenario and System Thermodynamics in Proton+Proton Collisions at Using PYTHIA8**

Sushanta Tripathy , Ashish Bisht , Raghunath Sahoo , Arvind Khuntia , and Malavika Panikkassery Salvan 

Research Article (19 pages), Article ID 8822524, Volume 2021 (2021)

## Editorial

# Particle Production in Small and Large Systems at High-Energy and High-Density Frontiers

**Fu-Hu Liu** <sup>1</sup>, **Sakina Fakhraddin** <sup>2,3</sup>, **Raghunath Sahoo** <sup>4</sup>,  
**Edward K. Sarkisyan-Grinbaum**<sup>5,6</sup> and **Bhartendu K. Singh**<sup>7</sup>

<sup>1</sup>*Institute of Theoretical Physics, Shanxi University, Taiyuan 030006, China*

<sup>2</sup>*Physics Department, College of Sciences & Arts in Riyadh Alkhabra, Qassim University, Saudi Arabia*

<sup>3</sup>*Physics Department, Faculty of Science, Sana'a University, P.O. Box 13499, Sana'a, Yemen*

<sup>4</sup>*Department of Physics, Indian Institute of Technology Indore, Indore 453552, India*

<sup>5</sup>*Experimental Physics Department, CERN, 1211 Geneva 23, Switzerland*

<sup>6</sup>*Department of Physics, The University of Texas at Arlington, Arlington, TX 76019, USA*

<sup>7</sup>*Physics Department, Banaras Hindu University, Varanasi 221005, India*

Correspondence should be addressed to Fu-Hu Liu; fuhuli@163.com

Received 28 July 2021; Accepted 28 July 2021; Published 15 August 2021

Copyright © 2021 Fu-Hu Liu et al. This is an open access article distributed under the Creative Commons Attribution License, which permits unrestricted use, distribution, and reproduction in any medium, provided the original work is properly cited.

Particle production in small systems (proton-proton and proton-nucleus collisions) and in large systems (nucleus-nucleus collisions) at high-energy and high-density frontiers displays both similar and different behaviors. Comparing this behavior is very useful for researchers to study the properties of particle production and system evolutions. These properties are related to the signatures of the formation of a new state of matter, quark-gluon plasma (QGP), which is predicated by quantum chromodynamics (QCD). These properties are also related to the mechanisms of particle production, which are inevitably appearing in collisions.

At the high-energy frontier, the Relativistic Heavy Ion Collider (RHIC) in the Brookhaven National Laboratory (BNL) and the Large Hadron Collider (LHC) in the European Organization for Nuclear Research (CERN) provide abundant data produced in small and large systems. These data include, but are not limited to, transverse momentum spectra, anisotropic flows, statistical or dynamical fluctuations of light flavor particles, heavy flavor particles, jets, and leptons. It is expected that the effect of cold nuclei or medium affects particle production in large systems, compared with small systems.

At the high-density frontier, the beam energy scan (BES) program and its second round (BESII) and fixed target exper-

iments at the RHIC, the BES at the Super Proton Synchrotron (SPS) in CERN, the Facility for Antiproton and Ion Research (FAIR) in Germany Center for Heavy Ion Research (GSI), and others perform nucleus-nucleus collisions at high baryon number densities around the expected critical point of hadronic matter transition to QGP. It is expected that the spectra of particles are different in small and large systems at the high-density and high-energy frontiers.

In small and large systems at high-energy and high-density frontiers, the features of particle production and system evolution attract high interest and are extensively studied both experimentally and theoretically. It is believed that the properties of particle production and system evolution in small and large systems at high-energy and high-density frontiers are different. These properties are related to those of the early universe considered to go through the stages of high density and high temperature.

This special issue concerns many topics on particle production in small and large systems at high-energy and high-density frontiers, for example, (i) description of particle distributions and correlations and studies of statistical laws and dynamical properties of particle production; (ii) extraction of different quantities based on the particle spectra, correlations, and yield ratios; (iii) studies of the properties of

particle production and system evolution in small and large systems at the high-energy frontier; (iv) studies of the properties of particle production and system evolution in small and large systems at the high-density frontier; and (v) comparison of the properties of particle production and system evolution in small and large systems at high-energy and high-density frontiers.

In the article “Event Shape and Multiplicity Dependence of Freeze-Out Scenario and System Thermodynamics in Proton+Proton Collisions at  $\sqrt{s} = 13$  TeV Using PYTHIA8” by S. Tripathy et al., the authors have studied the recent observations of QGP-like conditions in high-multiplicity proton+proton (pp) collisions from the ALICE experiment at the LHC and warranted an introspection whether to use pp collisions as a baseline measurement to characterize heavy-ion collisions for the possible formation of a QGP. This article has shown that a double differential study of the particle spectra and thermodynamics of the produced system as a function of charged particle multiplicity and transverse sphericity in pp collisions would shed light on the underlying event dynamics. Transverse sphericity, one of the event shape observables, allows separating the events in terms of jetty and isotropic events. The authors analyzed the identified particle transverse momentum spectra as a function of charged particle multiplicity and transverse sphericity using Tsallis nonextensive statistics and the Boltzmann-Gibbs Blast-Wave (BGBW) model in pp collisions using the PYTHIA8 event generator. The extracted parameters such as temperature, radial flow, and nonextensive parameters are shown as a function of charged particle multiplicity for different sphericity classes. The authors observed that the isotropic events approach thermal equilibrium while the jetty ones remain far from equilibrium. Meanwhile, the authors argued that, while studying the QGP-like conditions in small systems, one should separate the isotropic events from the sphericity-integrated events, as the production dynamics are different.

In the article “Study of Production of (Anti-)deuteron Observed in Au+Au Collisions at  $\sqrt{s_{NN}} = 14.5, 62.4,$  and  $200$  GeV” by Y. Yuan, the author has studied the transverse momentum distributions of deuterons and anti-deuterons in Au+Au collisions at  $\sqrt{s_{NN}} = 14.5, 62.4,$  and  $200$  GeV with different centralities (0-10%, 10-20%, 20-40%, 40-60%, and 60-80%) in the framework of the multisource thermal model. The results show that the transverse momentum spectra are conformably and approximately described by the Tsallis distribution which is from the Tsallis nonextensive statistics and has the form satisfying the thermodynamic consistency. The dependences of the derived quantity (average transverse momenta) and the two free parameters (effective temperature and entropy index) on event centrality are obtained. It is found that the effective temperature extracted from this study increases with the decrease of centrality percentage at the same incident energy, and the entropy index decreases with the decrease of centrality percentage at the same incident energy. At the same collision centrality, the two parameters increase with the increase of incident energy. However, the kinetic freeze-out temperature and the evolution of time during the collision have yet to be studied in depth.

In the article “Calculation of Binding Energy and Wave Function for Exotic Hidden-Charm Pentaquark” by F. Chezani Sharahi and M. Monemzadeh, the authors have studied the pentaquark  $P_c(4380)$  system consisting of baryon  $\Sigma_c$  and  $\bar{D}^*$  meson. The obtained potential for the pentaquark in the literature was presented and expanded. In this study, the expanded potential was replaced with the Schrödinger equation, and that was solved as a bound state of two-body systems. By solving this to analytically approach and according to the values of constants and cutoff, 10 nonlinear differential equations and binding energy  $E_B$  of pentaquark  $P_c$  and wave function coefficients were obtained. The resulting  $E_B$  and wave function, which are presented in the form of tables and diagrams in this study, could confirm the existence of a bound state of pentaquark  $P_c(4380)$ . It is specified that the wave function plots tend to be zero at a given value. The maximum radius of pentaquark  $P_c$  was found out in the range from 23.67 to 25.64 fm. The authors observed that the calculated values match with the findings of others regarding the mass of  $P_c(4380)$ . The advantage of this study is in the methodology. In fact, other references are numerically calculated, and this study delivers the results analytically. The results obtained in this study are more comprehensive and complete compared to others.

The article “Transverse Momentum and Pseudorapidity Spectrum of the Top Quark, Lepton, and  $b$  Jet in Proton-Proton Collisions at LHC” by L.-N. Gao and E.-Q. Wang has studied the transverse momentum and pseudorapidity spectra of the top quarks and their decay products, the  $t\bar{t}$  system, and the total number of jets in proton-proton collisions at 7, 8, and 13 TeV by using the Tsallis-Pareto-type function and the three-source Landau hydrodynamic model, respectively. The related parameters, such as the effective temperature of the interacting system, the nonextensivity of the process, and the width of the pseudorapidity distribution, are extracted. This study shows that for the products, top quarks, leptons, and  $b$  jets, the width of the pseudorapidity distribution shows an increasing trend with the collision energy. The effective temperature of the interacting system shows a slight increase with the collision energy; this phenomenon may be affected by QGP. Based on the related parameters, the values of average momentum and initial temperature are calculated. Both values are very large; this could mean the high excitation degree of the interesting system.

The article “Centrality Dependence of Chemical Freeze-Out Parameters and Strangeness Equilibration in RHIC and LHC Energies” by D. Biswas has studied the centrality variation of chemical freeze-out parameters from yield data at midrapidity of charged pions, charged kaons, protons, and antiprotons for collision energies of RHIC, RHIC-BES, and LHC. The author has considered a simple hadron resonance gas model and employed a formalism involving conserved charges ( $B, Q, S$ ) of QCD for parameterization. Along with temperature and three chemical potentials ( $T, \mu_B, \mu_Q,$  and  $\mu_S$ ), a strangeness undersaturation factor ( $\gamma_S$ ) has been used to incorporate the partial equilibration in the strange sector. The obtained freeze-out temperature does not vary much with centrality, whereas the chemical potentials and  $\gamma_S$  seem to have a significant dependence. The strange hadrons are

found to deviate from a complete chemical equilibrium at freeze-out at peripheral collisions. This deviation appears to be more prominent as the collision energy decreases at lower RHIC-BES energies. The author has also shown that this departure from equilibrium reduces towards central collisions, and strange particle equilibration may happen after a threshold number of participants in large collision systems. These results can be compared with those from thermal and kinetic freeze-out.

This issue brings together a collection of articles on particle production in small and large systems at high-energy and high-density frontiers. We hope this will be a useful issue for researchers working in related areas. Meanwhile, we regret that more manuscripts submitted for publication in this issue have not been accepted following the reviewer's reports.

### **Conflicts of Interest**

The editors declare that they have no conflicts of interest regarding the publication of this special issue.

### **Acknowledgments**

We sincerely thank all authors and reviewers of this special issue.

*Fu-Hu Liu*  
*Sakina Fakhraddin*  
*Raghunath Sahoo*  
*Edward K. Sarkisyan-Grinbaum*  
*Bhartendu K. Singh*

## Research Article

# Centrality Dependence of Chemical Freeze-Out Parameters and Strangeness Equilibration in RHIC and LHC Energies

Deeptak Biswas 

Department of Physics, Center for Astroparticle Physics & Space Science Bose Institute, EN-80, Sector-5, Bidhan Nagar, Kolkata 700091, India

Correspondence should be addressed to Deeptak Biswas; [deeptakb@gmail.com](mailto:deeptakb@gmail.com)

Received 16 December 2020; Revised 31 March 2021; Accepted 9 April 2021; Published 28 April 2021

Academic Editor: Raghunath Sahoo

Copyright © 2021 Deeptak Biswas. This is an open access article distributed under the Creative Commons Attribution License, which permits unrestricted use, distribution, and reproduction in any medium, provided the original work is properly cited. The publication of this article was funded by SCOAP<sup>3</sup>.

We have estimated centrality variation of chemical freeze-out parameters from yield data at midrapidity of  $\pi^\pm$ ,  $K^\pm$  and  $p$ ,  $\bar{p}$  for collision energies of RHIC (Relativistic Heavy Ion Collider), Beam Energy Scan (RHIC-BES) program, and LHC (Large Hadron Collider). We have considered a simple hadron resonance gas model and employed a formalism involving conserved charges ( $B, Q, S$ ) of QCD for parameterization. Along with temperature and three chemical potentials ( $T, \mu_B, \mu_Q, \mu_S$ ), a strangeness undersaturation factor ( $\gamma_S$ ) has been used to incorporate the partial equilibration in the strange sector. Our obtained freeze-out temperature does not vary much with centrality, whereas chemical potentials and  $\gamma_S$  seem to have a significant dependence. The strange hadrons are found to deviate from a complete chemical equilibrium at freeze-out at the peripheral collisions. This deviation appears to be more prominent as the collision energy decreases at lower RHIC-BES energies. We have also shown that this departure from equilibrium reduces towards central collisions, and strange particle equilibration may happen after a threshold number of participants in  $A$ - $A$  collision.

## 1. Introduction

In the last few decades, several ion collider experiment collaborations have been developed to explore the phase diagram of quantum chromodynamics (QCD). Relativistic Heavy Ion Collider (RHIC) started to investigate the signatures of deconfined quark-gluon plasma, whereas the RHIC Beam Energy Scan (BES) program became motivated in searching the QCD critical point [1]. The Large Hadron Collider (LHC) is trying to investigate the medium created in zero baryon density, where a crossover transition from a hadronic state to a deconfined state of quarks and gluons may happen [2].

The hot and dense fireball created in these collisions experiences a fast expansion due to the initial pressure gradient. Assuming that the system starts from a strongly interacting quark-gluon state, a fast thermalization can occur. The thermodynamic parameters like temperature and chemical potentials can describe this thermalized medium. The matter

and energy density dilute with the expansion and the temperature declines. As the energy density (temperature) drops below the hadronization threshold, the matter evolves as a state of hadrons and their resonances. The mean free path increases with further expansion and various collisions among particles abate. In this context, one can define freeze-out as the boundary, onwards which no interaction is supposed to happen among hadrons. In the standard description, two freeze-out surfaces are described, depending on the interaction type. The chemical freeze-out (CFO) happens when inelastic scattering stops and the particle abundances become fixed. The kinetic freeze-out (KFO) is the point where elastic collisions cease. In this free noninteracting limit, the ideal hadron resonance gas model may give a reasonable description of the hadrons at freeze-out.

Yields of strange hadrons help to understand the extent of chemical equilibrium achieved in these collisions. The strange quark equilibrates later than the  $u$ ,  $d$  quarks due to

its larger mass [3]. Equilibrated strangeness spectra may be a suitable signature to understand the existence of a deconfined partonic phase [4]. Recently, a charged particle multiplicity ( $dN_{\text{ch}}/d\eta$ ) dependent production of strangeness has been observed in LHC [5]. This strangeness production is related to the collision centrality and number of participants ( $N_{\text{part}}$ ) of the collision system [6, 7]. Here,  $N_{\text{part}}$  denotes the average number of participating nucleons of a particular collision system.

Following the success of the Statistical Hadronization Model (SHM) [8], studies have determined the chemical freeze-out parameters, considering the Hadron Resonance Gas (HRG) model. In this context, a  $\chi^2$  fitting with the available yield data is well practiced [9–20]. Generally, one extracts the chemical freeze-out temperature  $T_{\text{CFO}}$  and the baryon chemical potential  $\mu_B$  by the minimization procedure, whereas the charge chemical potential  $\mu_Q$  and the strange chemical potential  $\mu_S$  get fixed from the constraints of the colliding nuclei. To scale the possible nonequilibrium of strange hadrons, a strangeness under saturation factor  $\gamma_S$  can be introduced [13, 21–27]. This parameter scales the deviation of strange hadrons from a complete equilibrium in the Grand Canonical Ensemble (GCE). In a recent work [28], we have shown that in  $\chi^2$  analysis, a larger systematic variation can arise depending on the chosen set of ratios. A conserved-charge-dependent extraction of thermal parameters has been proposed [29], which seems to suitably estimate thermal parameters and predict equilibration in the most central collision. It will be interesting to check the centrality variation of thermal parameters and the equilibration of strange particles in this framework.

In this manuscript, we have tried to study the centrality variation of freeze-out parameters, with an emphasis on the saturation of strangeness equilibration [5] in heavy nuclei collision. We have observed a similar saturation with centrality ( $N_{\text{part}}$ ) for collision energies ranging from 7.7 GeV of RHIC-BES to LHC (2.76 TeV). We have employed a recently developed parameter extraction process [29, 30] with a strangeness suppression factor  $\gamma_S$  to measure the possible deviation of strange hadrons from respective equilibrium yield. We have found the kaons to deviate from equilibrium at chemical freeze-out for the peripheral and semiperipheral collision, though the temperature does not change much with centrality. We have further studied the scaling behavior of all freeze-out parameters. The parameters attain a saturation onwards  $N_{\text{part}} = 150$ . This flattening indicates that the system created in the heavy-ion collision reaches a grand canonical limit corresponding to the most central value, in which thermodynamic description becomes independent of the system size. Finally, we have verified the efficacy of our parametrization by comparing our estimated hadron yield ratios with experimental data.

We have organized the manuscript as follows. A short description of the Hadron resonance gas model (HRG) is given in Section 2. In Section 3, we have briefly discussed the parameter extraction method in our approach. 4 describes our results followed by discussion. We summarise our results in Section 5.

## 2. Hadron Resonance Gas Model

The hadron resonance gas (HRG) model describes the system as a mixture of hadrons and their resonances. It is a standard exercise to incorporate all available hadron yields for obtaining a good description of the medium. In recent years various studies have been performed using HRG model [11, 12, 14, 31–57]. This model has successfully described hadron yields from AGS to LHC energies [11, 12, 34, 35, 37–39, 43]. Bulk properties of hadronic matter have also been studied in this model [14, 41, 42].

In the present work, we have considered the ideal HRG model in which hadrons are treated as point-like particles. A grand canonical ensemble can describe the partition function of hadron resonance gas as [14]

$$\ln Z^{\text{ideal}} = \sum_i \ln Z_i^{\text{ideal}}, \quad (1)$$

The sum runs over all hadrons and resonances. In the idealistic scenario of a chemical freeze-out, we can neglect all dissipative interactions and finite volume corrections. The thermodynamic potential for  $i$ 'th species is given as

$$\ln Z_i^{\text{ideal}} = \pm \frac{V g_i}{(2\pi)^3} \int d^3p \ln [1 \pm \exp(-(E_i - \mu_i)/T)], \quad (2)$$

where the upper sign is for baryons and lower for mesons. Here,  $V$  is the volume and  $T$  is the temperature of the system. For the  $i$ 'th species of hadron,  $g_i$ ,  $E_i$ , and  $m_i$  are, respectively, the degeneracy factor, energy, and mass, while  $\mu_i = B_i \mu_B + S_i \mu_S + Q_i \mu_Q$  is the chemical potential, with  $B_i$ ,  $S_i$ , and  $Q_i$  denoting the baryon number, strangeness, and the electric charge, respectively. For a thermalized system, the number density  $n_i$  can be calculated from partition function as

$$n_i = \frac{T}{V} \left( \frac{\partial \ln Z_i}{\partial \mu_i} \right)_{V,T} = \frac{g_i}{(2\pi)^3} \int \frac{d^3p}{\exp[(E_i - \mu_i)/T] \pm 1}. \quad (3)$$

## 3. Application to Freeze-Out

We first outline the usual application of the HRG model for characterizing the freeze-out temperature and chemical potentials in the context of heavy-ion collision experiments. The rapidity density for  $i$ 'th hadron may be related to the corresponding number density as [13]

$$\frac{dN_i}{dy} \Big|_{\text{Det}} = \frac{dV}{dy} n_i^{\text{Tot}} \Big|_{\text{Det}} \quad (4)$$

where the subscript Det denotes the detected hadrons. Here, the total number density of any hadron is

$$n_i^{\text{Tot}} = n_i(T, \mu_B, \mu_Q, \mu_S) + \sum_j n_j(T, \mu_B, \mu_Q, \mu_S) \times \text{Branch Ratio}(j \rightarrow i). \quad (5)$$

The summation is over the heavier resonances ( $j$ ) that decay to the  $i^{\text{th}}$  hadron. This number density  $n_i$  is calculated using Eq. (3).

In this context, it is also important to consider the constraints regarding the conserved charges. Following the assumption of an isentropic evolution, one can employ conservation conditions like strangeness neutrality (Eq. (6)) and baryon density to charge density (Eq. (7)) to restrict the values of chemical potentials [16].

$$\sum_i n_i(T, \mu_B, \mu_S, \mu_Q) S_i = 0, \quad (6)$$

$$\sum_i n_i(T, \mu_B, \mu_S, \mu_Q) Q_i = r \sum_i n_i(T, \mu_B, \mu_S, \mu_Q) B_i. \quad (7)$$

Here,  $r$  is the net-charge to net-baryon number ratio of the colliding nuclei. For example, in Au + Au collisions,  $r = N_p / (N_p + N_n) = 0.4$ , with  $N_p$  and  $N_n$  denoting the number of protons and neutrons in the colliding nuclei. In a proton-proton collision, this ratio is 1.

The usual approach should be solving Eq. (4) to extract thermal parameters. The freeze-out description will be more reasonable if we include data for a larger number of detected particles in our solving mechanism. So a  $\chi^2$  minimization is performed with all the available yields. One may avoid the volume systematics by taking ratios of two hadrons. In this approach, the effects of hydrodynamical flow also disappear [38]. Further, performing a minimization procedure with available yield ratios, one can parameterize the chemical freeze-out surface. In a recent work Ref. [28], we have shown that significant systematic uncertainty may arise in  $\chi^2$  analysis due to variation in the chosen set of ratios.

**3.1. Our Approach.** Following the complication regarding the chosen set of ratios, we have introduced an alternative method in Ref. [29]. The individual hadrons are not a conserved quantity in the strong interaction. So we opted to introduce ratios regarding conserved net charge densities like  $B$ ,  $Q$ ,  $S$ . Along with the constraints Eqs. (6) and (7), we have proposed two new independent equations, the net baryon number normalized to the total baryon number and the net baryon number normalized to the total hadron yield [58], as given below.

$$\frac{\sum_i^{\text{Det}} B_i (dN_i/dY)}{\sum_i^{\text{Det}} |B_i| (dN_i/dY)} = \frac{\sum_i^{\text{Det}} B_i n_i^{\text{Tot}}}{\sum_i^{\text{Det}} |B_i| n_i^{\text{Tot}}}, \quad (8)$$

$$\frac{\sum_i^{\text{Det}} B_i (dN_i/dY)}{\sum_i^{\text{Det}} (dN_i/dY)} = \frac{\sum_i^{\text{Det}} B_i n_i^{\text{Tot}}}{\sum_i^{\text{Det}} n_i^{\text{Tot}}}. \quad (9)$$

We want to mention that the left-hand side consists of the particle yields data from the heavy-ion collision, and those on the right are the number densities calculated from the thermal HRG model.  $i$  runs only over detected (Det) hadrons with available experimental yield data.

**3.2. Application to Centrality.** The geometric information of the collision system is crucial to understand, as different final

observables like eccentricity, elliptical flow, and charge particle multiplicity are directly dependent on the initial conditions like impact parameter ( $b$ ), the number of participating nucleons ( $N_{\text{part}}$ ) [59]. We employ the centrality bins to differentiate collision events according to their impact parameters. As there is no direct method to measure  $b$ , the centrality bins can be calibrated from charge particle multiplicity with the Glauber model [6, 59, 60]. Each centrality bin is represented by a corresponding  $N_{\text{part}}$ . Most central (0% – 5% centrality) collisions correspond to the events with the lowest value of impact parameters (highest value of  $N_{\text{part}}$ ), whereas the most peripheral (70% – 80%) are with the largest impact parameter and smallest  $N_{\text{part}}$ . The degree of equilibration of the created medium should strongly depend on centralities as the system's initial volume and initial energy, baryon deposition depends on these initial specifications.

**3.3. Strangeness with Centrality.** Introducing a strangeness suppression factor is optional for the most central collisions [28, 29], whereas this appears essential when we deal with a peripheral or semicentral collision. Complete chemical equilibrium may not be achieved in the strangeness sector due to the higher mass threshold of strange particles and their hadronic counterpart [3]. Initially, this suppression factor  $\gamma_S$  was introduced considering the phase space undersaturation [22]. Ref. [23, 24] has discussed this undersaturation as an effect of the canonical ensemble consideration of strangeness, where exact strangeness conservation should be considered for a smaller collision system. In Ref. [61], a core corona-dependent model has also tried to discuss this suppression of strangeness. Irrespective of the reason for this undersaturation, considering this factor  $\gamma_S$ , gives rise to a better agreement to the thermal description of heavy-ion data. It seems that the strange sector may have a deviation from the respective grand canonical picture, and this parameter is a measure of that departure [13, 21–27]. In the presence of this factor, the number density is modified in the following manner [13]:

$$n_i = \frac{g_i}{(2\pi)^3} \int \frac{d^3p}{\gamma_S^{-n_i} \exp[(E_i - \mu_i)/T] \pm 1}. \quad (10)$$

Here,  $n_i^s$  denotes the number of valence strange quarks or antiquarks in the  $i^{\text{th}}$  hadron. In this work, we have calculated the number densities following 10.  $\gamma_S = 1$  for all non-strange particles. A smaller value of  $\gamma_S$  denotes a larger deviation from the grand canonical limit of equilibrium.

As we have introduced one added parameter  $\gamma_S$ , an extra equation is needed to close our system of equations. This parameter is not related to any conserved quantity, rather it is used to describe the possible nonequilibrium of the strange sector. Keeping in mind that we have used only yields of kaons among the strange particles, we have utilized kaon to pion ratio to evaluate the value of  $\gamma_S$  in Eq. (11).

$$\sum_i \frac{(K/\pi)_{\text{expt}}^i - (K/\pi)_{\text{model}}^i}{(K/\pi)_{\text{model}}^i} = 0. \quad (11)$$

Here,  $i$  stands for two possible charges, i.e.,  $(K/\pi)^+ = K^+/\pi^+$  and  $(K/\pi)^- = K^-/\pi^-$ . Here, we want to reiterate that, for smaller system size (peripheral collisions), the exact strangeness conservation demands the canonical treatment. To study the systematic variation with centrality, we have approached within a Grand Canonical Ensemble (GCE) with the  $\gamma_S$  to scale the possible deviation from equilibrium picture. This exercise is well practiced in the context of freeze-out parameter extraction for various centrality [25–27, 62–65]. Finally, we have solved all these five equations Eq. (6)–(9) and Eq. (11) to extract the five parameters ( $T$ ,  $\mu_B$ ,  $\mu_Q$ ,  $\mu_S$ , and  $\gamma_S$ ).

These three quantities are independent so as the constructed total charges. So the correlated uncertainties, arising from repeated entries of a single yield (addressed in Ref. [66]), are reduced in this formalism.

In this analysis, we have used yield data of  $\pi^\pm$ ,  $K^\pm$ , and  $p, \bar{p}$ . In this context, netB can be constructed out of net-pion, whereas net charge is the sum of net-pion, net-kaon, and net-proton. This consideration is in line with the general approximation of taking the net proton as a proxy for net baryon number [67]. For these set of particles, the abovementioned equations will be

$$\begin{aligned} \frac{dN_p/dY - dN_{\bar{p}}/dY}{(dN_p/dY) + (dN_{\bar{p}}/dY)} &= \frac{n_p^{\text{Tot}} - n_{\bar{p}}^{\text{Tot}}}{n_p^{\text{Tot}} + n_{\bar{p}}^{\text{Tot}}} \frac{dN_p/dY - dN_{\bar{p}}/dY}{(dN_{\pi^+}/dY) + (dN_{\pi^-}/dY) + (dN_{K^+}/dY) + (dN_{K^-}/dY) + (dN_p/dY) + (dN_{\bar{p}}/dY)} \\ &= \frac{n_p^{\text{Tot}} - n_{\bar{p}}^{\text{Tot}}}{n_{\pi^+}^{\text{Tot}} + n_{\pi^-}^{\text{Tot}} + n_{K^+}^{\text{Tot}} + n_{K^-}^{\text{Tot}} + n_p^{\text{Tot}} + n_{\bar{p}}^{\text{Tot}}}. \end{aligned} \quad (12)$$

Here, the  $n_i^{\text{Tot}}$  denotes the total number density of  $i$ 'th particles, considering the relevant decay channels. We have considered all the strong decay channels from higher mass resonances, whereas weak decay corrections have been performed depending on the experimental specification [6, 66, 68]. In LHC, we have not included weak decay contribution into protons, whereas in RHIC energies, they are present in the total density.

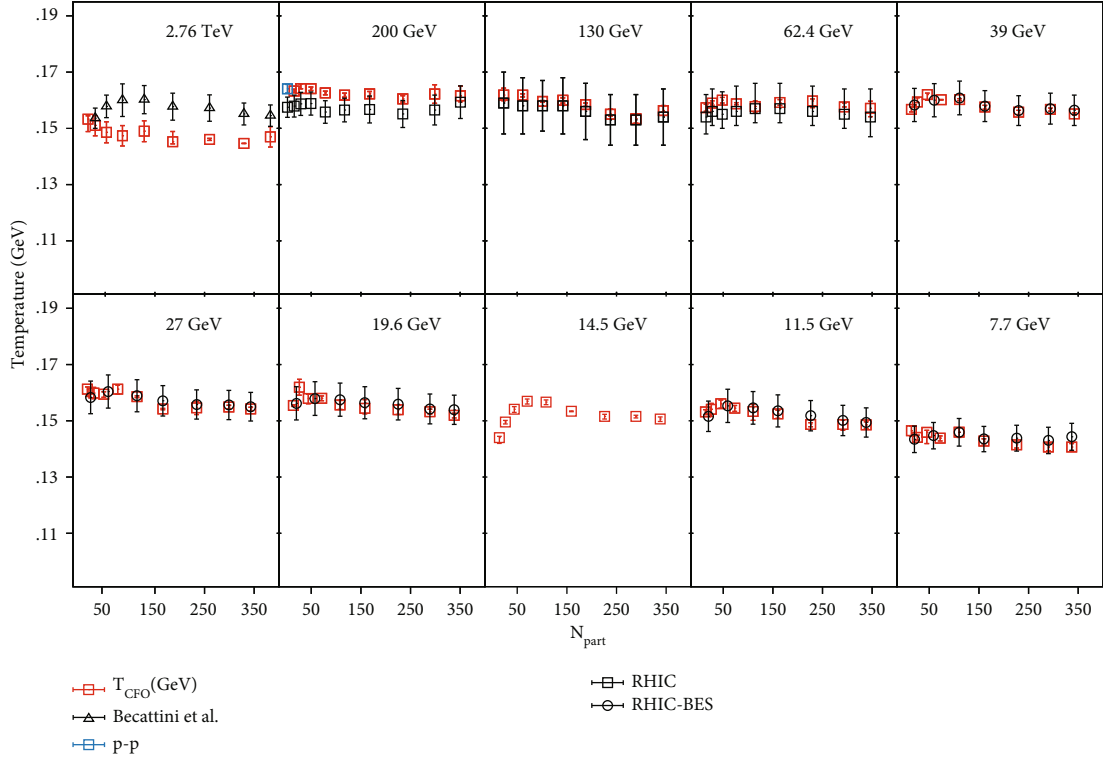
## 4. Results and Discussions

In this analysis, we have used the yields of  $\pi^\pm$  (139.57 MeV),  $K^\pm$  (493.68 MeV), and  $p, \bar{p}$  (938.27 MeV) for collision energies ( $\sqrt{s_{NN}}$ ) ranging from RHIC-BES (7.7 GeV) to LHC (2.76 TeV). For convenience, we have represented the centrality bins by their corresponding number of participants ( $N_{\text{part}}$ ). The collision system is Au-Au at higher RHIC and RHIC-BES energies and Pb-Pb at LHC. Data have been used following RHIC [6], RHIC-BES [66, 69], and LHC [68]. Data for  $p$ - $p$  collision is available in RHIC for  $\sqrt{s_{NN}} = 200$  GeV and included in our analysis for completeness. In the present analysis, we have only taken midrapidity data. The details of the experimental yields used in the analysis are listed in Ref. [6, 66, 68, 69].

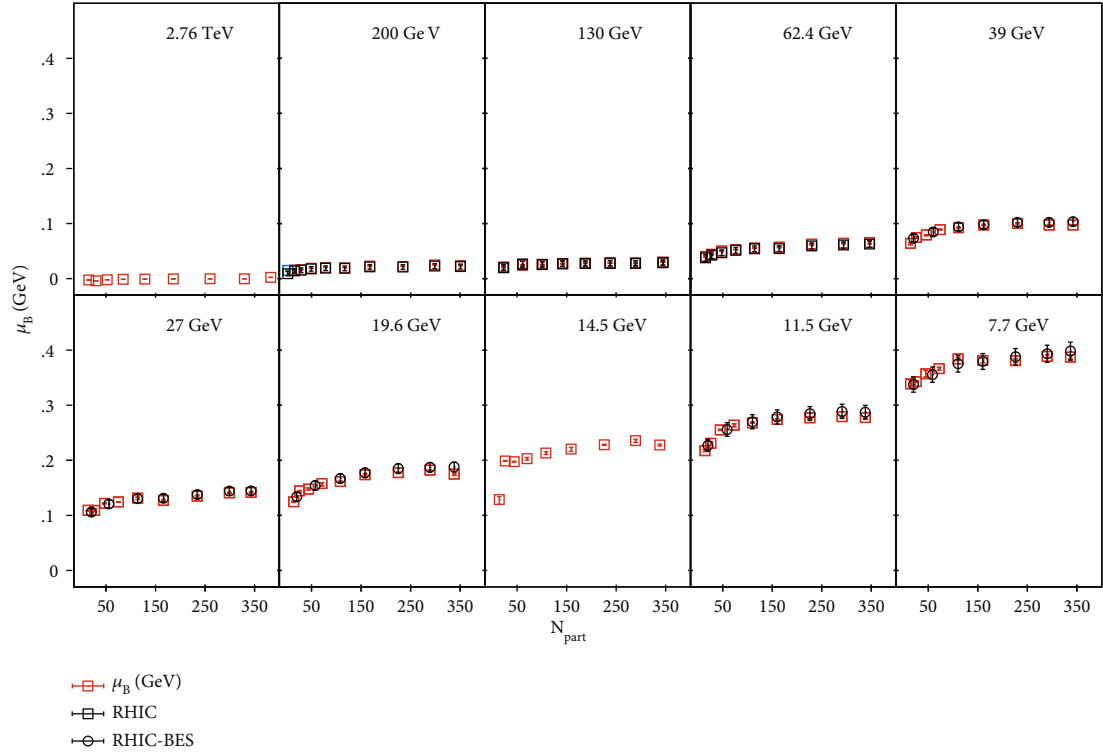
In our HRG spectrum, we have used all confirmed hadrons up to 2 GeV, with masses and branching ratios following the Particle Data Group [70] and THERMUS [71], which is a numerical thermal model package for the root framework. Finally, we solve Eqs. (6)–(9) and (11) numerically, using Broyden's method with a minimum convergence criterion of  $10^{-6}$  [72]. We have estimated the variances of thermal parameters by repeating the analysis at the given extremum value of hadrons yields.

**4.1. Freeze-Out Parameters.** We have described the variation of our extracted freeze-out parameters with the number of participants ( $N_{\text{part}}$ ) for various collision energies in Figures 1(a), 1(b), 2(a), 2(b), and 3. In plots, the horizontal axis is the number of participants. Results for collision energy LHC-2.76 TeV to RHIC-BES-7.7 GeV have been shown in different columns in descending order from left to right. For the clarity of discussion, we shall discuss variation concerning  $\sqrt{s_{NN}}$  first and then try to understand the changes with centrality. For completeness, we have also presented available results for  $T_{\text{CFO}}$ ,  $\mu_B$ , and  $\gamma_S$  from other studies alongside our findings. We have included results from Ref. [6, 66] for RHIC and RHIC-BES and Ref. [73] for LHC.

The variation of the chemical freeze-out temperatures ( $T_{\text{CFO}}$ ) in Figure 1(a) has good agreement with general understanding [29]. At most central collisions, the freeze-out temperature increases with collision energy, and near  $\sqrt{s_{NN}} = 39$  GeV saturates around the value of 160 MeV as it reaches the Hagedorn limit [74]. At LHC,  $T_{\text{CFO}}$  is lower than the expected value as the proton yield is lower than their preceding RHIC energies [68]. The freeze-out temperatures seem to have a weaker dependence on the centrality and appear to be independent of  $N_{\text{part}}$  and maintains a flat pattern at all collision energies. For  $\sqrt{s_{NN}} = 14.5$  GeV, the variation of  $T_{\text{CFO}}$  is a little different at peripheral bins. The horn-like behavior is arising from a relatively lower yield of the proton (evident from the ratio  $\bar{p}/p$  and  $p/\pi^+$ ), which also reflects in the extracted values of  $\mu_B$ . There is good agreement with other results (black points) for  $T_{\text{CFO}}$ . In Ref. [6, 66], the parametrization has been performed utilizing only pion, kaon, and proton. Results from these analyses match with our findings, whereas the little differences in LHC energy may arise from the fitting procedure and particle species used for fitting.

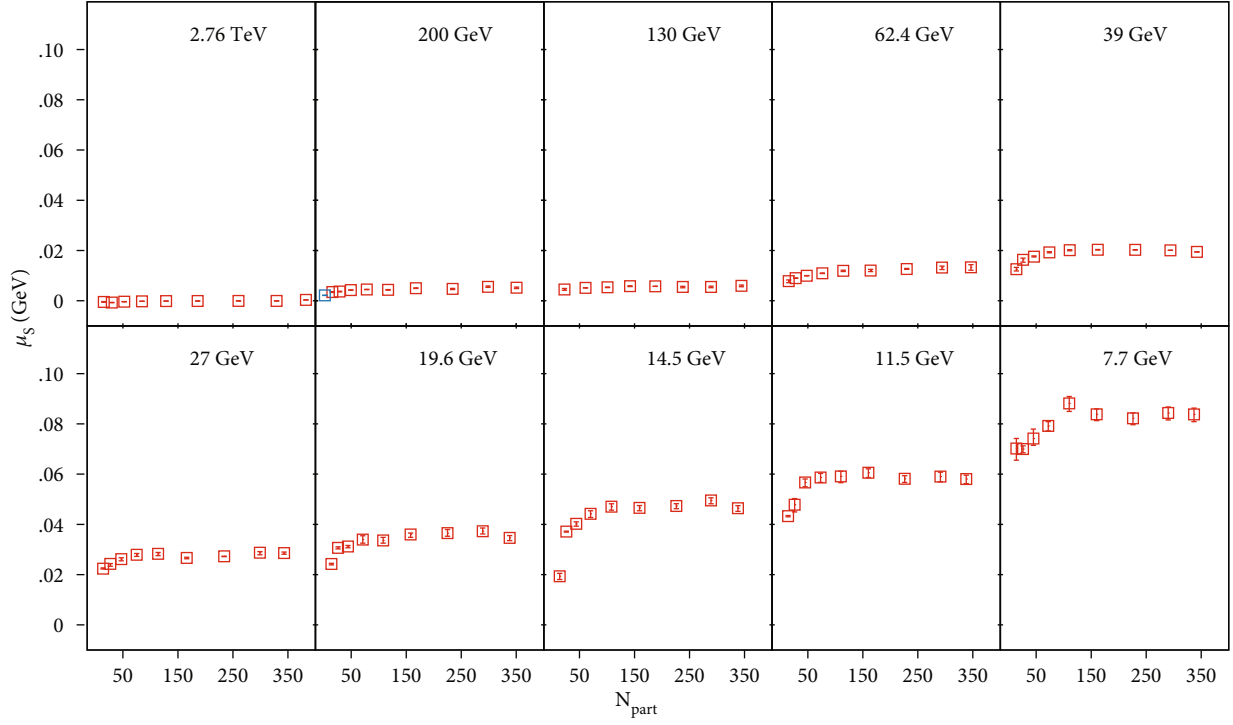


(a)



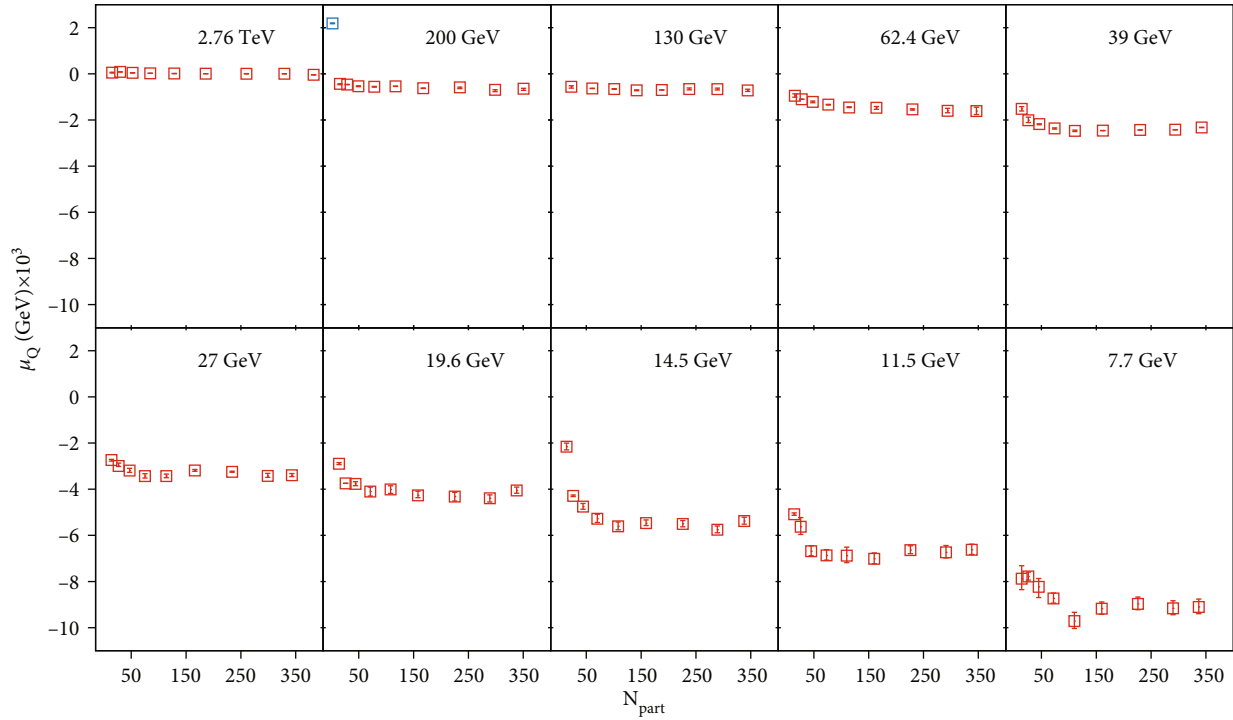
(b)

FIGURE 1: (Color online) variation of  $T_{CFO}$ ,  $\mu_B$  with  $N_{part}$  for representative collision energies. Each column stands for different collision energy, ranging from LHC (2.76 TeV) to RHIC-BES (7.7 GeV). Most central collision (0% – 5%) is denoted by the highest value of  $N_{part}$ , lowest value denotes the peripheral collision (70% – 80%). Red squares denote results for Pb-Pb at LHC and Au-Au at RHIC and BES. Blue square points analysis for  $p$ - $p$  collision of RHIC-200 GeV. Results from available literature have been included in the following Ref. [73] for LHC (black triangle), Ref. [6] for RHIC (black square), and Ref. [66] for RHIC-BES (black circle).



—■—  $\mu_S$  (GeV)

(a)



—■—  $\mu_Q$  (GeV)  $\times 10^3$

(b)

FIGURE 2: (Color online) variation of  $\mu_S$ ,  $\mu_Q$  with  $N_{\text{part}}$  for representative collision energies. The red square denotes results for Pb-Pb at LHC and Au-Au at RHIC and BES. Blue square points analysis for the  $p$ - $p$  collision of RHIC-200 GeV.

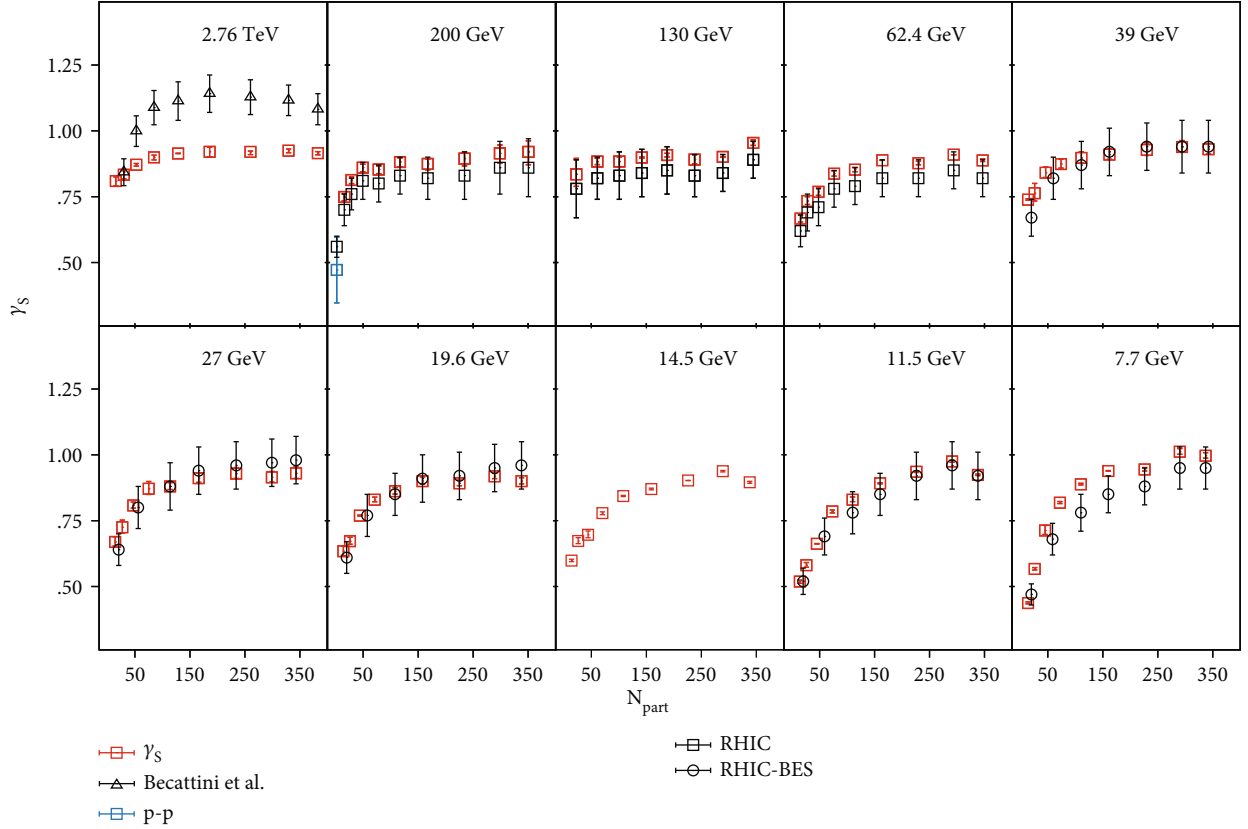


FIGURE 3: (Color online) variation of  $\gamma_s$  with  $N_{part}$  for representative collision energies. Each column stands for different collision energy, ranging from LHC (2.76 TeV) to RHIC-BES (7.7 GeV). Most central collision (0% – 5%) is denoted by the highest value of  $N_{part}$ , lowest value denotes the peripheral collision (70% – 80%). Red square denotes results for Pb-Pb at LHC and Au-Au at RHIC and BES. Blue square points analysis for  $p$ - $p$  collision of RHIC-200 GeV. Results from available literature have been included in the following Ref. [73] for LHC (black triangle), Ref. [6] for RHIC (black square), and Ref. [66] for RHIC-BES (black circle).

We have plotted the baryon chemical potential as a function of  $N_{part}$  for all  $\sqrt{s_{NN}}$  in Figure 1(b). The general expectation is that at lower collision energies, a larger amount of nucleons deposit in the collision region due to the baryon stopping [75, 76]. But at very high collision energies, the nuclei are transparent to each other [77, 78]. So at higher RHIC and LHC energies, the medium is created having almost zero net baryon number. Therefore, the net baryon density and hence the estimated chemical potential  $\mu_B$  would decrease with increasing  $\sqrt{s_{NN}}$  due to baryon transparency [78]. In the same manner, one should expect a rise of  $\mu_B$  for higher  $N_{part}$ . In central collisions, the value of the deposited net baryon number increases due to baryon stopping among a large number of the participating nucleons. Contrarily for a peripheral collision, a lesser number of nucleons get deposited in the collision zone, creating a dilute system of net baryon, which results in a smaller value of  $\mu_B$ . We have observed this trend in all  $\sqrt{s_{NN}}$ . Our resulted  $\mu_B$  agrees with previous findings from Ref. [6, 66].

Strangeness chemical potential  $\mu_s$  shows a similar trend as  $\mu_B$  in Figure 2(a). It decreases as collision energy increases and becomes zero at LHC energy. On the other hand,  $\mu_s$  escalates as one goes from peripheral to the central collision. The correlation between  $\mu_s$  and  $\mu_B$  can be described in the

following manner. A higher baryon density demands hyperons to be produced more than antihyperons. To maintain the strange neutrality, this excess amount of strangeness from the baryonic sector has to be nullified from the mesonic sector. So in the mesonic sector,  $K^+$  is more abundant than  $K^-$ . Being the lightest strange particles, this difference between charged kaons determines the sign and trend of  $\mu_s$ .

The general trend of charge chemical potential  $\mu_Q$  is the same as other  $\mu_s$  except for the sign. As  $N_{part}$  increases, it becomes more negative and the magnitude decreases with  $\sqrt{s_{NN}}$  in Figure 2(b). However,  $\mu_Q$  is more negative for larger baryon densities. We can understand this as following. The neutrons are more abundant than protons in the colliding heavy nuclei. This abundance generates a net negative isospin value in the collision system and produces more  $\pi^-$  than  $\pi^+$ , to conserve the isospin. As the lightest charged particle, these pions determine the negative  $\mu_Q$ . This reasoning will be more clear if we look into the value of  $\mu_Q$  for  $\sqrt{s_{NN}} = 200$  GeV at  $N_{part} = 2$ . In this case of  $p$ - $p$  collision, the isospin dominance should not act in favor of  $\pi^-$ , as there is no neutron in the colliding particles. So one should expect the  $\mu_Q$  to be positive for this case. Indeed, we have observed a positive value of  $\mu_Q$  for the  $p$ - $p$  collision of 200 GeV RHIC energy. The net value of

isospin increases with the  $N_{\text{part}}$ , thus increases asymmetry between the yield of charged pions. So the magnitude of  $\mu_Q$  rises following the  $\mu_B$ .

If strange particles achieve chemical equilibrium, then the thermal abundance of kaons should be described by equilibrium thermal parameters ( $T, \mu_s$ ) of a grand canonical ensemble. This is not observed in cases of a small collision system like  $p$ - $p$ ,  $p$ - $A$ , and even in  $A$ - $A$  with a smaller  $N_{\text{part}}$  [13]. Several models [23–25, 62, 64] have tried to describe this source of strangeness undersaturation in the smaller system and advocated the use of  $\gamma_s$ . The common perception from all this work is that  $\gamma_s$  scales the deviation of strange particles from their respective equilibrium thermal yield of a grand canonical ensemble, while  $\gamma_s = 1$  denotes the equilibration in the strange sector.

We have shown the variation of  $\gamma_s$  in Figure 3. It is interesting to notice that even in LHC and high RHIC energies, the  $\gamma_s$  has an increasing trend from lower peripheral to a central collision, though the temperature and other chemical potentials do not change much. Initially, it starts from a lower value in the case of peripheral collisions and increases with participants. Around  $N_{\text{part}} = 150$ ,  $\gamma_s$  tends to saturate to the most central values. It appears that the strangeness tends to be closer to the grand canonical limit as the system size increases. The saturation of  $\gamma_s$  with the colliding system size for central  $A$ - $A$  collisions suggests that the strangeness suppression may be independent of the hadronic scatterings, which happens in the later time of the evolution [62]. From the pattern, one can also conclude that the strangeness equilibration has a prominent dependence on the number of participants and system volume. The differences between the values between peripheral and central are larger for lower RHIC-BES energies. The general understanding from the above study is that the strangeness sector may be closer to equilibrium in a peripheral collision of higher  $\sqrt{s_{NN}}$ , whereas the deviation from equilibrium is larger for peripheral cases in lower collision energy. We have found that strangeness equilibration tends to happen in collisions with a  $N_{\text{part}}$  more than 150, which may be the threshold  $N_{\text{part}}$  for the creation of a deconfined phase in a  $A$ - $A$  collision, which drives the system close to strangeness equilibration [3].

We want to mention that even at high RHIC and LHC energies, the central value of  $\gamma_s$  lies below 1 (around 0.9). This finding is in agreement with previous analyses from RHIC collaboration [6, 66]. In Ref. [66], the  $\gamma_s$  is shown to increase and saturate near 1 as more hyperon species are included in chemical freeze-out parametrization. In this context, our method would be similar to the standard chi-square analysis, where the parameterization depends on the chosen hadronic ratios. Future studies with other heavy ions and data of hyperons may help to understand this.

**4.2. Scaling Nature of CFO Parameters.** The scaling behavior with  $N_{\text{part}}$  is important to calibrate the chemical composition at freeze-out with system size. To simplify the discussion, we have normalized the obtained parameters by their corresponding value for the most central collision of individual

$\sqrt{s_{NN}}$ . As an example, to understand the scaling of temperature at 200 GeV, we have divided the extracted  $T_{\text{CFO}}$  of each centrality bin ( $N_{\text{part}}$ ) with that of the most central collision (maximum  $N_{\text{part}}$ ). Figure 4 shows the variation for all five freeze-out parameters. For simplicity, we have plotted for two collision energies from both RHIC (200, 62.4) and RHIC-BES (27, 11.5). These scaled quantities should lie around 1 if parameters do not vary much with centrality ( $N_{\text{part}}$ ). The scaled freeze-out temperature shows this pattern for all collision energies. It seems that for given incident energy, the freeze-out temperature does not vary much with the system size, whereas the scaled baryon chemical potential ( $\mu_B$ ) has an increasing trend as it becomes maximum at most central collisions. In the case of equilibrium among all the charges, all the chemical potentials should commensurate with each other. Scaled  $\mu_Q$  and  $\mu_s$  should follow the pattern of  $\mu_B$  with both the number of participants and collision energy, which we have already discussed in Section 4.1. We have indeed observed a similar trend for all three  $\mu_s$ . There is a trend of saturation near 1 around  $N_{\text{part}} = 150$ . Onward this point, the system may achieve a thermodynamical state which is independent of the system size. Future analysis with other colliding ions at these c.m energies may shed light on this issue. Nontriviality could have appeared in the case of  $\gamma_s$  as it is a nonequilibrium parameter. But the observed trend is similar to the chemical potentials. It starts from a smaller magnitude and saturates onward  $N_{\text{part}} = 150$ . The system may have enough energy and number density for strangeness equilibration onward this centrality bin [79], and we can employ a grand canonical description to describe the yield at freeze-out. The deviation of scaled  $\gamma_s$  from central value is larger for peripheral collisions in lower RHIC-BES energy, which indicates that colliding energy has a crucial contribution to decide the equilibration of strangeness.

**4.3. Particle Yield Ratios.** In this section, we shall discuss ratios regarding detected particles to check the efficiency of our parameterization. We have estimated particle ratios from our extracted freeze-out parameters and plotted them alongside their experimental values. Variances in the detected yield ratios have been obtained using the standard error propagation method [80], considering both the systematic and statistical uncertainties of data. We have calculated the variance of thermally estimated ratios by evaluating them at the extrema of the obtained freeze-out parameters.

In Figure 5(a), we have plotted the particle to antiparticle ratios for pions and kaons. There is good agreement between model estimation and experimental data for both ratios. No notable variation has been observed for  $\pi^-/\pi^+$  with  $N_{\text{part}}$  and  $\sqrt{s_{NN}}$ . Freeze-out temperature and  $\mu_Q$  determine the chemical abundance of pions. For the ratio of negatively charged to positively charged pions, the variation should depend on  $\mu_Q$  only. Here, we want to mention that there is no prominent variation of  $\mu_Q/T_{\text{CFO}}$  with  $\sqrt{s_{NN}}$  and  $N_{\text{part}}$ , as the value of  $\mu_Q$  is much smaller (around 5 MeV) than the value of  $T_{\text{CFO}}$  (about 150 MeV). On the other hand,  $\mu_Q$  is much lower than the mass of the pion itself. So it does not

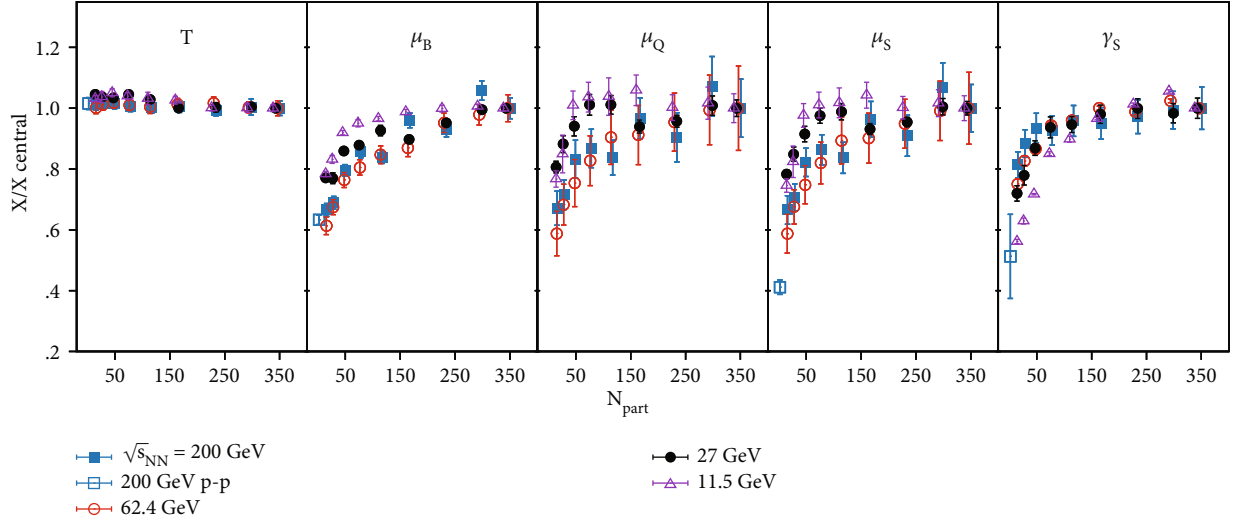


FIGURE 4: (Color online) scaling behavior of various parameters with  $N_{\text{part}}$ . Representative points are for collision energies RHIC (200 GeV, 62.4 GeV) and RHIC-BES (27 GeV, 11.5 GeV). Different columns denote different scaled parameters.

differentiate between the thermal yield of  $\pi^-$  and  $\pi^+$ , and the ratio lies near unity for all collision energies and centrality classes.

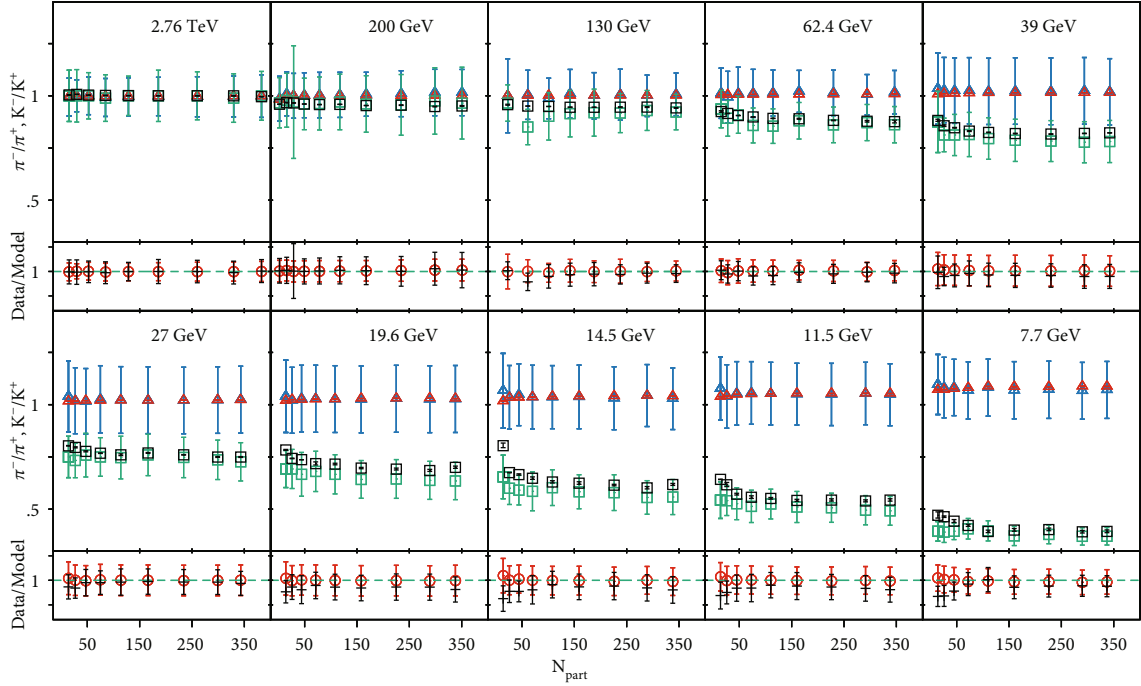
The asymmetry between  $K^-$  and  $K^+$  depends on net baryon density and net strangeness from the hyperon sector. One should expect a larger yield of  $K^+$  than  $K^-$  at higher baryon density ( $\mu_B$ ). We have observed this pattern with both centrality and  $\sqrt{s_{NN}}$ . At lower RHIC-BES energies, the ratio is far from unity due to higher net baryon density and approaches 1 as the collision energy increases. The yields of particle and antiparticle become equal at LHC as baryon transparency takes over, and the medium starts with zero net baryon density. With  $N_{\text{part}}$ , a commensurable trend has been observed following the value of  $\mu_B$ . At peripheral bins of lower collision energies, our model has overestimated the  $K^-/K^+$  ratio. This overestimation has occurred as an interplay between the  $\bar{p}/p$  ratio and the constraint  $\text{NetS} = 0$ . The  $\mu_B$  decreases towards peripheral and noncentral collision following the  $\bar{p}/p$  ratio, which results in a lower density of  $\Lambda$  and other hyperons. On the other hand, to maintain the strangeness neutrality, thermal parameters adjust to produce a larger thermal density of  $K^-$ , which results in this overestimation.

The charge independent  $K/\pi$  ratios  $K^+/\pi^+$ ,  $K^-/\pi^-$  are important observables for understanding the strangeness production in high-energy collisions. As the lightest mass hadrons, pions may act as the proxy of entropy, whereas the kaons carry the signature of strangeness. Strange particles are important in studying chemical equilibrium in heavy-ion collisions due to their late production [3]. A charged particle multiplicity ( $dN_{\text{ch}}/d\eta$ ) dependent saturation of strangeness normalized to pions has already been observed in LHC [5], which can be utilized to investigate the system size-dependent strangeness production. Ref. [79] has related this saturation to equilibration with a threshold  $dN_{\text{ch}}/d\eta$ . In heavy nuclei collisions, the overlap region and  $dN_{\text{ch}}/d\eta$  both are related to  $N_{\text{part}}$  [6]. We have observed the same saturation trend with  $N_{\text{part}}$  here for all  $\sqrt{s_{NN}}$  in Figure 5(b) and have

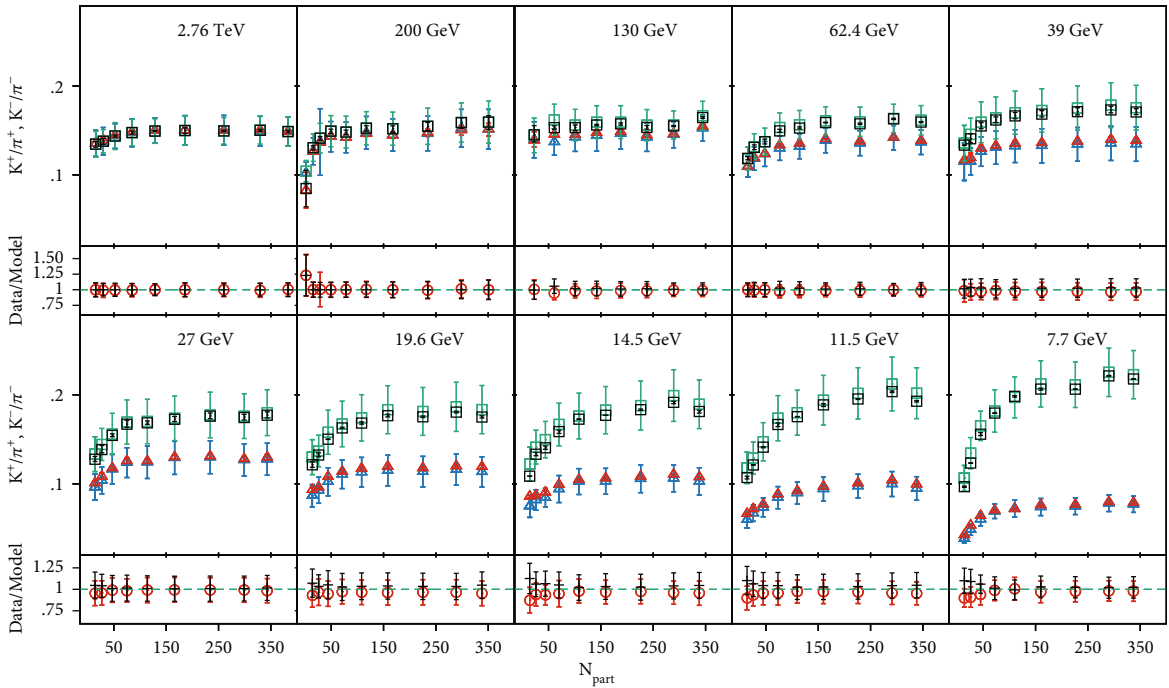
suitably reproduced it with our parametrization. This saturation starts around  $N_{\text{part}} = 150$  in higher RHIC and LHC. Here, we want to mention that there is no variation of  $\pi^-/\pi^+$  with centrality and collision energy, but  $K^-/K^+$  has a strict dependence on both. At lower collision energy,  $K^+/\pi^+$  is much higher than  $K^-/\pi^-$  due to the excess yield of  $K^+$ . The difference between the ratios decreases with increasing collision energies, and they become equal at LHC, as the particle-antiparticle yields become the same. The pattern of  $\gamma_S$  has a close resemblance to both the ratios. It seems that as  $N_{\text{part}}$  decreases, the kaon yields deviate far from their equilibrium yield. So a nonequilibrium parameter  $\gamma_S$  had to be introduced in our thermal model. Lower the value of  $\gamma_S$ , larger is the deviation from equilibrium for kaons.

Here, we want to reemphasize that both  $K^-/K^+$  and  $\pi^-/\pi^+$  have no significant variation with centrality bins at LHC. This symmetry between particle and anti-particle demands  $\mu_Q$  and  $\mu_S$  to be almost zero. A centrality variation in the  $K/\pi$  ratio cannot be reproduced with zero  $\mu$  without introducing a  $\gamma_S$  like parameters. This centrality variation of the  $K/\pi$  ratio indicates that the strange particles are out of equilibrium at peripheral collisions of LHC.

From the discussion of freeze-out parameters, it appears that the variation of antiproton (anti baryon) to proton (baryon) is a guideline to understand the variation of  $\mu_B$ . This ratio becomes 1 at upper RHIC and LHC energies as the colliding nuclei pass through each other, and the hadrons are created out of a medium having zero net baryon density. In lower collision energy, baryon stopping motivates a larger net baryon density. As a result, protons are more abundant than antiproton and advocate a smaller  $\bar{p}/p$  at lower collision energy. Our thermal model estimations have good agreement with the experimental data in Figure 6(a). Towards peripheral collisions, this ratio tends to increase and symbolizes the decrease of baryon dominance over antibaryons. Initial net baryon number density decreases as one goes from central to peripheral collision due to nuclear distribution [81]

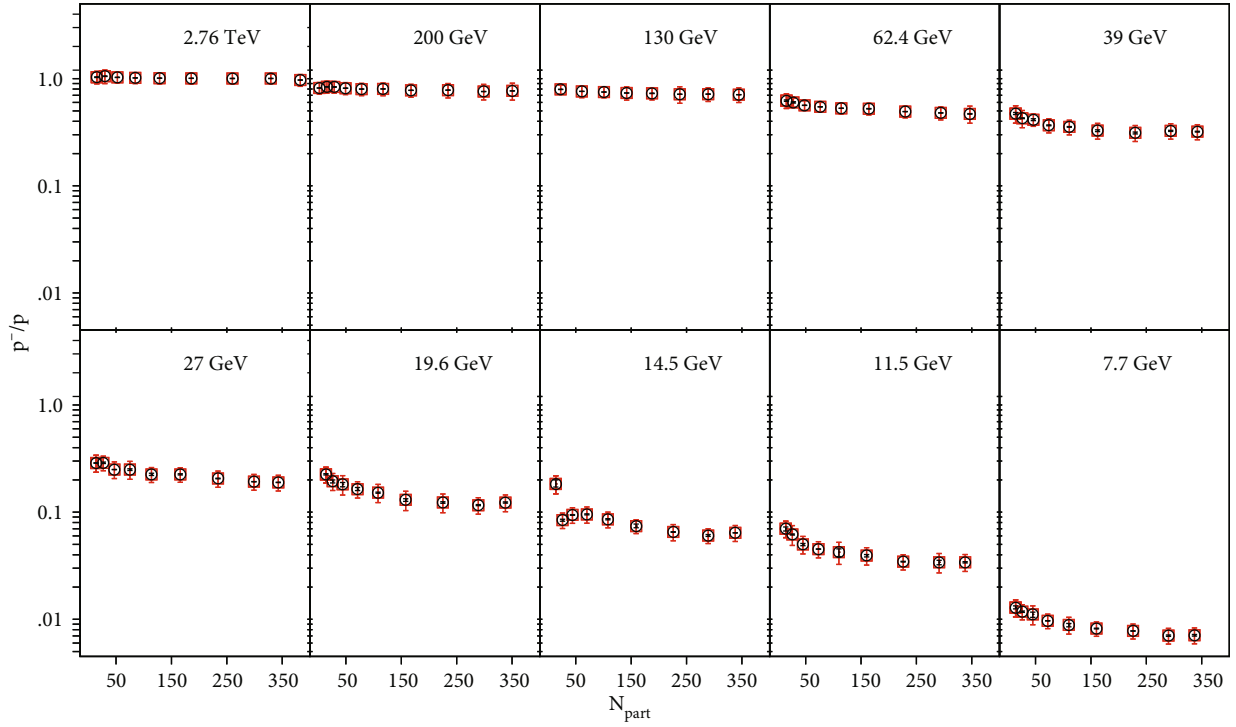


(a)



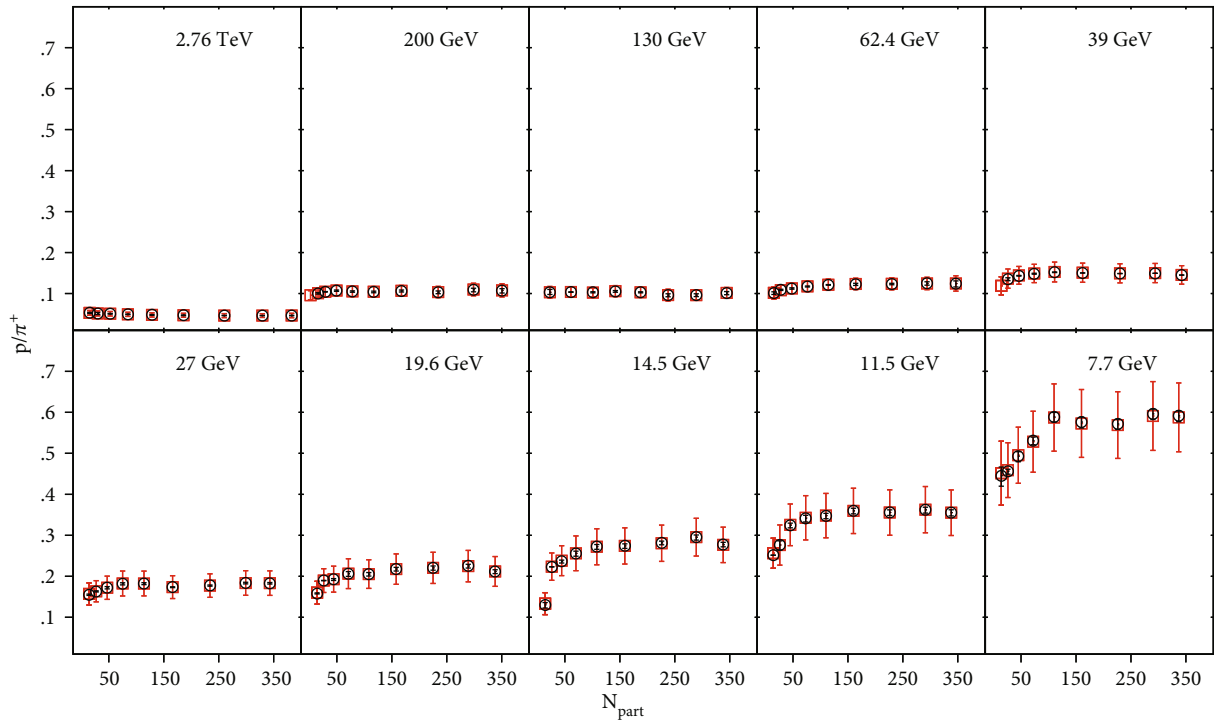
(b)

FIGURE 5: (Color online)  $N_{\text{part}}$  dependency of  $\pi^-/\pi^+$ ,  $K^-/K^+$  (upper panel) and  $K^+/\pi^+$ ,  $K^-/\pi^-$  (lower panel) for different collision energies ( $\sqrt{s_{NN}}$ ). Experimental data (blue and green) are from RHIC [6], RHIC-BES [66, 69], and LHC [68]. Model estimations are calculated from freeze-out parametrization. Ratio between the data and model are given below each plot.



■ Data  
○ Model

(a)



■ Data  
○ Model

(b)

FIGURE 6: (Color online)  $N_{\text{part}}$  dependency of  $\bar{p}/p$  (upper panel) and  $p/\pi^+$  (lower panel) for different  $\sqrt{s_{NN}}$ . Experimental data (red) are from Ref. [6, 66, 68, 69]. Thermal estimations (black) are estimated from freeze-out parametrization.

of the colliding nuclei and induces a smaller baryon antibaryon asymmetry in their yield.

At this point, we also want to mention that for the ratio  $\bar{p}/p$ , there is a chance of overfitting as our constructed ratio net-baryon to total baryon Eq. (8) reduces to  $\bar{p}/p$ , as we have utilized centrality dependent data for (anti-)proton from the baryon sector. This deficiency of our formalism will reduce when centrality data for other (anti-)baryons are considered (as discussed in Ref. [29]). On that occasion,  $\bar{p}/p$  will be an independent prediction.

We have discussed proton to positively charged pion ratio in Figure 6(b). As we have already discussed, pions may act as the measure of entropy. So the ratio  $p/\pi^+$  will describe the variation of baryon production with entropy. If the particles are produced only from deposited energy, then pions will be highly abundant than massive protons. But if the medium starts to evolve from a finite baryon density, then per pion, proton production will be larger to conserve the net baryon density. That is why a clear increasing trend for  $p/\pi^+$  takes place as the collision energy decreases. This same increment is expected with  $N_{\text{part}}$ , as more baryon deposition happens in the more central collisions. This variation is prominent in lower  $\sqrt{s_{NN}}$  due to the higher efficacy of baryon stopping.

## 5. Summary and Conclusion

The equilibration of the system created in a heavy-ion collision should strongly depend on the system size and number of participants. A comparison among the chemical freeze-out conditions of high and low multiplicity  $A$ - $A$  collisions may shed light in that direction. Instead of the general  $\chi^2$  minimization, a conserved charge-dependent parametrization process has been adopted, utilizing the midrapidity yield of the pion, kaon, and proton to explore the freeze-out parameters of various centrality bins of  $A$ - $A$  collision for LHC (2.76 TeV), RHIC (200 GeV, 130 GeV, 62.4 GeV), and RHIC-BES (39 GeV, 27 GeV, 19.6 GeV, 14.5 GeV, 11.5 GeV, and 7.7 GeV). We have incorporated a strangeness suppression factor ( $\gamma_S$ ) to estimate the possible nonequilibrium in strange hadrons in the peripheral collisions. We have discussed the variation of these chemical freeze-out parameters with both centrality and collision energy.

The variation of parameters with collision energies has good agreement with general understanding, whereas there are significant variations with the number of participants. The extracted freeze-out temperature has no strong dependence on the number of participants (centrality), whereas the chemical potentials show a wide variation. We have presented the behavior of scaled parameters to have a better understanding of the centrality variation. These parameters have been normalized with the value obtained in most central collisions and compared along with the other collision energies. Scaled  $\mu_Q$  and  $\mu_S$  appear to follow the scaling behavior of  $\mu_B$ , which may be a signal of equilibration among three conserved charges. The strangeness suppression factor ( $\gamma_S$ ) deviates from the equilibrium value at peripheral collisions and tends to saturate near unity in central collisions. In the

peripheral collisions,  $\gamma_S$  starts around .7 and increases towards most central bins. This variation indicates that the strange hadrons are deviated from equilibrium at low multiplicity collision, whereas there is a sign of equilibration as the  $N_{\text{part}}$  increases. The flattening of the scaled parameter and  $\gamma_S$  appears around a threshold of  $N_{\text{part}} = 150$ . So we can apply a grand canonical description for the systems created out of  $A$ - $A$  collisions with more participants than 150. We have found the  $\gamma_S$  to lie below 1 (around 0.9) even at most central collisions. In this study, we have only used kaons, so the variation of  $\gamma_S$  is an artifact of the kaon to pion ratio. Future analysis with yields data of other strange hyperons may help to understand this further.

Further, we have estimated different particle ratios to cross-check the effectiveness of our parameterization. Our estimated hadron ratios seem to have good agreement with experimental data. We have only reproduced ratios regarding pions, kaons, and protons as they are present in our analysis. A saturating trend with  $N_{\text{part}}$  has been observed for the kaon to pion ratio and explained with the  $\gamma_S$ .

We want to mention that the centrality variation has previously been investigated in RHIC-BES energy [66] and in LHC [56, 57, 73] with the  $\chi^2$  approach. Rather than the conventional practice, we have followed a fitting procedure that relies on the conserved quantities and produces similar parameter sets. The agreement with other studies will act as a benchmark for the future application of this parameterization. Further, we have found a threshold  $N_{\text{part}}$ , which is significant to study the bulk properties in a thermodynamic picture.

## Data Availability

All data used in the analysis are properly cited.

## Conflicts of Interest

The authors declare that they have no conflicts of interest.

## Acknowledgments

This work is funded by UGC and DST. The author thanks Sumana Bhattacharyya, Sanjay K. Ghosh, and Rajarshi Ray for the helpful discussions, and Pratik Goshal and Pracheta Singha for the critical reading of the manuscript. The publication and article processing charges are funded by SCOAP3.

## References

- [1] B. I. Abelev, M. M. Aggarwal, Z. Ahammed et al., "Identified particle production, azimuthal anisotropy, and interferometry measurements in Au+Au collisions at  $\sqrt{s_{NN}} = 9.2$  GeV," *Physical Review C*, vol. 81, no. 2, article 024911, 2010.
- [2] P. Foka and M. A. Janik, "An overview of experimental results from ultra-relativistic heavy-ion collisions at the CERN LHC: bulk properties and dynamical evolution," *Reviews in Physics*, vol. 1, p. 154, 2016.

- [3] P. Koch, B. Muller, and J. Rafelski, "Strangeness in relativistic heavy ion collisions," *Physics Reports*, vol. 142, no. 4, pp. 167–262, 1986.
- [4] J. Rafelski and B. Müller, "Strangeness Production in the Quark-Gluon Plasma," *Physical Review Letters*, vol. 48, pp. 1066–1069, 1982.
- [5] ALICE Collaboration, "Enhanced production of multi-strange hadrons in high-multiplicity proton-proton collisions," *Nature Physics*, vol. 13, no. 6, pp. 535–539, 2017.
- [6] STAR Collaboration, "Systematic measurements of identified particle spectra in  $pp$ ,  $d + Au$ , and  $Au+Au$  collisions at the STAR detector," *Physical Review C*, vol. 79, article 034909, 2009.
- [7] ALICE Collaboration, "Centrality dependence of the charged-particle multiplicity density at midrapidity in Pb-Pb collisions at  $\sqrt{s_{NN}} = 2.76$  TeV," *Physical Review Letters*, vol. 106, article 032301, 2011.
- [8] J. Cleymans and K. Redlich, "Unified description of freeze-out parameters in relativistic heavy ion collisions," *Physical Review Letters*, vol. 81, no. 24, pp. 5284–5286, 1998.
- [9] J. Cleymans, H. Oeschler, K. Redlich, and S. Wheaton, "Transition from baryonic to mesonic freeze-out," *Physics Letters B*, vol. 615, no. 1-2, pp. 50–54, 2005.
- [10] J. Cleymans, H. Oeschler, K. Redlich, and S. Wheaton, "Comparison of chemical freeze-out criteria in heavy-ion collisions," *Physics Review C*, vol. 73, no. 3, article 034905, 2006.
- [11] A. Andronic, P. Braun-Munzinger, and J. Stachel, "Hadron production in central nucleus-nucleus collisions at chemical freeze-out," *Nuclear Physics A*, vol. 772, no. 3-4, pp. 167–199, 2006.
- [12] A. Andronic, P. Braun-Munzinger, and J. Stachel, "Thermal hadron production in relativistic nuclear collisions: the hadron mass spectrum, the horn, and the QCD phase transition," *Physics Letters B*, vol. 673, no. 2, pp. 142–145, 2009.
- [13] J. Manninen and F. Becattini, "Chemical freeze-out in ultrarelativistic heavy ion collisions at  $s_{NN} = 130$  and 200 GeV," *Physics Review C*, vol. 78, article 054901, 2008.
- [14] A. Andronic, P. Braun-Munzinger, J. Stachel, and M. Winn, "Interacting hadron resonance gas meets lattice QCD," *Physics Letters B*, vol. 718, p. 80, 2012.
- [15] S. Chatterjee, R. M. Godbole, and S. Gupta, "Strange freeze-out," *Physics Letters B*, vol. 727, no. 4-5, pp. 554–557, 2013.
- [16] P. Alba, W. Alberico, R. Bellwied et al., "Freeze-out conditions from net-proton and net-charge fluctuations at RHIC," *Physics Letters B*, vol. 738, pp. 305–310, 2014.
- [17] S. Chatterjee, S. Das, L. Kumar et al., "Freeze-out parameters in heavy-ion collisions at AGS, SPS, RHIC, and LHC energies," *Advances in High Energy Physics*, vol. 2015, Article ID 349013, 20 pages, 2015.
- [18] R. P. Adak, S. Das, S. K. Ghosh, R. Ray, and S. Samanta, "Centrality dependence of chemical freeze-out parameters from net-proton and net-charge fluctuations using a hadron resonance gas model," *Physics Review C*, vol. 96, no. 1, article 014902, 2017.
- [19] S. Chatterjee, A. K. Dash, and B. Mohanty, "Contrasting freezeouts in large versus small systems," *Journal of Physics G: Nuclear and Particle Physics*, vol. 44, no. 10, article 105106, 2017.
- [20] S. Chatterjee, D. Mishra, B. Mohanty, and S. Samanta, "Freeze-out systematics due to the hadron spectrum," *Physics Review C*, vol. 96, no. 5, article 054907, 2017.
- [21] J. Rafelski, "Strange anti-baryons from quark-gluon plasma," *Physics Letters B*, vol. 262, no. 2-3, pp. 333–340, 1991.
- [22] J. Letessier, A. Tounsi, U. W. Heinz, J. Sollfrank, and J. Rafelski, "Strangeness conservation in hot nuclear fireballs," *Physics Review D*, vol. 51, no. 7, pp. 3408–3435, 1995.
- [23] J. Cleymans, A. Keränen, M. Marais, and E. Suhonen, "Exact baryon, strangeness, and charge conservation in hadronic gas models," *Physics Review C*, vol. 56, no. 5, pp. 2747–2751, 1997.
- [24] S. Hamieh, K. Redlich, and A. Tounsi, "Canonical description of strangeness enhancement from p-A to Pb-Pb collisions," *Physics Letters B*, vol. 486, no. 1-2, pp. 61–66, 2000.
- [25] J. Cleymans, B. Kampfer, and S. Wheaton, "Centrality dependence of thermal parameters in heavy-ion collisions at relativistic energies," *Physics Review C*, vol. 65, article 027901, 2002.
- [26] NA44 Collaboration, "Particle production in central Pb+Pb collisions at 158A GeV/c," *Physical Review C*, vol. 66, article 044907, 2002.
- [27] A. N. Tawfik, M. Y. El-Bakry, D. M. Habashy, M. T. Mohamed, and E. Abbas, "Degree of chemical nonequilibrium in central Au–Au collisions at RHIC energies," *International Journal of Modern Physics E*, vol. 24, article 1550067, 2015.
- [28] S. Bhattacharyya, D. Biswas, S. K. Ghosh, R. Ray, and P. Singha, "Systematics of chemical freeze-out parameters in heavy-ion collision experiments," *Physical Review D*, vol. 101, no. 5, article 054002, 2020.
- [29] S. Bhattacharyya, D. Biswas, S. K. Ghosh, R. Ray, and P. Singha, "Novel scheme for parametrizing the chemical freeze-out surface in heavy ion collision experiments," *Physical Review D*, vol. 100, no. 5, article 054037, 2019.
- [30] D. Biswas, "Formation of light nuclei at chemical freezeout: description within a statistical thermal model," *Physical Review C*, vol. 102, no. 5, article 054902, 2020.
- [31] R. Hagedorn and J. Rafelski, "Hot hadronic matter and nuclear collisions," *Physics Letters*, vol. 97, p. 136, 1980.
- [32] D. H. Rischke, M. I. Gorenstein, H. Stöcker, and W. Greiner, "Excluded volume effect for the nuclear matter equation of state," *Zeitschrift für Physik C Particles and Fields*, vol. C51, pp. 485–489, 1991.
- [33] J. Cleymans, M. I. Gorenstein, J. Stalnacke, and E. Suhonen, "Excluded volume effect and the quark-hadron phase transition," *Physica Scripta*, vol. 48, no. 3, pp. 277–280, 1993.
- [34] P. Braun-Munzinger, J. Stachel, J. P. Wessels, and N. Xu, "Thermal equilibration and expansion in nucleus-nucleus collisions at the AGS," *Physics Letters B*, vol. 344, no. 1-4, pp. 43–48, 1995.
- [35] J. Cleymans, D. Elliott, H. Satz, and R. L. Thews, "Thermal hadron production in Si-Au collisions," *Zeitschrift für Physik C Particles and Fields*, vol. 74, pp. 319–323, 1997.
- [36] G. D. Yen, M. I. Gorenstein, W. Greiner, and S.-N. Yang, "Excluded volume hadron gas model for particle number ratios in  $A + A$  collisions," *Physics Review C*, vol. 56, pp. 2210–2218, 1997.
- [37] P. Braun-Munzinger, I. Heppe, and J. Stachel, "Chemical equilibration in Pb+Pb collisions at the SPS," *Physics Letters B*, vol. 465, no. 1-4, pp. 15–20, 1999.
- [38] J. Cleymans and K. Redlich, "Chemical and thermal freeze-out parameters from 1A to 200 AGeV," *Physics Review C*, vol. 60, article 054908, 1999.

- [39] P. Braun-Munzinger, D. Magestro, K. Redlich, and J. Stachel, “Hadron production in Au-Au collisions at RHIC,” *Physics Letters B*, vol. 518, no. 1-2, pp. 41–46, 2001.
- [40] P. Braun-Munzinger, K. Redlich, and J. Stachel, “Particle production in heavy ion collision,” in *Quark-Gluon Plasma 3*, pp. 491–599, World Scientific, 2004.
- [41] F. Karsch, K. Redlich, and A. Tawfik, “Thermodynamics at non-zero baryon number density: a comparison of lattice and hadron resonance gas model calculations,” *Physics Letters B*, vol. 571, no. 1-2, pp. 67–74, 2003.
- [42] A. Tawfik, “QCD phase diagram: a comparison of lattice and hadron resonance gas model calculations,” *Physics Review D*, vol. 71, article 054502, 2005.
- [43] F. Becattini, J. Manninen, and M. Gazdzicki, “Energy and system size dependence of chemical freeze-out in relativistic nuclear collisions,” *Physics Review C*, vol. 73, article 044905, 2006.
- [44] V. V. Begun, M. Gazdzicki, and M. I. Gorenstein, “Hadron-resonance gas at freeze-out: Reminder on the importance of repulsive interactions,” *Physics Review C*, vol. 88, article 024902, 2013.
- [45] S. K. Tiwari, P. K. Srivastava, and C. P. Singh, “Description of hot and dense hadron-gas properties in a new excluded-volume model,” *Physics Review C*, vol. 85, article 014908, 2012.
- [46] J. Fu, “Higher moments of net-proton multiplicity distributions in heavy ion collisions at chemical freeze-out,” *Physics Letters B*, vol. 722, no. 1-3, pp. 144–150, 2013.
- [47] A. Tawfik, “Constant-trace anomaly as a universal condition for the chemical freeze-out,” *Physics Review C*, vol. 88, article 035203, 2013.
- [48] P. Garg, D. K. Mishra, P. K. Netrakanti et al., “Conserved number fluctuations in a hadron resonance gas model,” *Physics Letters B*, vol. 726, no. 4-5, pp. 691–696, 2013.
- [49] A. Bhattacharyya, S. Das, S. K. Ghosh, R. Ray, and S. Samanta, “Fluctuations and correlations of conserved charges in an excluded-volume hadron resonance gas model,” *Physics Review C*, vol. 90, article 034909, 2014.
- [50] G. P. Kadam and H. Mishra, “Dissipative properties of hot and dense hadronic matter in an excluded-volume hadron resonance gas model,” *Physics Review C*, vol. 92, no. 3, article 035203, 2015.
- [51] G. P. Kadam and H. Mishra, “Medium modification of hadron masses and the thermodynamics of the hadron resonance gas model,” *Physics Review C*, vol. 93, article 025205, 2016.
- [52] G. P. Kadam, “Curing the acausal behavior of the sound velocity in an excluded volume hadron resonance gas model,” 2015, <https://arxiv.org/abs/1510.04371>.
- [53] M. Albright, J. Kapusta, and C. Young, “Matching excluded-volume hadron-resonance gas models and perturbative QCD to lattice calculations,” *Physics Review C*, vol. 90, article 024915, 2014.
- [54] M. Albright, J. Kapusta, and C. Young, “Baryon number fluctuations from a crossover equation of state compared to heavy-ion collision measurements in the beam energy range  $s_{NN} = 7.7$  to 200 GeV,” *Physics Review C*, vol. 92, article 044904, 2015.
- [55] V. Begun, “Fluctuations as a test of chemical nonequilibrium at energies available at the CERN Large Hadron Collider,” *Physics Review C*, vol. 94, article 054904, 2016.
- [56] N. Sharma, J. Cleymans, B. Hippolyte, and M. Paradza, “Comparison of  $p-p$ ,  $p$ -Pb, and Pb-Pb collisions in the thermal model: multiplicity dependence of thermal parameters,” *Physical Review C*, vol. 99, no. 4, article 044914, 2019.
- [57] V. Vovchenko, B. Dönigus, and H. Stoecker, “Canonical statistical model analysis of  $p-p$ ,  $p$ -Pb, and Pb-Pb collisions at energies available at the CERN Large Hadron Collider,” *Physical Review C*, vol. 100, article 054906, 2019.
- [58] D. Biswas, K. Deka, A. Jaiswal, and S. Roy, “Viscosity, nonconformal equation of state, and sound velocity in Landau hydrodynamics,” *Physical Review C*, vol. 102, no. 1, article 014912, 2020.
- [59] M. L. Miller, K. Reygers, S. J. Sanders, and P. Steinberg, “Glauber modeling in high-energy nuclear collisions,” *Annual Review of Nuclear and Particle Science*, vol. 57, no. 1, pp. 205–243, 2007.
- [60] ALICE Collaboration, “Centrality determination of Pb-Pb collisions at  $\sqrt{s_{NN}} = 2.76$  TeV with ALICE,” *Physical Review C*, vol. 88, article 044909, 2013.
- [61] F. Becattini and J. Manninen, “Centrality dependence of strangeness production in heavy-ion collisions as a geometrical effect of core-corona superposition,” *Physics Letters B*, vol. 673, no. 1, pp. 19–23, 2009.
- [62] F. Becattini, M. Gazdzicki, and J. Sollfrank, “On chemical equilibrium in nuclear collisions,” *The European Physical Journal C*, vol. 5, p. 143, 1998.
- [63] J. Cleymans, B. Kampfer, and S. Wheaton, “Towards strangeness saturation in central heavy-ion collisions at high energies,” *Nuclear Physics A*, vol. 715, pp. 553c–556c, 2003.
- [64] F. Becattini, M. Gazdzicki, A. Keranen, J. Manninen, and R. Stock, “Chemical equilibrium study in nucleus-nucleus collisions at relativistic energies,” *Physics Review C*, vol. 69, article 024905, 2004.
- [65] J. Cleymans, B. Kampfer, P. Steinberg, and S. Wheaton, “System-size dependence of strangeness saturation,” *Journal of Physics G: Nuclear and Particle Physics*, vol. 30, no. 1, pp. S595–S598, 2004.
- [66] STAR Collaboration (STAR), “Bulk properties of the medium produced in relativistic heavy-ion collisions from the beam energy scan program,” *Physical Review C*, vol. 96, article 044904, 2017.
- [67] Y. Hatta and M. A. Stephanov, “Proton-number fluctuation as a signal of the QCD critical end point,” *Physical Review Letters*, vol. 91, no. 10, p. 102003, 2003.
- [68] ALICE collaboration, “Centrality dependence of  $\pi$ , K, and p production in  $Pb-Pb$  collisions at  $s_{NN} = 2.76$  TeV,” *Physical Review C*, vol. 88, article 044910, 2013.
- [69] J. Adam and D. Varela, “Inflationary twin models,” *Physical Review D*, vol. 101, article 024905, 2020.
- [70] Particle Data Group, “Review of particle physics,” *Physical Review D*, vol. 98, article 030001, 2018.
- [71] S. Wheaton, J. Cleymans, and M. Hauer, “THERMUS—A thermal model package for ROOT,” *Computer Physics Communications*, vol. 180, no. 1, pp. 84–106, 2009.
- [72] W. H. Press, S. A. Teukolsky, W. T. Vetterling, and B. P. Flannery, *Numerical Recipes: The Art of Scientific Computing*, Cambridge University Press, New York, NY, USA, 3rd edition, 2007.
- [73] F. Becattini, E. Grossi, M. Bleicher, J. Steinheimer, and R. Stock, “Centrality dependence of hadronization and chemical freeze-out conditions in heavy ion collisions at  $s_{NN} = 2.76$  TeV,” *Physics Review C*, vol. 90, article 054907, 2014.

- [74] R. Hagedorn, "Statistical thermodynamics of strong interactions at high energies," *Nuovo Cimento Supplemento*, vol. 3, p. 147, 1965.
- [75] H. Sorge, "Flavor production in Pb(160A GeV) on Pb collisions: Effect of color ropes and hadronic rescattering," *Physical Review C*, vol. 52, no. 6, pp. 3291–3314, 1995.
- [76] E-802 Collaboration, "Particle production at high baryon density in central Au+Au reactions at 11.6A GeV/c," *Physical Review C*, vol. 57, article R466, 1998.
- [77] J. J. Gaardhoje, I. Arsene, I. G. Bearden et al., "The new physics at RHIC. From transparency to high pt suppression," *Nuclear Physics A*, vol. 734, pp. 13–27, 2004.
- [78] J. I. Kapusta and M. Li, "High baryon densities achievable at RHIC and LHC," *Nuclear Physics A*, vol. 982, pp. 903–906, 2019.
- [79] A. Kurkela and A. Mazeliauskas, "Chemical equilibration in hadronic collisions," *Physical Review Letters*, vol. 122, no. 14, p. 142301, 2019.
- [80] G. Knoll, *Radiation Detection and Measurement*, Wiley, 2000.
- [81] Q. Y. Shou, Y. G. Ma, P. Sorensen, A. H. Tang, F. Videbæk, and H. Wang, "Parameterization of deformed nuclei for Glauber modeling in relativistic heavy ion collisions," *Physics Letters B*, vol. 749, pp. 215–220, 2015.

## Research Article

# Transverse Momentum and Pseudorapidity Spectrum of the Top Quark, Lepton, and $b$ Jet in Proton-Proton Collisions at LHC

Li-Na Gao  and Er-Qin Wang 

Department of Physics, Taiyuan Normal University, Jinzhong, Shanxi 030619, China

Correspondence should be addressed to Li-Na Gao; [gao-lina@qq.com](mailto:gao-lina@qq.com)

Received 8 December 2020; Revised 12 January 2021; Accepted 2 April 2021; Published 23 April 2021

Academic Editor: Bhartendu K. Singh

Copyright © 2021 Li-Na Gao and Er-Qin Wang. This is an open access article distributed under the Creative Commons Attribution License, which permits unrestricted use, distribution, and reproduction in any medium, provided the original work is properly cited. The publication of this article was funded by SCOAP<sup>3</sup>.

We study the transverse momentum and pseudorapidity spectrum of the top quark and their decay products, the  $t\bar{t}$  system, and the total number of jets in proton-proton (pp) collisions at 13 TeV by using the Tsallis-Pareto-type function and the three-source Landau hydrodynamic model, respectively. The related parameters, such as the effective temperature of the interacting system ( $T$ ), the nonextensivity of the process ( $n$ ), and the width ( $\sigma$ ) of pseudorapidity distribution, are extracted.

## 1. Introduction

The top quark is an interesting particle. It was first found by the Tevatron detector of Fermi National Accelerator Laboratory in 1995 [1–3]. As the heaviest particle in the Standard Model, the top quark is very different from the other quark. Its biggest mass is one of the hotspots for physicists. And it is the only one quark which will decay before it becomes hadron. These unique properties make top quark occupy a very important position in particle physics.

The Large Hadron Collider (LHC) has created a lot of top quark events since 2010. Physicists could study the top quark in detail with the help of the LHC. By studying the final state particles produced in high-energy collisions, physicists could obtain some information about the evolution of the collision system. The spectra of transverse momenta ( $p_T$ ) and (pseudo)rapidity ( $\eta/y$ ) are important quantities measured in experiments. Many models and functions are used to describe the transverse momentum and pseudorapidity spectra.

In this paper, we use the Tsallis-Pareto-type function [4, 5] and the three-source Landau hydrodynamic model [6] to describe the transverse momentum and pseudorapidity spectra of the top quark, lepton, and bottom quark produced in

proton-proton (pp) collisions at the center of mass energy  $\sqrt{s} = 13$  TeV measured at the parton level and particle level, in the full phase space and in the fiducial phase by CMS Collaboration at the LHC [7]. The values of related parameters are extracted and analyzed.

The present paper is organized as follows. We briefly introduce the Tsallis-Pareto-type function and the three-source Landau hydrodynamic model in Section 2. The result of comparisons with experimental data is given in Section 3. Moreover, we outlined the conclusions in Section 4.

## 2. The Model and Formalism

**2.1. The Tsallis-Pareto-Type Function.** There are some models and functions that could be used to analyze the transverse momentum distribution, such as the Erlang distribution [8–10], the inverse power law [11–14], the Schwinger mechanism [9, 10, 15, 16], Lévy distribution [16], and the Tsallis statistics [17–22]. In a lot of models and formulas, the Tsallis-Pareto-type function is a good choice for transverse momentum spectra. Whether in the relative high  $p_T$  region or the relative low  $p_T$  region, people could use the Tsallis-Pareto-type function to fit the experimental data well

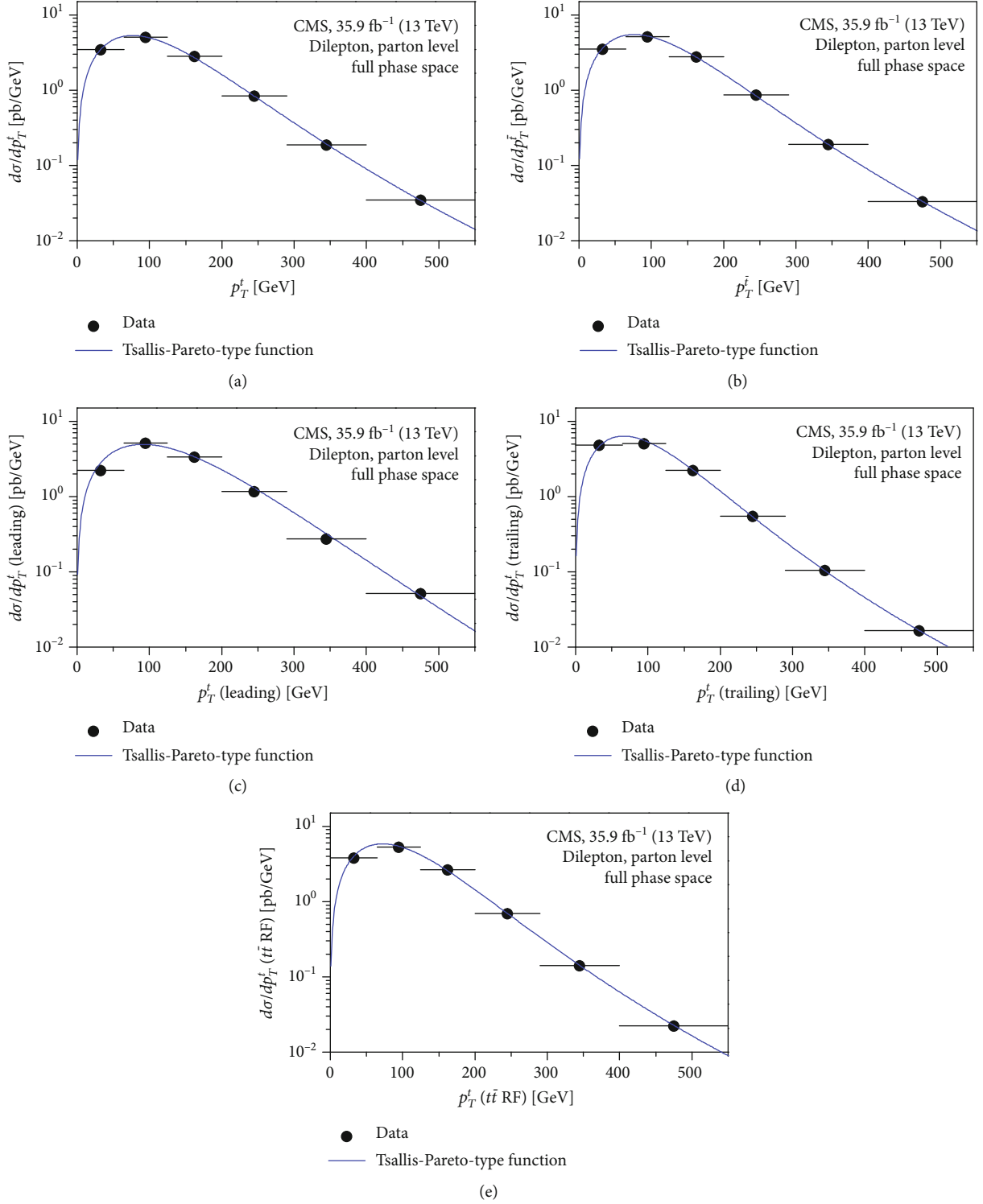


FIGURE 1: Transverse momentum distribution of (a) the top quark ( $p_T^t$ ), (b) the top antiquark ( $p_T^{\bar{t}}$ ), (c) the top quark or top antiquark with the largest  $p_T$  ( $p_T^t$ (leading)), (d) the top quark or top antiquark with the second-largest  $p_T$  ( $p_T^t$ (trailing)), and (e) the top quark in the rest frame of the  $t\bar{t}$  system ( $p_T^t$  ( $t\bar{t}$ RF)) at the parton level in the full phase space produced in pp collisions at  $\sqrt{s} = 13$  TeV. The solid circles represent the experimental data of the CMS Collaboration in literature [7]; the curves are our results calculated by the Tsallis-Pareto-type function.

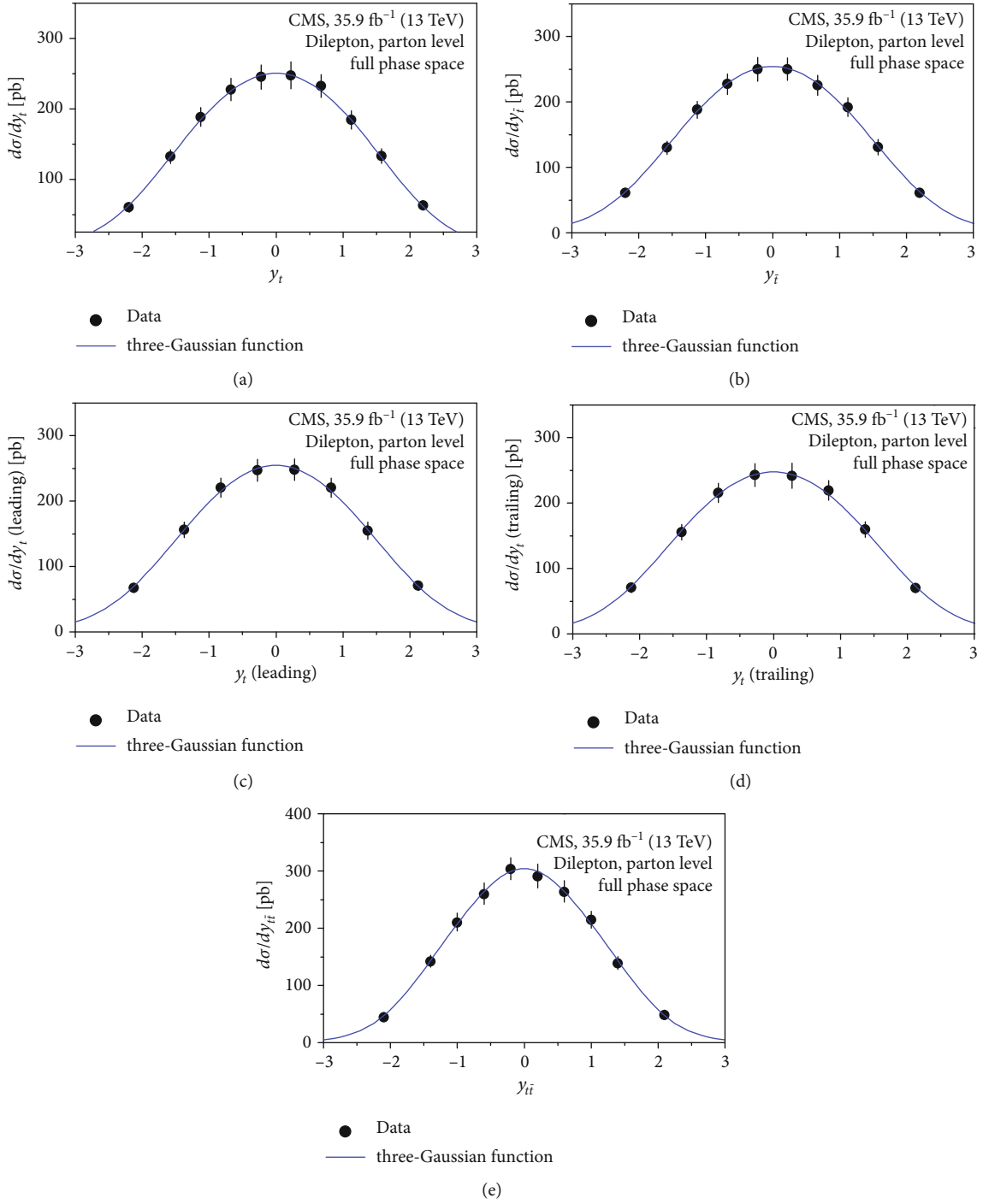


FIGURE 2: Rapidity distributions of (a) the top quark ( $y_t$ ), (b) the top antiquark ( $y_{\bar{t}}$ ), (c) the top quark or top antiquark with the largest  $p_T$  ( $y_t$  (leading)), (d) the top quark or top antiquark with the second-largest  $p_T$  ( $y_t$  (trailing)), and (e) the  $t\bar{t}$  system ( $y_{t\bar{t}}$ ) at the parton level in the full phase space produced in pp collisions at  $\sqrt{s} = 13$  TeV. The solid circles represent the experimental data of the CMS Collaboration in literature [7]; the curves are our results calculated by the three-Gaussian functions.

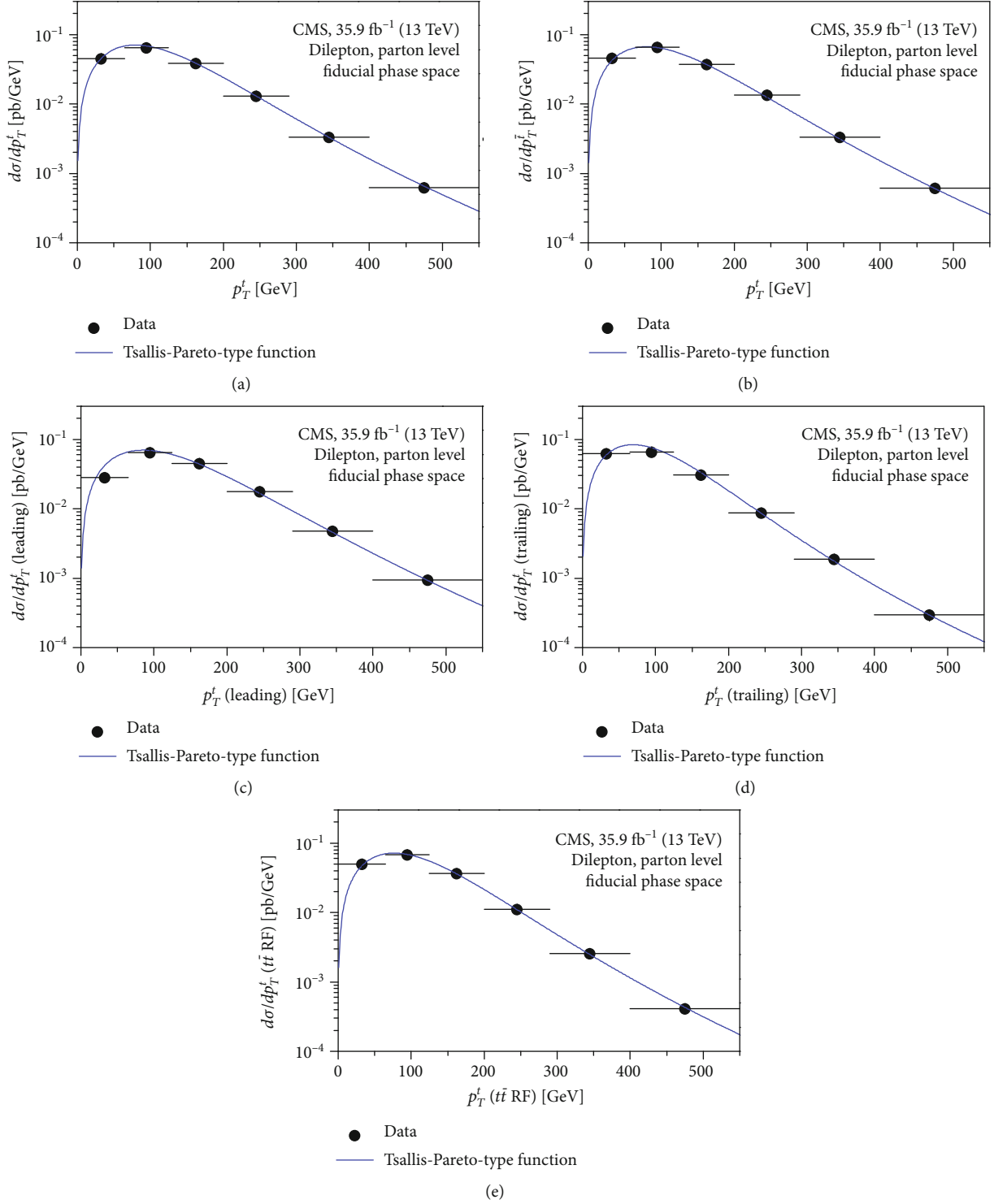


FIGURE 3: The same as Figure 1 but showing the results of transverse-momentum distribution of (a)  $p_T^t$ , (b)  $p_T^{\bar{t}}$ , (c)  $p_T^t$  (leading), (d)  $p_T^t$  (trailing), and (e)  $p_T^t$  ( $t\bar{t}$ RF) at the particle level in the fiducial phase space.

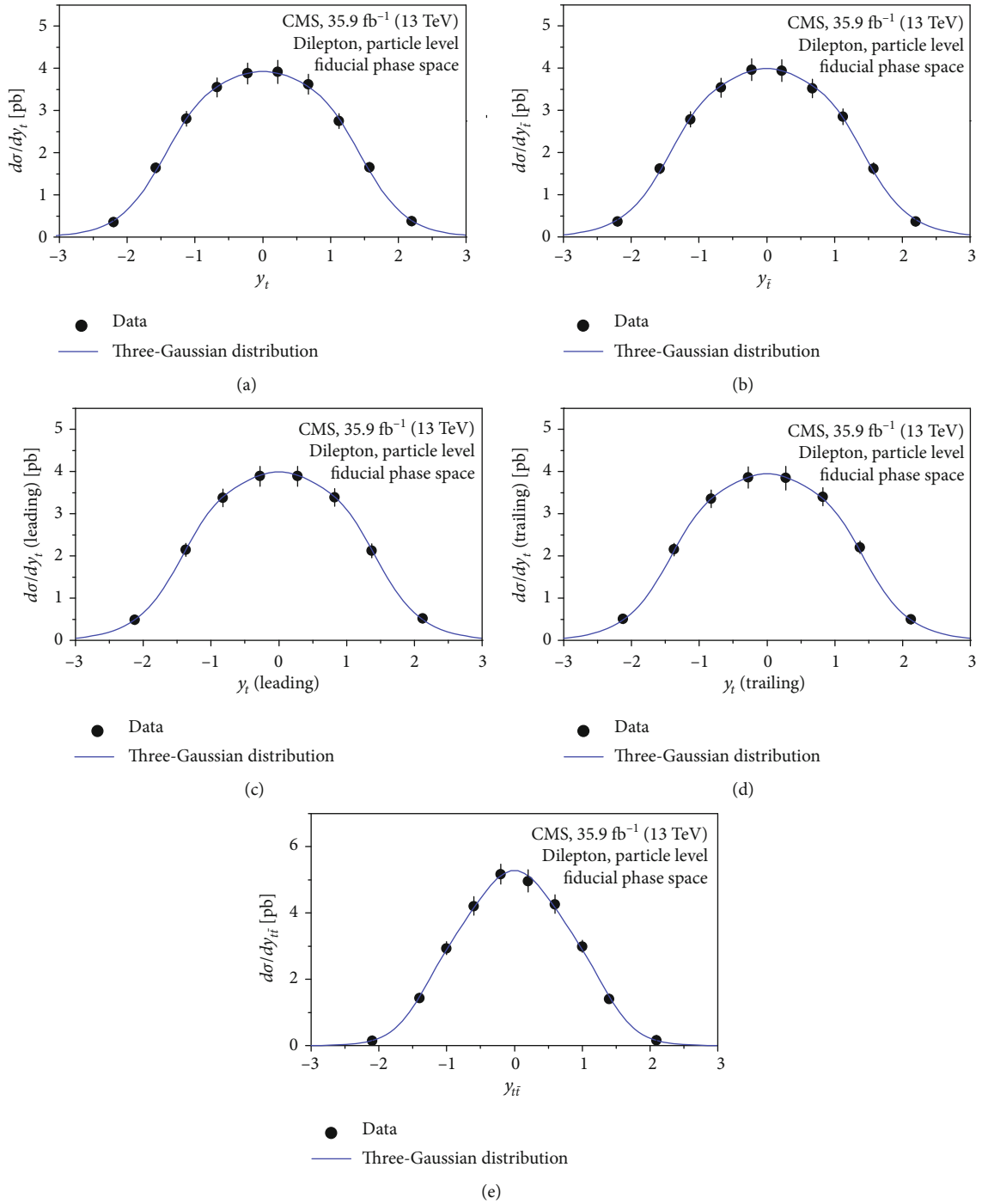


FIGURE 4: The same as Figure 2 but showing the results of (a)  $y_t$ , (b)  $y_{\bar{t}}$ , (c)  $y_t$  (leading), (d)  $y_t$  (trailing), and (e)  $y_{t\bar{t}}$  at the particle level in the fiducial phase space.

TABLE 1: Values of parameters and  $\chi^2/\text{dof}$  corresponding to the curves in Figures 1, 3, 5, 7, 11, 12, 13, 15, and 16.

Figure	Type	$n$	$T$ (GeV)	$\chi^2/\text{dof}$
13 TeV				
1(a)	$t$	$9.23 \pm 0.65$	$29.26 \pm 2.98$	0.021
1(b)	$\bar{t}$	$9.32 \pm 0.68$	$29.02 \pm 2.58$	0.012
1(c)	$t$ (leading)	$22.00 \pm 0.93$	$41.56 \pm 3.54$	0.411
1(d)	$t$ (trailing)	$8.05 \pm 0.53$	$22.25 \pm 2.13$	0.037
1(e)	$t$ ( $t\bar{t}$ RF)	$9.22 \pm 0.62$	$26.25 \pm 2.25$	0.022
3(a)	$t$	$8.80 \pm 0.57$	$31.00 \pm 2.85$	0.018
3(b)	$\bar{t}$	$9.20 \pm 0.65$	$31.50 \pm 3.00$	0.083
3(c)	$t$ (leading)	$10.20 \pm 0.70$	$36.00 \pm 2.95$	0.732
3(d)	$t$ (trailing)	$8.20 \pm 0.52$	$24.00 \pm 2.20$	0.150
3(e)	$t$ ( $t\bar{t}$ RF)	$9.50 \pm 0.67$	$29.20 \pm 2.50$	0.030
5(a)	$l$	$4.72 \pm 1.00$	$8.50 \pm 1.30$	0.056
5(b)	$\bar{l}$	$4.80 \pm 1.10$	$8.55 \pm 1.30$	0.036
5(c)	$l$ (leading)	$5.80 \pm 1.25$	$13.00 \pm 2.60$	3.517
5(d)	$l$ (trailing)	$4.15 \pm 0.85$	$3.90 \pm 0.70$	0.324
5(e)	$\bar{l}$	$7.88 \pm 1.55$	$14.50 \pm 3.00$	0.611
7(a)	$b$ (leading)	$15.00 \pm 2.00$	$28.00 \pm 3.00$	6.550
7(b)	$b$ (trailing)	$10.00 \pm 1.30$	$15.20 \pm 2.30$	1.101
7(c)	$b\bar{b}$	$23.00 \pm 2.80$	$30.00 \pm 3.00$	13.903
7 TeV				
11(a)	$t$	$9.52 \pm 0.68$	$25.00 \pm 2.50$	0.024
11(c)	$\bar{t}$	$1.40 \pm 0.15$	$0.27 \pm 0.07$	0.078
12(a)	$b$	$21.40 \pm 1.80$	$28.80 \pm 2.80$	0.406
12(c)	$l$	$3.95 \pm 0.40$	$7.30 \pm 0.90$	0.104
8 TeV				
13(a)	$t$	$8.96 \pm 0.86$	$26.82 \pm 2.52$	0.064
13(b)	$t\bar{t}$	$2.32 \pm 0.30$	$3.10 \pm 0.40$	1.206
13(c)	$t$ (leading)	$13.54 \pm 1.16$	$33.68 \pm 2.80$	1.144
13(d)	$t$ (trailing)	$7.12 \pm 0.82$	$20.23 \pm 2.10$	0.061
13(e)	$t$ ( $t\bar{t}$ RF)	$9.35 \pm 0.90$	$24.45 \pm 2.50$	0.116
15(a)	$l$	$4.97 \pm 0.57$	$8.50 \pm 0.50$	59.839
15(b)	$\bar{l}$	$6.80 \pm 0.80$	$12.60 \pm 1.10$	1.144
16(a)	$b$	$16.95 \pm 1.25$	$25.58 \pm 2.53$	0.988
16(b)	$b\bar{b}$	$16.32 \pm 1.08$	$29.06 \pm 2.86$	19.317

[5]. So, in this work, we chose the Tsallis-Pareto-type function to describe the transverse momentum spectra. The Tsallis-Pareto-type function can be written as [5]

$$\frac{d^2N}{dydp_T} = \frac{dN}{dy} C P_T \left[ 1 + \frac{m_T - m_0}{nT} \right]^{-n}, \quad (1)$$

where  $m_0$  is the rest mass of each particle;  $C$  and  $m_T$  are given by

$$C = \frac{(n-1)(n-2)}{nT[nT + (n-2)m_0]}, \quad (2)$$

$$m_T = \sqrt{m_0^2 + p_T^2}.$$

$T$  and  $n$  are free parameters.  $T$  means the mean effective temperature of the interacting system, and it is connected with the average particle energy.  $n$  reveals the nonextensivity of the process, and it denotes the departure of the spectra from the Boltzmann distribution [5]. We could obtain values of the two free parameters ( $T$  and  $n$ ) by using the Tsallis-Pareto-type function to fit the  $p_T$  spectra.

**2.2. The Three-Source Landau Hydrodynamic Model.** The three-source Landau hydrodynamic model has become a mature theoretical model in research for the pseudorapidity distributions at nuclear collisions. In our previous work, this model has described the experimental data successfully [6]. In the present work, we will use it to fit the pseudorapidity distributions of particles (top quark, lepton, and bottom quark) produced in pp collisions at  $\sqrt{s} = 13$  TeV again. The following is a brief description of the three-source Landau hydrodynamic model.

The source means particle emission source. We think the rapidity distribution of particles produced in high-energy collisions is contributed by the three emission sources. The three emission sources are a central source ( $C$ ), a target source ( $T$ ), and a projectile ( $P$ ). The central source is located at the central of rapidity distribution and covers the whole rapidity range. The target source and projectile source are located at the left and right side of the central source, respectively. And the target source and projectile source are revisions for the central source. For the rapidity distribution of particles produced in each emission source, we can use a Gaussian form of the Landau solution to describe it [23–25]:

$$\frac{dN_{ch}}{dy} = \frac{N_0}{\sqrt{2\pi}\sigma_X} \exp\left(-\frac{(y-y_X)^2}{2\sigma_X^2}\right), \quad (3)$$

where  $N_0$  is the normalization constant,  $y$  is rapidity,  $\sigma$  denote the width of rapidity distribution, and  $X$  represents the type of emission source.

Actually, the three-source Landau hydrodynamic model can be written as a form of a superposition of three-Gaussian forms of the Landau solution:

$$\frac{dN_{ch}}{dy} = \frac{N_0}{\sqrt{2\pi}} \left\{ \frac{k_T}{\sigma_T} \exp\left(-\frac{(y-y_T)^2}{2\sigma_T^2}\right) + \frac{k_C}{\sigma_C} \exp\left(-\frac{(y-y_C)^2}{2\sigma_C^2}\right) + \frac{k_P}{\sigma_P} \exp\left(-\frac{(y-y_P)^2}{2\sigma_P^2}\right) \right\}. \quad (4)$$

TABLE 2: Values of parameters and  $\chi^2/\text{dof}$  corresponding to the curves in Figures 2, 4, 6, 8, 11, 12, 14, 15, and 16.

Figure	Type	$k_C$	$y_P/\eta_P$	$\sigma(C)$	$\sigma(P)$	$\chi^2/\text{dof}$
13 TeV						
2(a)	$t$	$0.887 \pm 0.017$	$1.354 \pm 0.074$	$1.230 \pm 0.025$	$0.718 \pm 0.015$	0.013
2(b)	$\bar{t}$	$0.892 \pm 0.020$	$1.354 \pm 0.074$	$1.230 \pm 0.025$	$0.718 \pm 0.018$	0.026
2(c)	$t$ (leading)	$0.908 \pm 0.022$	$1.354 \pm 0.074$	$1.245 \pm 0.030$	$0.725 \pm 0.018$	0.019
2(d)	$t$ (trailing)	$0.892 \pm 0.018$	$1.354 \pm 0.074$	$1.265 \pm 0.033$	$0.720 \pm 0.015$	0.012
2(e)	$t\bar{t}$	$0.935 \pm 0.025$	$1.354 \pm 0.074$	$1.040 \pm 0.025$	$0.518 \pm 0.008$	0.020
4(a)	$t$	$0.840 \pm 0.020$	$1.100 \pm 0.060$	$1.000 \pm 0.020$	$0.470 \pm 0.006$	0.037
4(b)	$\bar{t}$	$0.875 \pm 0.022$	$1.100 \pm 0.060$	$1.020 \pm 0.020$	$0.425 \pm 0.008$	0.102
4(c)	$t$ (leading)	$0.875 \pm 0.022$	$1.100 \pm 0.060$	$1.020 \pm 0.022$	$0.425 \pm 0.007$	0.053
4(d)	$t$ (trailing)	$0.875 \pm 0.025$	$1.100 \pm 0.060$	$1.020 \pm 0.020$	$0.425 \pm 0.008$	0.032
4(e)	$t\bar{t}$	$0.905 \pm 0.027$	$1.100 \pm 0.060$	$0.780 \pm 0.018$	$0.355 \pm 0.005$	0.232
6(a)	$l$	$0.915 \pm 0.103$	$1.225 \pm 0.300$	$1.235 \pm 0.040$	$0.650 \pm 0.035$	0.027
6(b)	$\bar{l}$	$0.912 \pm 0.100$	$1.225 \pm 0.300$	$1.235 \pm 0.040$	$0.672 \pm 0.040$	0.014
6(c)	$l$ (leading)	$0.950 \pm 0.110$	$0.990 \pm 0.285$	$1.235 \pm 0.030$	$0.560 \pm 0.030$	0.033
6(d)	$l$ (trailing)	$0.918 \pm 0.105$	$1.265 \pm 0.310$	$1.268 \pm 0.035$	$0.670 \pm 0.040$	0.040
8(a)	$b$ (leading)	$0.930 \pm 0.110$	$1.225 \pm 0.280$	$1.210 \pm 0.050$	$0.650 \pm 0.045$	0.012
8(b)	$b$ (trailing)	$0.915 \pm 0.105$	$1.550 \pm 0.300$	$1.270 \pm 0.050$	$0.680 \pm 0.060$	0.012
7 TeV						
11(b)	$t$	$0.880 \pm 0.110$	$1.290 \pm 0.328$	$0.970 \pm 0.015$	$0.430 \pm 0.010$	0.088
11(d)	$t\bar{t}$	$0.950 \pm 0.130$	$1.290 \pm 0.315$	$0.840 \pm 0.010$	$0.450 \pm 0.013$	0.056
12(b)	$b$	$0.920 \pm 0.125$	$1.290 \pm 0.325$	$1.190 \pm 0.030$	$0.700 \pm 0.020$	0.040
12(c)	$l$	$0.904 \pm 0.110$	$1.290 \pm 0.320$	$1.120 \pm 0.030$	$0.700 \pm 0.022$	0.009
8 TeV						
14(a)	$t$	$0.900 \pm 0.080$	$1.290 \pm 0.290$	$1.110 \pm 0.020$	$0.680 \pm 0.015$	0.028
14(b)	$t\bar{t}$	$0.900 \pm 0.100$	$1.290 \pm 0.300$	$0.875 \pm 0.015$	$0.540 \pm 0.010$	0.070
15(c)	$l$	$0.905 \pm 0.100$	$1.280 \pm 0.260$	$1.140 \pm 0.025$	$0.570 \pm 0.018$	0.232
16(c)	$b$	$0.923 \pm 0.112$	$1.280 \pm 0.255$	$1.240 \pm 0.030$	$0.550 \pm 0.015$	0.027

A given parameter  $k$  is the contribution of each emission source,  $k_T + k_C + k_P = 1$ . For the symmetric collision, we think  $k_T = k_P$ . Because of  $y \approx \eta$  at very high energy, we could describe the pseudorapidity distributions of lepton by the following formula:

$$\frac{dN_{ch}}{d\eta} = \frac{N_0}{\sqrt{2\pi}} \left\{ \frac{k_T}{\sigma_T} \exp\left(-\frac{(\eta - \eta_T)^2}{2\sigma_T^2}\right) + \frac{k_C}{\sigma_C} \exp\left(-\frac{(\eta - \eta_C)^2}{2\sigma_C^2}\right) + \frac{k_P}{\sigma_P} \exp\left(-\frac{(\eta - \eta_P)^2}{2\sigma_P^2}\right) \right\}. \quad (5)$$

Significantly, as a revision of the central source, the contributions of the target source and projectile source are small.

### 3. Comparisons with Experimental Data

From the experimental point of view, the particle-level definition is expected to result in decreased uncertainties with respect to a definition at the parton level [26]. So, in this work, we use the same approach to analyze the experimental data.

In this section, we study the transverse momentum and pseudorapidity spectrum of the top quark, lepton, and  $b$  jet in proton-proton collisions at LHC. Based on the Tsallis-Pareto-type function, we describe the transverse momentum spectra of the related product. And we use the three-source Landau hydrodynamic model to analyze the pseudorapidity and rapidity distribution.

Figures 1 and 2 show the transverse momentum and rapidity cross sections of (a) the top quark ( $t$ ), (b) the top antiquark ( $\bar{t}$ ), (c) the top quark or top antiquark with

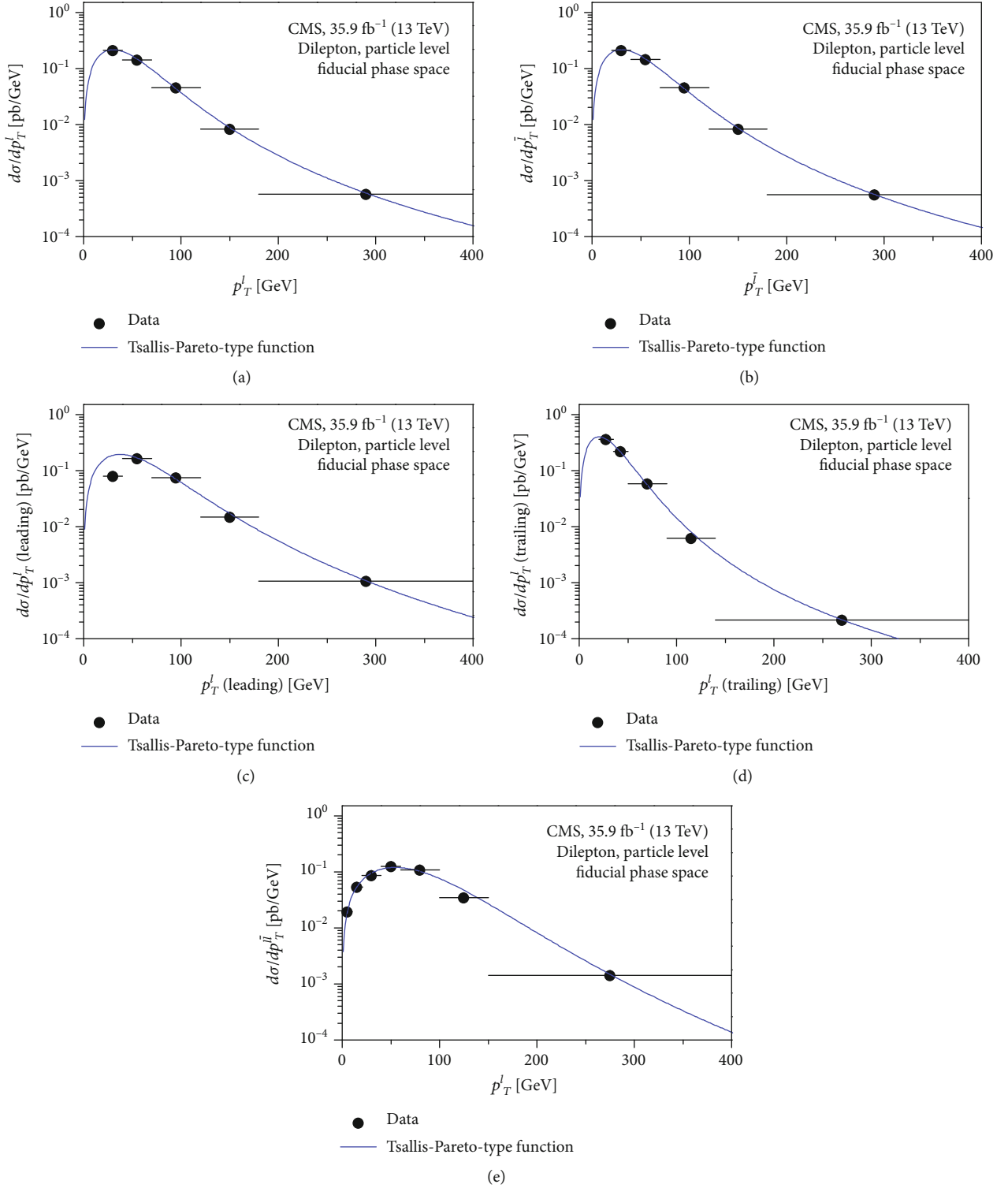


FIGURE 5: The same as Figure 1 but showing the results of transverse momentum distribution of (a) the lepton ( $p_T^l$ ), (b) the antilepton ( $p_T^{\bar{l}}$ ), (c) the lepton or antilepton with the largest  $p_T$  ( $p_T^l$  (leading)), (d) the lepton or antilepton with the second-largest  $p_T$  ( $p_T^l$  (trailing)), and (e) the dilepton system ( $p_T^{\bar{l}}$ ) at the particle level in the fiducial phase space.

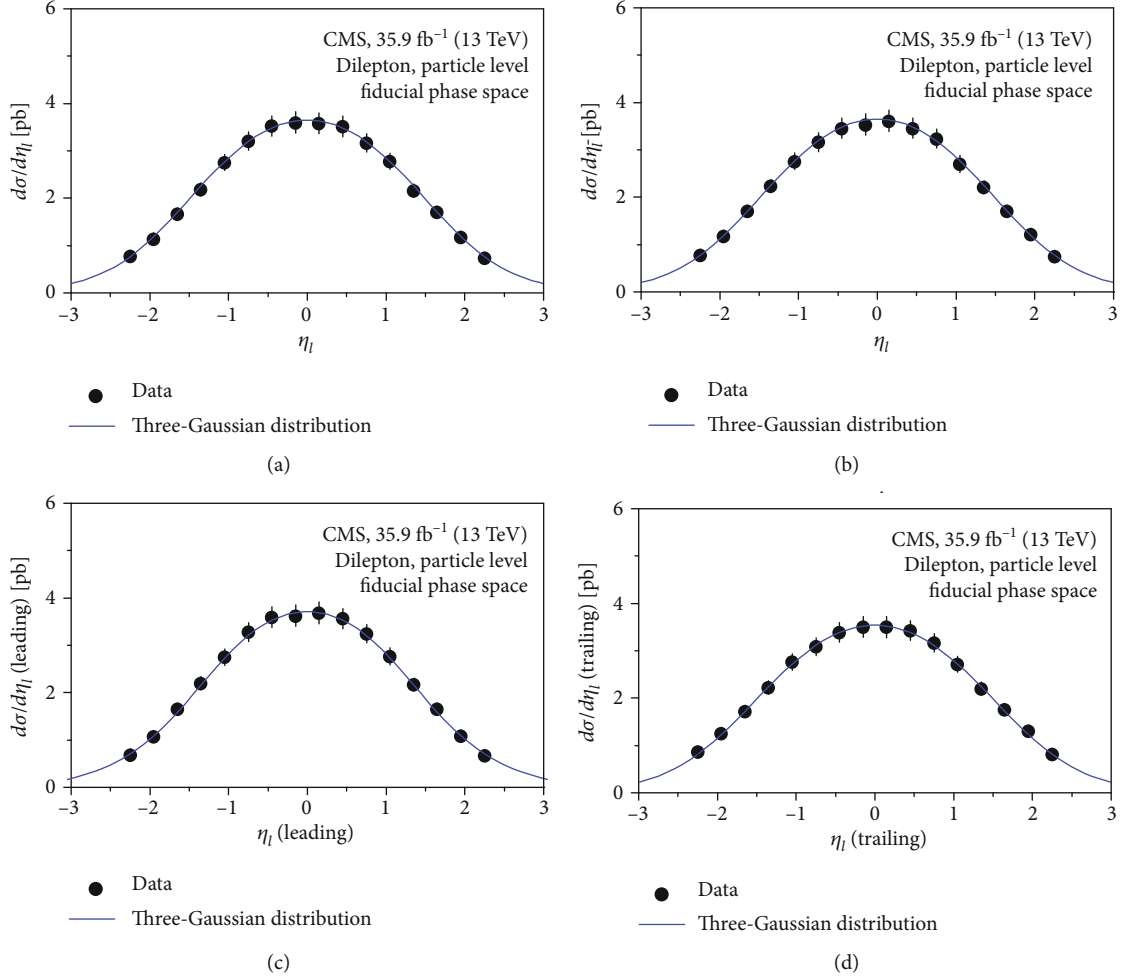


FIGURE 6: The same as Figure 2 but showing the results of pseudorapidity distribution of (a) the lepton ( $\eta_l$ ), (b) the antilepton ( $\eta_{\bar{l}}$ ), (c) the lepton or antilepton with the largest  $p_T$  ( $\eta_l$  (leading)), and (d) the lepton or antilepton with the second-largest  $p_T$  ( $\eta_l$  (trailing)).

the largest  $p_T$  ( $t$  (leading)), (d) the top quark or top antiquark with the second-largest  $p_T$  ( $t$  (trailing)), and (e) the top quark in the rest frame of the  $t\bar{t}$  system ( $t\bar{t}$  RF) at the parton level in the full phase space produced in pp collisions at  $\sqrt{s} = 13$  TeV. The same as Figures 1 and 2, but Figures 3 and 4 show the results at the particle level in the fiducial phase space. In these four figures, the solid circles represent the experimental data recorded by the CMS experiment at the LHC and correspond to an integrated luminosity of  $35.9 \text{ fb}^{-1}$  in 2016 [7]. In Figures 1 and 3, the curves are our results calculated by the Tsallis-Pareto-type function. In Figures 2 and 4, the curves show the calculate results of the three-Gaussian functions. Obviously, our results fit well with the experimental data. One can see that the Tsallis-Pareto-type function and the three-Gaussian functions are very helpful approaches to describe the transverse momentum and rapidity cross sections of particles, respectively. The related parameter values ( $n$ ,  $T$ ,  $k$ ,  $y_p$ ,  $\sigma$ ) extracted from the transverse momentum and rapidity cross sections and  $\chi^2/\text{dof}$  are given in Tables 1 and 2. We could find

that the values of  $n$  and  $T$  of  $t$  (leading) are the biggest in the five-type particles at the parton and particle level in the full and fiducial phase space. The values of  $y_p$  are the same in the scope of consideration. The values of  $k$ ,  $\sigma(C)$ , and  $\sigma(P)$  are basically the same within the margin of error in the  $t$ ,  $\bar{t}$ ,  $t$  (leading), and  $t$  (trailing), but these three parameter values decreased significantly in the rest frame of the  $t\bar{t}$  system.

Figures 5 and 6 show the transverse momentum and rapidity cross sections of (a) the lepton ( $l$ ), (b) the antilepton ( $\bar{l}$ ), (c) the lepton or antilepton with the largest  $p_T$  ( $l$  (leading)), and (d) the lepton or antilepton with the second-largest  $p_T$  ( $l$  (trailing)), and Figure 5(e) shows the transverse momentum cross sections of the dilepton system ( $l\bar{l}$ ) at the particle level in the fiducial phase space produced in pp collisions at  $\sqrt{s} = 13$  TeV. The solid circles and curves represent the experimental data and our calculated results, respectively. One can see that the results calculated by using the theoretical functions are in agreement with the experimental data. The related parameters are extracted and listed in Tables 1 (5(a)–(e)) and 2 (6(a)–(d)). The values of  $n$  and  $T$  of the  $l\bar{l}$

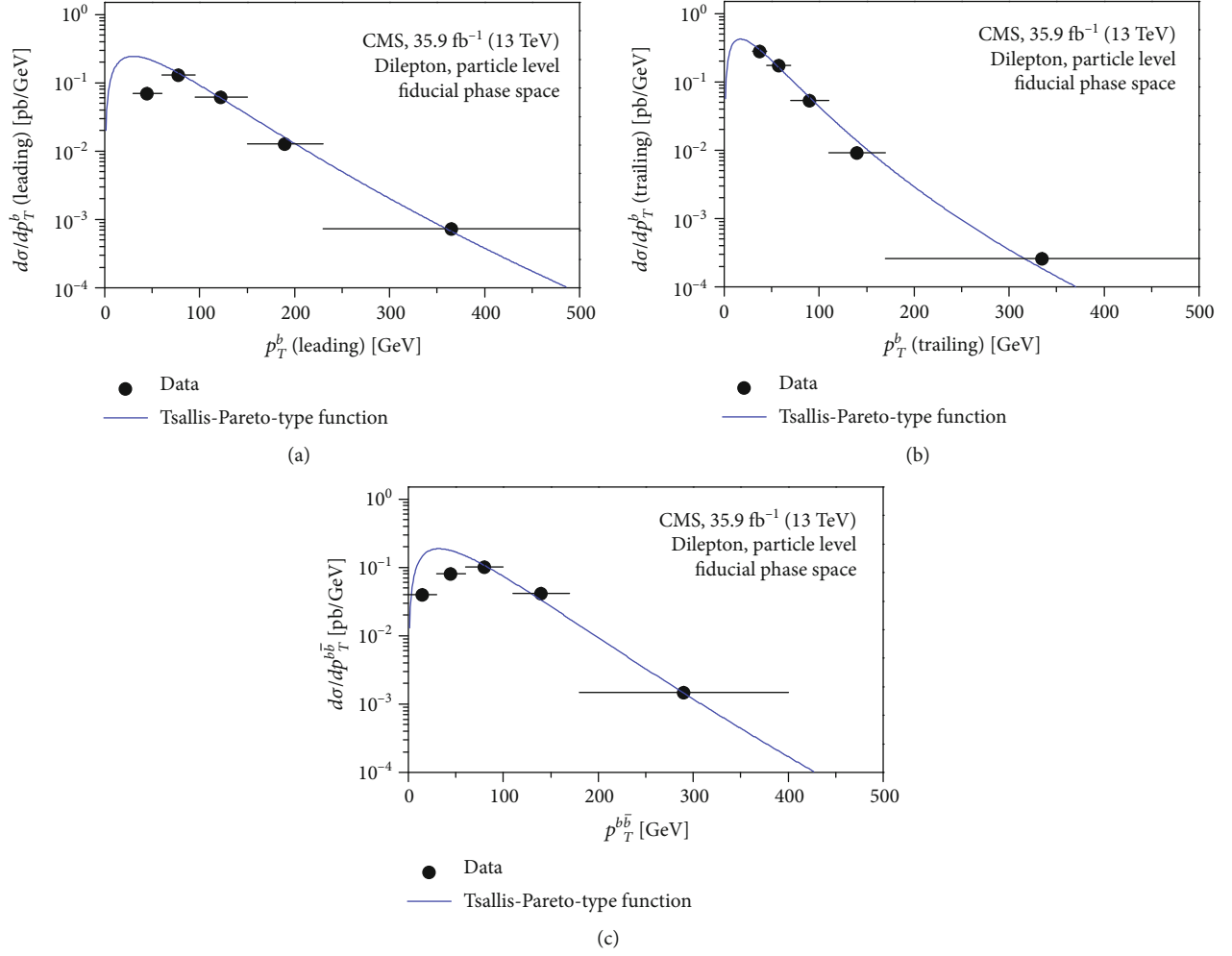


FIGURE 7: The same as Figure 1 but showing the results of transverse momentum distribution of (a) the  $b$  jet with the largest  $p_T$  ( $p_T^b$  (leading)), (b) the  $b$  jet with the second-largest  $p_T$  ( $p_T^b$  (trailing)), and (c) the  $b\bar{b}$  system ( $p_T^{b\bar{b}}$ ) at the particle level in the fiducial phase space.

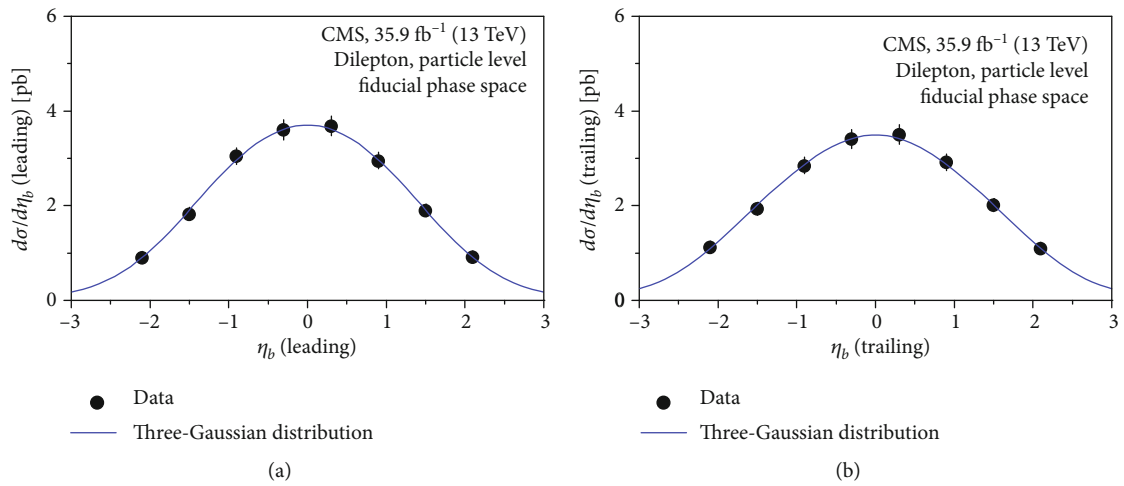


FIGURE 8: The same as Figure 2 but showing the results of pseudorapidity distribution of (a) the  $b$  jet with the largest  $p_T$  ( $\eta_b$  (leading)) and (b) the  $b$  jet with the second-largest  $p_T$  ( $\eta_b$  (trailing)).

TABLE 3: The values of  $\langle p_T \rangle$  and  $\sqrt{\langle p_T^2 \rangle / 2}$  are calculated by the curves in Figures 1, 3, 5, and 7.

Figure	Type	$\langle p_T \rangle$ (GeV/c)	$\sqrt{\langle p_T^2 \rangle / 2}$ (GeV/c)
At parton level in the full phase space			
9(a)/10(a)	$t$	$120.691 \pm 0.014$	$102.471 \pm 6.971$
	$\bar{t}$	$119.785 \pm 0.012$	$101.604 \pm 6.247$
	$t$ (leading)	$137.210 \pm 0.015$	$114.073 \pm 7.430$
	$t$ (trailing)	$103.660 \pm 0.006$	$88.028 \pm 3.131$
	$t\bar{t}$	$112.256 \pm 0.008$	$94.944 \pm 4.114$
At particle level in the fiducial phase space			
9(b)/10(b)	$t$	$126.834 \pm 0.017$	$108.302 \pm 8.416$
	$\bar{t}$	$127.002 \pm 0.018$	$108.153 \pm 8.762$
	$t$ (leading)	$136.458 \pm 0.022$	$115.996 \pm 10.800$
	$t$ (trailing)	$108.473 \pm 0.008$	$92.235 \pm 3.834$
	$t\bar{t}$	$119.830 \pm 0.012$	$101.536 \pm 5.958$
	$l$	$53.617 \pm 0.004$	$49.657 \pm 1.768$
9(c)/10(c)	$\bar{l}$	$53.322 \pm 0.003$	$49.075 \pm 1.703$
	$l$ (leading)	$64.970 \pm 0.005$	$58.171 \pm 2.743$
	$l$ (trailing)	$34.914 \pm 0.001$	$32.255 \pm 0.450$
	$\bar{l}\bar{l}$	$81.272 \pm 0.003$	$68.092 \pm 1.428$
	$b$ (leading)	$69.613 \pm 0.004$	$62.890 \pm 1.861$
9(d)/10(d)	$b$ (trailing)	$42.804 \pm 0.001$	$39.883 \pm 0.348$
	$b\bar{b}$	$69.127 \pm 0.002$	$61.179 \pm 0.867$

system are bigger than the other particles. The values of  $k$ ,  $y_p$ ,  $\sigma(C)$ , and  $\sigma(P)$  of the considered particles are not different obviously.

The results of transverse momentum and rapidity cross sections of (a) the  $b$  jet with the largest  $p_T$  ( $b$  (leading)) and (b) the  $b$  jet with the second-largest  $p_T$  ( $b$  (trailing)) are showed in Figures 7 and 8, and Figure 7(c) shows the transverse momentum cross sections of the  $b\bar{b}$  system at the particle level in the fiducial phase space produced in pp collisions at  $\sqrt{s} = 13$  TeV. We have extracted the related parameters by describing the transverse momentum and rapidity cross section distributions and listed them in Tables 1 (7(a)–(c)) and 2 (8(a)–(b)). The values of parameters are not in an obvious relationship.

Generally, the initial temperature ( $T_i$ ) and mean transverse momentum ( $\langle p_T \rangle$ ) are important physical quantities to understand the excitation degree of the interacting system. The two physical quantities are not dependent on the selected models and functions; they are only dependent on the experimental data. According to the literatures [27–29],  $T_i$  can be described by the ratio of root-mean-square  $p_T$  to  $\sqrt{2}$  ( $\sqrt{\langle p_T^2 \rangle / 2}$ ) approximately. So, we calculated the values of  $\langle p_T \rangle$  and  $\sqrt{\langle p_T^2 \rangle / 2}$  by the curves in Figures 1, 3, 5, and 7 and listed them in Table 3. Figures 9 and 10 show the  $\langle p_T \rangle$  and  $\sqrt{\langle p_T^2 \rangle / 2}$  of each particle. From Figures 9 and 10, we could observe that the  $\langle p_T \rangle$  and  $\sqrt{\langle p_T^2 \rangle / 2}$  of each particle are big. This

phenomenon means that the excitation degree of the interacting system is violent.

In order to find the relationship between the free parameter and collision energy, we have extracted the related parameters from the transverse momentum and rapidity cross sections at 7 TeV and 8 TeV (Figures 11–16), together. In Figures 11 and 12, the solid circles represent the experimental data recorded by the CMS experiment at 7 TeV and correspond to an integrated luminosity of  $5.0 \text{ fb}^{-1}$  in 2011 [30]. In Figures 13–16, the solid circles represent the experimental data recorded by the CMS experiment at 8 TeV and correspond to an integrated luminosity of  $19.7 \text{ fb}^{-1}$  in 2012 [31]. From the transverse momentum and rapidity cross sections of final state particles, we extracted the values of free parameters and listed them in Tables 1 and 2. And we plot the  $T$ ,  $n$ , and  $\sigma$  values listed in Tables 1 and 2 in Figure 17. In the panel, the symbols represent the values of  $T$ ,  $n$ , and  $\sigma$ , and the lines are linear fitting functions. The intercepts, slopes, and  $\chi^2/\text{dof}$  corresponding to the lines are listed in Table 4. From Figure 17 and Table 4, we found that the values of  $T$  show a slight increase with the collision energy increased; this phenomenon may be affected by QGP. It can be explained by the influence of jet quenching effect (quickly energy loss) in the case of high-energy quark and gluon jets penetrating through the dense deconfined matter [32].  $\sigma(C)$  shows to be increased with the collision

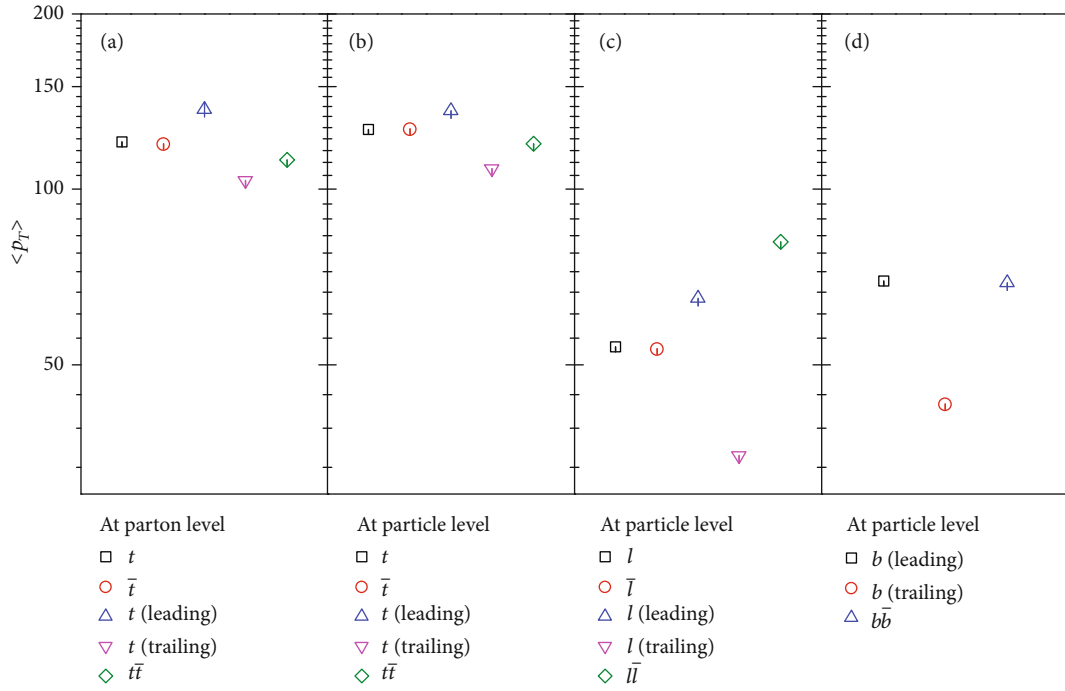


FIGURE 9: The values of  $\langle p_T \rangle$  for different particles.

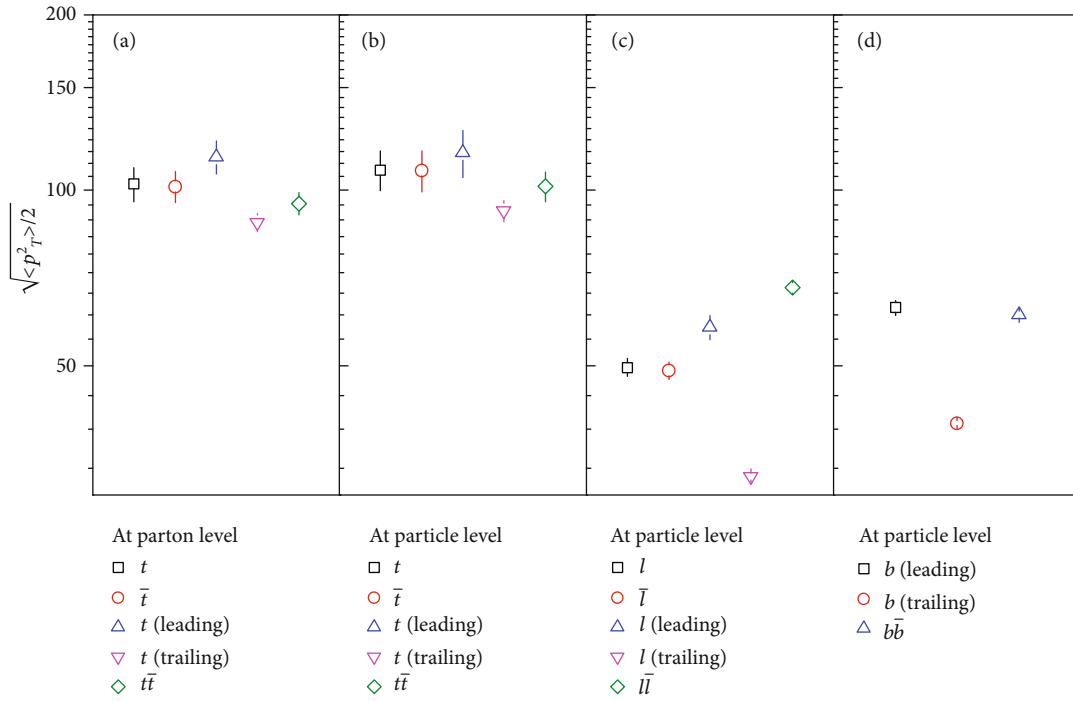
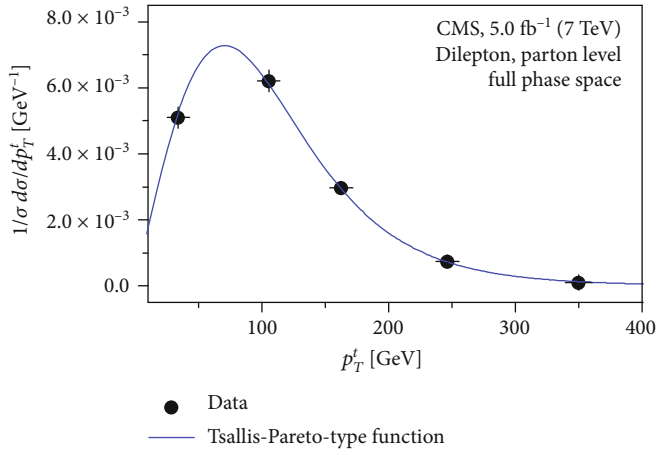
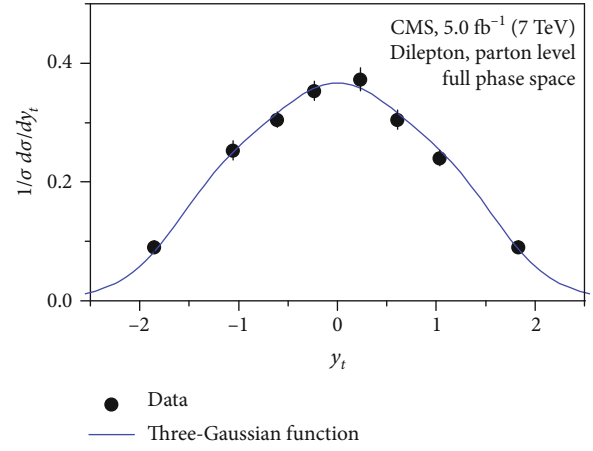


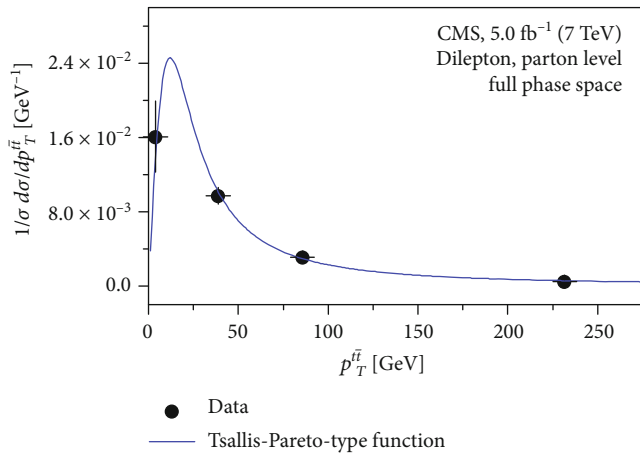
FIGURE 10: The same as Figure 9 but showing the values of  $\sqrt{\langle p_T^2 \rangle}/2$ .



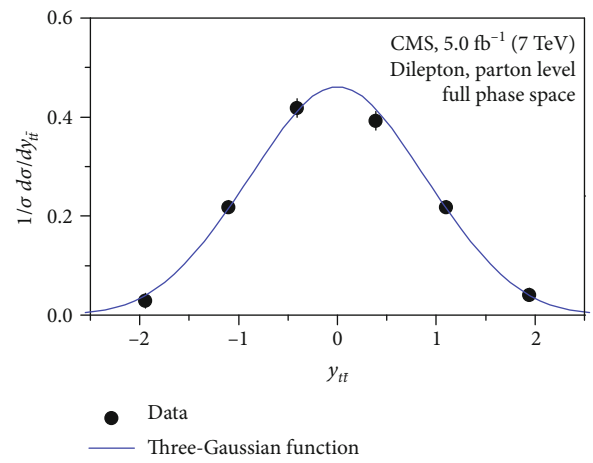
(a)



(b)

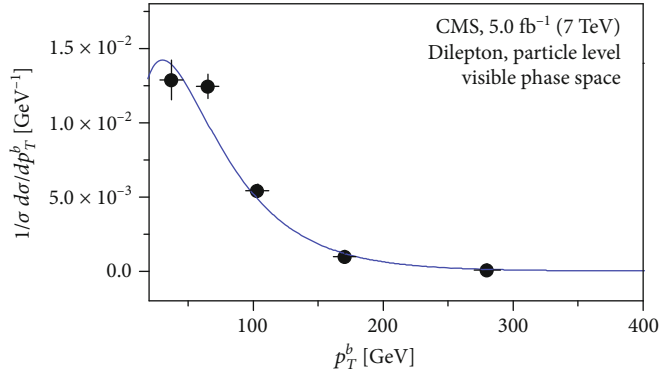


(c)



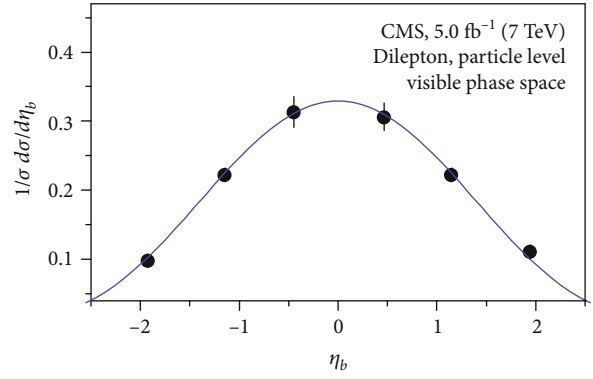
(d)

FIGURE 11: The same as Figures 1 and 2, but showing the results of  $t$  and  $t\bar{t}$  produced in pp collisions at the parton level in the full phase space at  $\sqrt{s} = 7$  TeV.



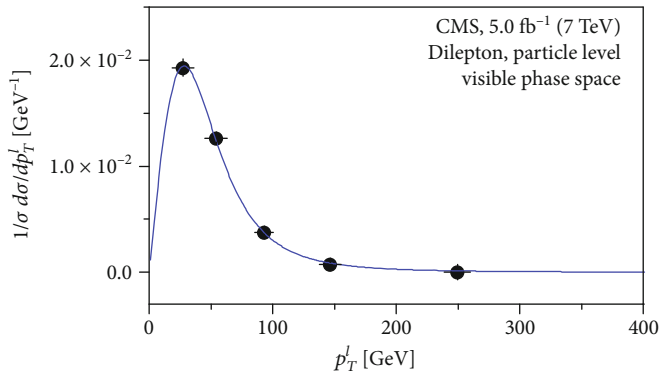
● Data  
— Tsallis-Pareto-type function

(a)



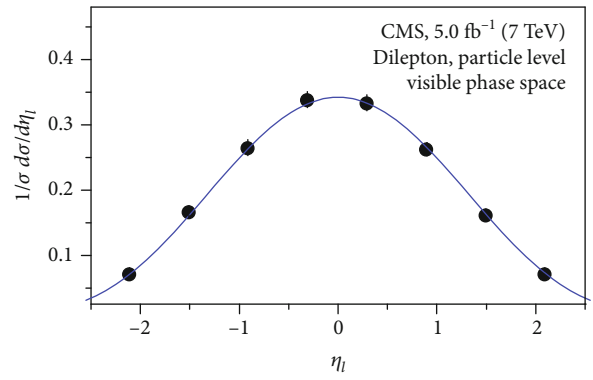
● Data  
— Three-Gaussian function

(b)



● Data  
— Tsallis-Pareto-type function

(c)



● Data  
— Three-Gaussian function

(d)

FIGURE 12: The same as Figures 1 and 5, but showing the results of  $b$  and  $l$  produced in pp collisions at the particle level in the visible phase space at  $\sqrt{s} = 7$  TeV.

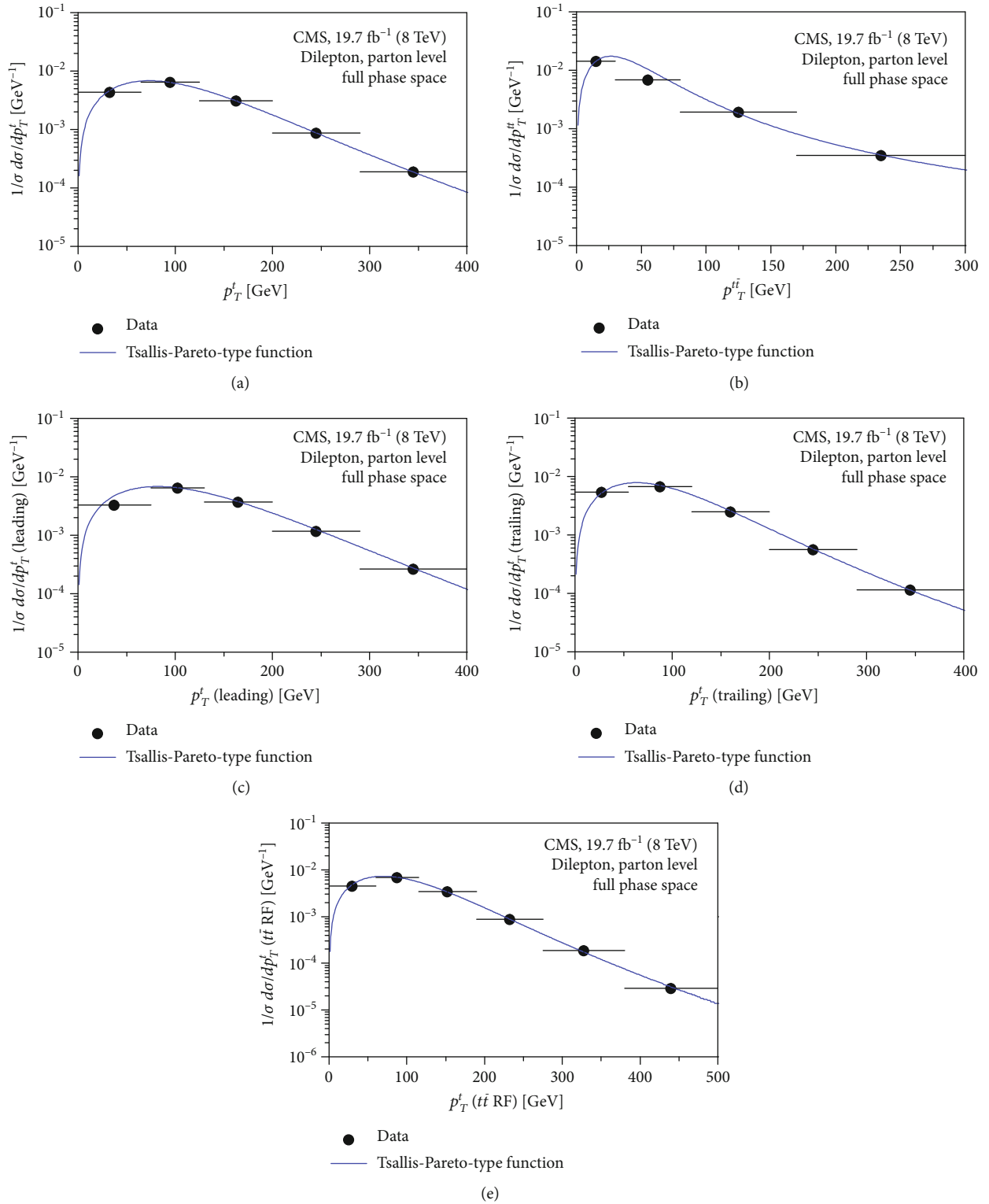


FIGURE 13: The same as Figure 1 but showing the results of transverse momentum distribution of (a)  $p_T^t$ , (b)  $p_T^{\bar{t}}$ , (c)  $p_T^t$  (leading), (d)  $p_T^t$  (trailing), and (e)  $p_T^t$  ( $t\bar{t}$ RF) at the parton level in the full phase space at  $\sqrt{s} = 8$  TeV.

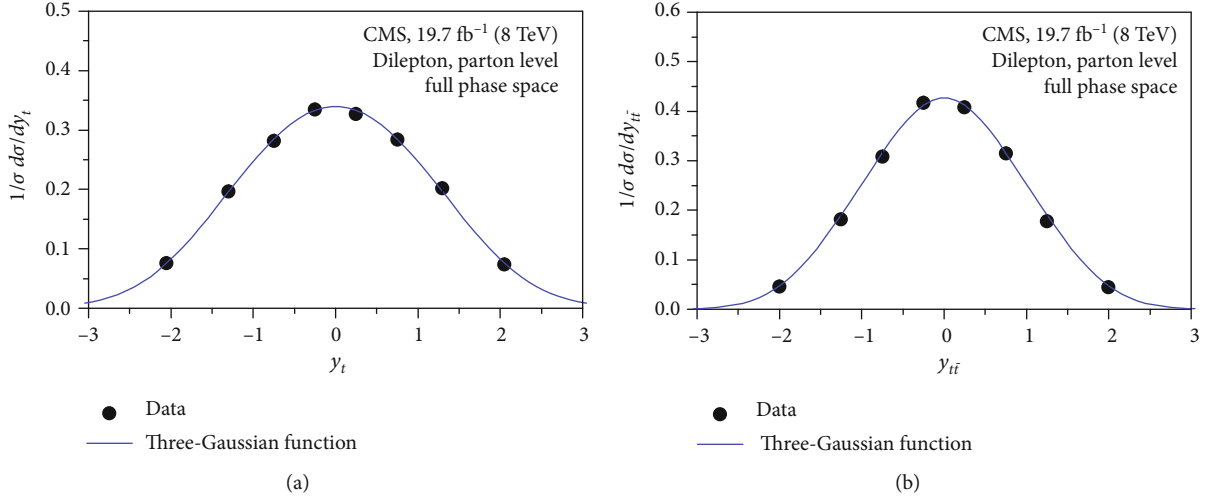


FIGURE 14: The same as Figure 2 but showing the results of rapidity distribution of  $t$  and  $\bar{t}$  at the parton level in the full phase space at  $\sqrt{s} = 8$  TeV.

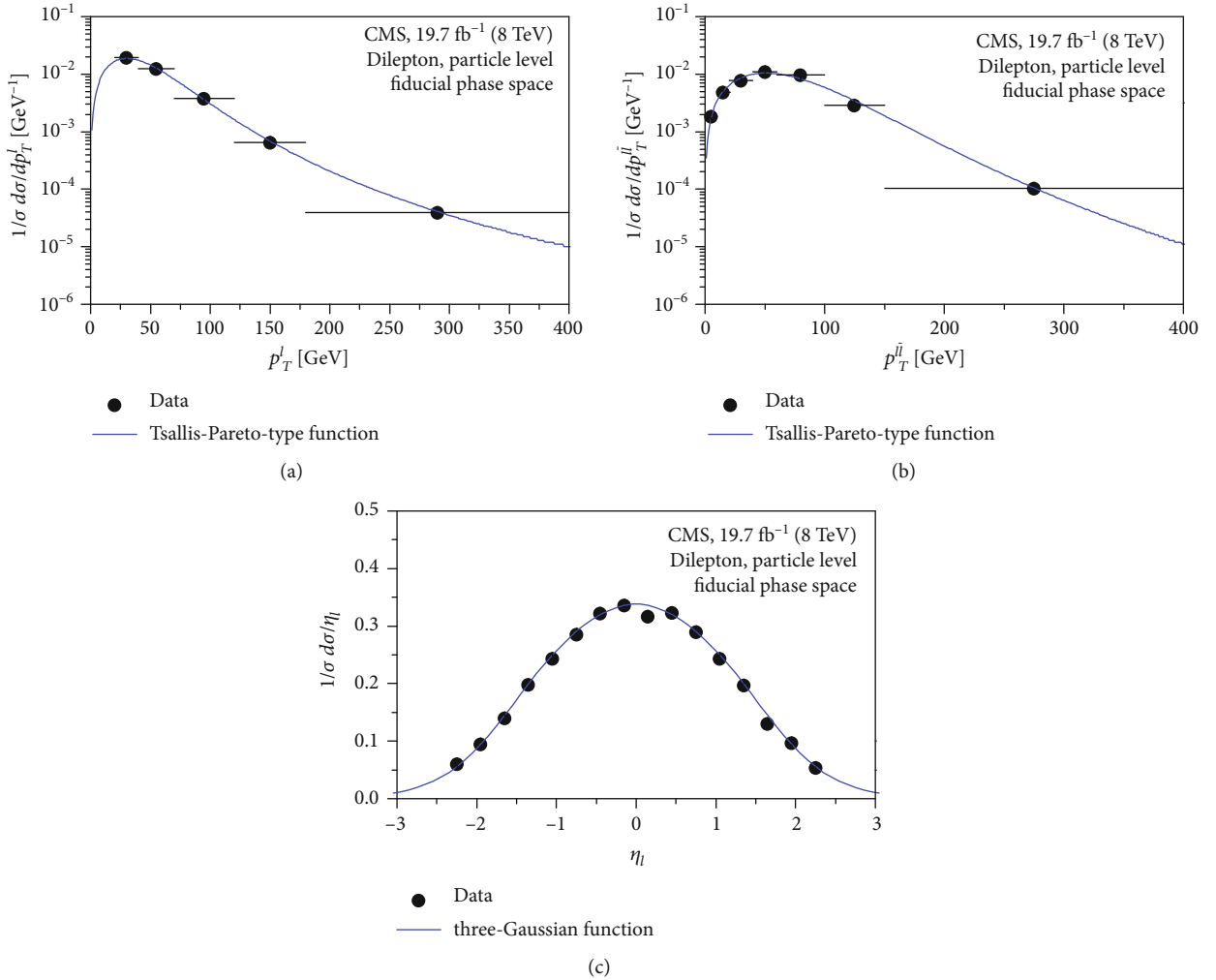


FIGURE 15: The same as Figures 1 and 5, but showing the results of  $l$  and  $\bar{l}$  produced in pp collisions at the particle level in the fiducial phase space at  $\sqrt{s} = 8$  TeV.

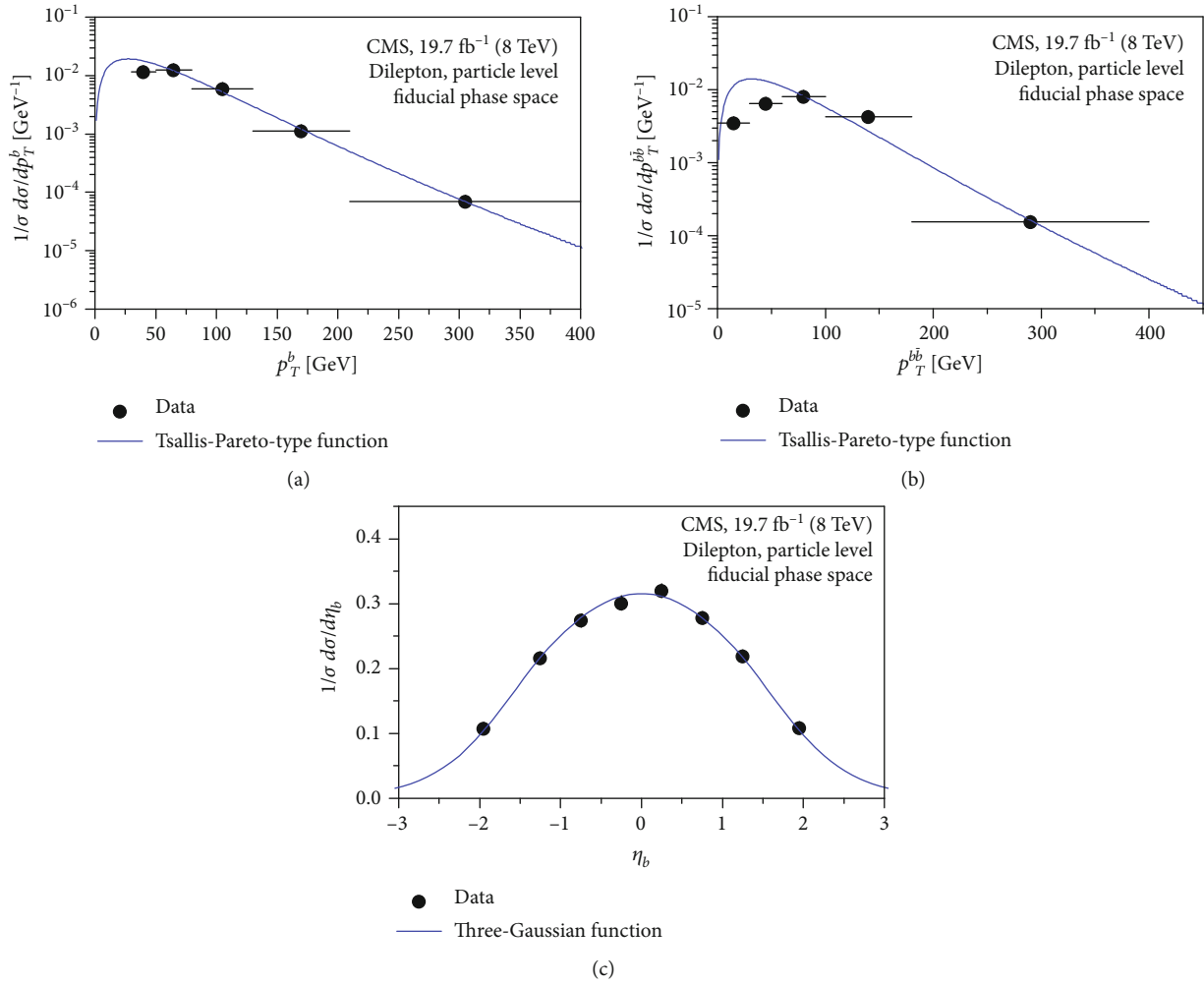


FIGURE 16: The same as Figures 1 and 5, but showing the results of  $b$  and  $b\bar{b}$  produced in pp collisions at the particle level in the fiducial phase space at  $\sqrt{s} = 8$  TeV.

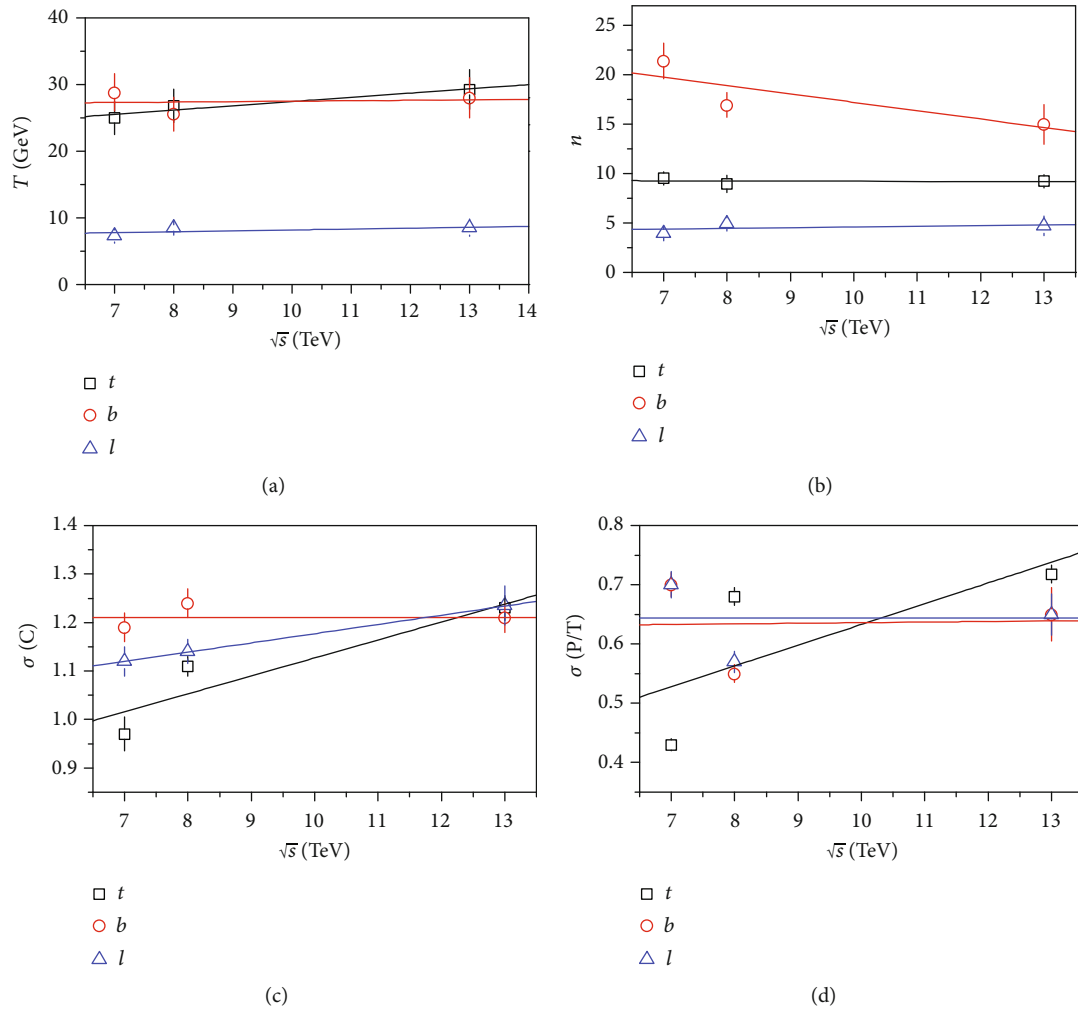


FIGURE 17: The relationship of the free parameter and collision energy.

TABLE 4: Values of intercepts, slopes, and  $\chi^2/\text{dof}$  corresponding to the lines in Figure 17.

Particle	Intercept	Slope	$\chi^2/\text{dof}$
$T - \sqrt{s}$			
$t$	$21.068 \pm 1.276$	$0.638 \pm 0.132$	0.113
$b$	$26.846 \pm 3.547$	$0.066 \pm 0.366$	0.796
$l$	$6.835 \pm 1.149$	$0.135 \pm 0.118$	1.643
$n - \sqrt{s}$			
$t$	$9.380 \pm 0.588$	$-0.015 \pm 0.061$	0.258
$b$	$25.702 \pm 3.888$	$-0.848 \pm 0.401$	3.324
$l$	$3.886 \pm 1.025$	$0.071 \pm 0.106$	1.996
$\sigma(C) - \sqrt{s}$			
$t$	$0.757 \pm 0.111$	$0.037 \pm 0.011$	9.802
$b$	$1.210 \pm 0.054$	$0.000 \pm 0.006$	1.405
$l$	$0.987 \pm 0.001$	$0.019 \pm 0.000$	0.001
$\sigma(P/T) - \sqrt{s}$			
$t$	$0.283 \pm 0.232$	$0.035 \pm 0.024$	158.376
$b$	$0.626 \pm 0.163$	$0.001 \pm 0.017$	41.913
$l$	$0.644 \pm 0.140$	$0.001 \pm 0.014$	22.677

energy increased. The values of  $n$  about  $t$  and  $l$  do not show obvious change, and the values of  $n$  about  $b$  decreased when the collision energy increased. Besides, we found that there is no linear relationship  $\sigma(P/T)$  and  $\sqrt{s}$ , so the values of  $\chi^2/\text{dof}$  for this relationship are large which are listed in Table 4.

## 4. Conclusion

We summarize here our main observations and conclusions.

- We use the Tsallis-Pareto-type function to describe the transverse momentum cross-section spectrum of  $t\bar{t}$  different cross sections in pp collisions at 7, 8, and 13 TeV. The values of the effective temperature of the interacting system ( $T$ ) and the nonextensivity of the process ( $n$ ) parameters are extracted and listed in Table 1
- The rapidity cross sections of the spectrum of  $t\bar{t}$  different cross sections in pp collisions at 7, 8, and 13 TeV are analyzed by the three-source Landau hydrodynamic model. We have obtained the values of the contribution of central emission source ( $k_C$ ) and the width of rapidity distribution ( $\sigma_C$ ,  $\sigma_P$ ) and calculated the values of  $\chi^2/\text{dof}$ . The values of related parameters and  $\chi^2/\text{dof}$  are given in Table 2. In fact, because of the relationship  $k_T + k_C + k_P = 1$ ,  $k_T = k_P$ , and  $\sigma_T = \sigma_P$  (for the symmetric collision), we can calculate the contributions of the target and projectile source and the width of rapidity distribution of the target source

(c) We have plotted the relationship of free parameters and collision energy in Figure 17. For the particles of  $t$ ,  $l$ , and  $b$ ,  $\sigma(C)$  shows an increasing trend with the collision energy increased. And  $T$  shows a slight increase with the collision energy increased; this phenomenon may be affected by QGP

(d) As has been mentioned in Section 3, the initial temperature ( $T_i$ ) can be described by  $\sqrt{\langle p_T^2 \rangle / 2}$  approximately. In order to understand the excitation degree of the interacting system, we calculated the values of  $\langle p_T \rangle$  and  $\sqrt{\langle p_T^2 \rangle / 2}$  by the curves in Figures 1, 3, 5, and 7. We found that the values of  $\langle p_T \rangle$  and  $\sqrt{\langle p_T^2 \rangle / 2}$  are large; this could mean the high excitation degree of the interacting system

## Data Availability

The data used to support the findings of this study are included within the article.

## Ethical Approval

The authors declare that they are in compliance with ethical standards regarding the content of this paper.

## Conflicts of Interest

The authors declare that they have no conflicts of interest regarding the publication of this paper.

## Acknowledgments

This work is supported by Scientific and Technological Innovation Programs of Higher Education Institutions in Shanxi under Grant No. 2019L0804, the National Natural Science Foundation of China under Grant No. 11847003, and the university student innovation and entrepreneurship training program of Taiyuan Normal University No. CXCX 2084. This work has been published at <http://arxiv.org/abs/2007.12445>.

## References

- [1] CDF Collaboration, "Evidence for top quark production in  $p\bar{p}$  collisions at  $\sqrt{s} = 1.8$  TeV," *Physical Review Letters*, vol. 73, p. 225, 1994.
- [2] CDF Collaboration, "Observation of top quark production in  $p\bar{p}$  collisions with the collider detector at Fermilab," *Physical Review Letters*, vol. 74, no. 14, pp. 2626–2631, 1995.
- [3] D0 Collaboration, "Observation of the top quark," *Physical Review Letters*, vol. 74, no. 14, pp. 2632–2637, 1995.
- [4] CMS Collaboration, "Measurement of charged pion, kaon, and proton production in proton-proton collisions at  $\sqrt{s}=13$ TeV," *Physical Review D*, vol. 96, no. 11, article 112003, 2017.
- [5] X. W. He, H. R. Wei, and F. H. Liu, "Chemical potentials of light hadrons and quarks from yield ratios of negative to positive particles in high energy pp collisions," *Journal of Physics G: Nuclear and Particle Physics*, vol. 46, no. 2, article 025102, 2019.

- [6] L. N. Gao, F. H. Liu, Y. Sun, Z. Sun, and R. A. Lacey, "Excitation functions of parameters extracted from three-source (net)proton rapidity distributions in Au-Au and Pb-Pb collisions over an energy range from AGS to RHIC," *The European Physical Journal A*, vol. 53, no. 3, p. 61, 2017.
- [7] CMS collaboration, "Measurements of  $t\bar{t}$  differential cross sections in proton-proton collisions at  $\sqrt{s} = 13$  TeV using events containing two leptons," *Journal of High Energy Physics*, vol. 2019, no. 2, p. 149, 2019.
- [8] F. H. Liu, Y. Q. Gao, T. Tian, and B.-C. Li, "Unified description of transverse momentum spectrums contributed by soft and hard processes in high-energy nuclear collisions," *The European Physical Journal A*, vol. 50, no. 6, p. 94, 2014.
- [9] L. N. Gao and F. H. Liu, "Comparing Erlang distribution and Schwinger mechanism on transverse momentum spectra in high energy collisions," *Advances in High Energy Physics*, vol. 2016, Article ID 1505823, 15 pages, 2016.
- [10] L. N. Gao, F. H. Liu, and R. A. Lacey, "Excitation functions of parameters in Erlang distribution, Schwinger mechanism, and Tsallis statistics in RHIC BES program," *The European Physical Journal A*, vol. 52, no. 5, p. 137, 2016.
- [11] UA1 Collaboration, "Transverse momentum spectra for charged particles at the CERN proton-antiproton collider," *Physics Letters B*, vol. 118, no. 1-3, pp. 167-172, 1982.
- [12] R. Odorico, "Does a transverse energy trigger actually trigger on large-PT jets?," *Physics Letters B*, vol. 118, no. 1-3, pp. 151-154, 1982.
- [13] T. Mizoguchi, M. Biyajima, and N. Suzuki, "Analyses of whole transverse momentum distributions in  $p\bar{p}$  and  $pp$  collisions by using a modified version of Hagedorn's formula," *International Journal of Modern Physics A: Particles and Fields; Gravitation; Cosmology; Nuclear Physics*, vol. 32, no. 11, article 1750057, 2017.
- [14] L. N. Gao, F. H. Liu, and B. C. Li, "Rapidity dependent transverse momentum spectra of heavy quarkonia produced in small collision systems at the LHC," *Advances in High Energy Physics*, vol. 2019, Article ID 6739315, 17 pages, 2019.
- [15] J. Schwinger, "On gauge invariance and vacuum polarization," *Physics Review*, vol. 82, no. 5, pp. 664-679, 1951.
- [16] R. C. Wang and C. Y. Wong, "Finite-size effect in the Schwinger particle-production mechanism," *Physical Review D*, vol. 38, no. 1, pp. 348-359, 1988.
- [17] C. Tsallis, "Possible generalization of Boltzmann-Gibbs statistics," *Journal of Statistical Physics*, vol. 52, no. 1-2, pp. 479-487, 1988.
- [18] W. M. Alberico and A. Lavagno, "Non-extensive statistical effects in high-energy collisions," *The European Physical Journal A*, vol. 40, no. 3, p. 313, 2009.
- [19] G. Wilk and Z. Wlodarczyk, "Multiplicity fluctuations due to the temperature fluctuations in high-energy nuclear collisions," *Physical Review C*, vol. 79, no. 5, article 054903, 2009.
- [20] J. Cleymans, G. I. Lykasov, A. S. Parvan, A. S. Sorin, O. V. Teryaev, and D. Worku, "Systematic properties of the Tsallis distribution: energy dependence of parameters in high energy  $p$ - $p$  collisions," *Physics Letters B*, vol. 723, no. 4-5, pp. 351-354, 2013.
- [21] J. Cleymans and D. Worku, "Relativistic thermodynamics: transverse momentum distributions in high-energy physics," *The European Physical Journal A*, vol. 48, no. 11, p. 160, 2012.
- [22] C. Y. Wong and G. Wilk, "Tsallis fits to  $p_T$  spectra and multiple hard scattering in  $pp$  collisions at the LHC," *Physical Review D*, vol. 87, no. 11, article 114007, 2013.
- [23] P. Carruthers and M. Duong-van, "New scaling law based on the hydrodynamical model of particle production," *Physics Letters B*, vol. 41, no. 5, pp. 597-601, 1972.
- [24] P. Carruthers and M. Duong-van, "Rapidity and angular distributions of charged secondaries according to the hydrodynamical model of particle production," *Physical Review D*, vol. 8, no. 3, pp. 859-874, 1973.
- [25] C. Y. Wong, "Landau hydrodynamics reexamined," *Physical Review C*, vol. 78, no. 5, article 054902, 2008.
- [26] The CMS Collaboration, "Object definitions for top quark analyses at the particle level," Technical Report No. CMS-NOTE-2017-004. CERN-CMS-NOTE-2017-004, CERN, Geneva, 2017.
- [27] L. J. Gutay, A. S. Hirsch, R. P. Scharenberg, B. K. Srivastava, and C. Pajares, "De-confinement in small systems: clustering of color sources in high multiplicity  $pp$  collisions at  $s = 1.8$  TeV," *International Journal of Modern Physics E: Nuclear Physics*, vol. 24, no. 12, article 1550101, 2015.
- [28] A. S. Hirsch, C. Pajares, R. P. Scharenberg, and B. K. Srivastava, "De-confinement in high multiplicity proton-proton collisions at LHC energies," 2018, <https://arxiv.org/abs/1803.02301>.
- [29] P. Sahoo, S. De, S. K. Tiwari, and R. Sahoo, "Energy and centrality dependent study of deconfinement phase transition in a color string percolation approach at RHIC energies," *The European Physical Journal A*, vol. 54, article 136, 2018.
- [30] The CMS Collaboration, "Measurement of differential top-quark-pair production cross sections in  $pp$  collisions at  $\sqrt{s} = 7$  TeV," *European Physical Journal C*, vol. 73, no. 3, article 2339, 2013.
- [31] The CMS Collaboration, "Measurement of the differential cross section for top quark pair production in  $pp$  collisions at  $\sqrt{s} = 8$  TeV," *European Physical Journal C*, vol. 75, no. 11, p. 542, 2015.
- [32] H. R. Wei and F. H. Liu, "A study of transverse momentum distributions of jets produced in p-p, p-p, d-Au, Au-Au, and Pb-Pb collisions at high energies," *Advances in High Energy Physics*, vol. 2015, Article ID 263135, 17 pages, 2015.

## Research Article

# Calculation of Binding Energy and Wave Function for Exotic Hidden-Charm Pentaquark

F. Chezani Sharahi<sup>1,2</sup> and M. Monemzadeh<sup>1</sup> 

<sup>1</sup>Department of Physics, University of Kashan, Iran

<sup>2</sup>Department of Physics, University of Arak, Iran

Correspondence should be addressed to M. Monemzadeh; monem@kashanu.ac.ir

Received 8 August 2020; Revised 5 March 2021; Accepted 11 April 2021; Published 21 April 2021

Academic Editor: Edward Sarkisyan Grinbaum

Copyright © 2021 F. Chezani Sharahi and M. Monemzadeh. This is an open access article distributed under the Creative Commons Attribution License, which permits unrestricted use, distribution, and reproduction in any medium, provided the original work is properly cited. The publication of this article was funded by SCOAP<sup>3</sup>.

In this study, pentaquark  $P_c(4380)$  composed of a baryon  $\Sigma_c$ , and a  $\bar{D}^*$  meson is considered. Pentaquark is as a bound state of two-body systems composed of a baryon and a meson. The calculated potential will be expanded and replaced in the Schrödinger equation until tenth sentences of expansion. Solving the Schrödinger equation with the expanded potential of Pentaquark leads to an analytically complete approach. As a consequence, the binding energy  $E_B$  of pentaquark  $P_c$  and wave function is obtained. The results  $E_B$  will be presented in the form of tables so that we can review the existence of pentaquark  $P_c$ . Then, the wave function will be shown on diagrams. Finally, the calculated results are compared with the other obtained results, and the mass of observing pentaquark  $P_c$  and the radius of pentaquark are estimated.

## 1. Introduction

In the first researches, the existence of multi-quark states is illustrated in its simplest possible form, in which baryons are made of three fundamental quarks and mesons from a quark and an antiquark [1]. Indeed, from the point of view of the mathematics and physics, there was no QCD theorem opposing the existence of exotic multi-quark. In gauge field theory, the QCD principle allows the existence of multi-quarks and hybrids, which include quark and gluonic degrees of freedom [2].

The search for the pentaquark and its probing has a long history. About ten years ago, in the study of pentaquark, a big progress was occurred when LEPS collaborations started a search with a claim to find out strong evidence of the pentaquark with the mass of about 1.540 GeV [3]. Then, many theoretical and experimental approaches were pursued, and many ideas were proposed in this field. For example, Zou and his colleagues suggested that the components of pentaquark can be included in nucleon. Since the heavy quarks play an important role in stabilization of multi-quark systems and these play exactly the same role as the hydrogen mole-

cule in QED [4–7], there are theoretical predictions about exotic hidden-charm pentaquark. In particular, the possibility of the existence of hidden-charm molecular baryons composed of an anticharmed meson and a charmed baryon was systematically studied within the one boson exchange model [3].

In 2003, LEPS collaboration reported the evidence of pentaquark  $s$  state with content of quark  $uudd\bar{s}$  having a very narrow width [8]. Unfortunately, this exotic flavor was not confirmed in subsequent experiments [9, 10]. In fact, the possible theoretical arguments are presented for the nonexistence of a stable pentaquark  $s$  in the references [11, 12]. Also, this mode has not been found with a light flavor yet. However, the baryons with light flavor may be able to have a significant pentaquark components [2].

A decade ago, numerous researches were conducted around the world to find exotic particles. The result of these efforts was the observation of the mesonic  $X$ ,  $Y$ , and  $Z$  particles in Belle, BESIII, BABAR, and LHCb. Some of these were considered as candidates for exotic states because they do not fit in a regular mesonic structure [1]. The common point of the exotic states is that all of these contain the heavy quarks and antiquarks.

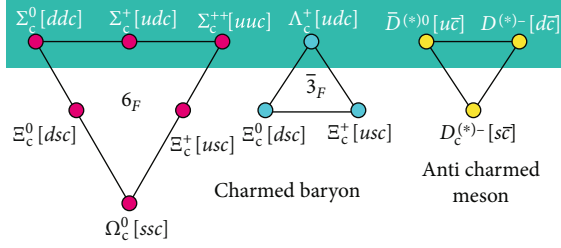


FIGURE 1: (color line) The  $s$ -wave charmed baryons with  $J^P = 1/2^+$  and pseudoscalar or vector  $s$ -wave charmed mesons which form the molecular baryons with double charm [6].

Due to the heavy quarks, the exotic states can be stable, and light modes can be combined with a regular mode [13]. This estimation is consistent with the fact that all of the exotic states have a hidden  $c$  or  $b$  which is experimentally observed. If this claim is valid that the heavy components stabilize multi-quark systems by particle physics scientists, it will be a natural proposal from their experimental colleagues to search for exotic states consisting of clear quarks  $c$  and  $b$ , for example,  $b\bar{c}qq'$  [2].

Here, one hidden-charm molecular baryon composed of an anticharmed meson and a charmed baryon has been studied. This can have one of the two flavors, i.e., symmetric  $6_F$  or antisymmetric flavor  $\bar{3}_F$  as shown in Figure 1. So, spin parity of  $s$ -wave charmed baryon is  $J^P = 1/2^+$  or  $J^P = 3/2^+$  for  $6_F$  and  $J^P = 1/2^+$  for  $\bar{3}_F$ . The pseudoscalar or vector anticharmed meson is made of  $s$ -wave anticharmed mesons. In Figure 1, hidden-charm molecular states composed of the anticharmed mesons and the charmed baryons are placed inside the green range [6].

Recently, LHCb collaboration has observed two resonance structures  $P_c(4380)$  and  $P_c(4450)$  with mass and width decay  $M_{P_c(4380)} = 4380 \pm 8 \pm 29 \text{ MeV}$ ,  $\Gamma_{P_c(4380)} = 205 \pm 18 \pm 86 \text{ MeV}$  and  $M_{P_c(4450)} = 4449.8 \pm 1.7 \pm 2.5 \text{ MeV}$ ,  $\Gamma_{P_c(4450)} = 39 \pm 5 \pm 19 \text{ MeV}$  in the invariant mass spectrum  $J/\psi p$  from  $\Lambda_b \rightarrow J/\psi p K$ . According to the final state  $J/\psi p$ , it is concluded that two observing states  $P_c$  cannot be isosinglet, and these consist of hidden-charm quantum numbers. Also, it is suggested that structures for each of the states  $P_c$  are considered for  $P_c(4380)$ ,  $\Sigma_c(2455)\bar{D}^*$  and  $P_c(4450)$ ,  $\Sigma_c^*(2520)\bar{D}^*$  [2, 3].

Binding energy may be calculated analytically by solving Schrödinger equation with the expanded potential of Pentaquark. This approach offers advantages over numerical solution of the Schrödinger equation for pentaquark. First, all values for binding energy can be calculated, and this is done more accurately. Second wave function can be computed and presented graphically ( $\phi(r)$  versus  $r$ ), from which useful particle characteristics and data could be extracted.

In this work, this is described by analytical solution of pentaquark  $\Sigma_c\bar{D}^*$  in four sections: where apart from the introduction in section 1, the potential of pentaquark  $P_c(4380)$  is discussed in section 2. Then, using the potential of pentaquark, the Schrödinger equation is analytically solved in section 3. Finally, important conclusions are discussed in section 4.

TABLE 1: ( $E_B(\text{MeV}), M_{P_c}(\text{MeV})$ ) for  $P_c(4380)$  and  $g_1 = 0.94$ .

$\Lambda(\text{MeV})$	$g = 0.51$	$g = 0.59$	$g = 0.67$
800	(-63, 4400.32)	(-40, 4423.32)	(-17, 4446.32)
850	(-62, 4401.32)	(-34, 4429.32)	(-6.7, 4456.62)
900	(-59, 4404.32)	(-26, 4437.32)	—
1000	(-45, 4418.32)	(-0.11, 4463.21)	—
1100	(-22, 4441.32)	—	—

TABLE 2: ( $E_B(\text{MeV}), M_{P_c}(\text{MeV})$ ) for  $P_c(4380)$  and  $g_1 = 0.75$ .

$\Lambda(\text{MeV})$	$g = 0.51$	$g = 0.59$	$g = 0.67$
800	(-90, 4373.32)	(-73, 4390.32)	(-56, 4407.32)
850	(-95, 4368.32)	(-75, 4390.32)	(-53, 4407.32)
900	(-99, 4364.32)	(-74, 4389.32)	(-49, 4414.32)
1000	(-102, 4361.32)	(-67, 4369.32)	(-32, 4431.32)
1100	(-98, 4365.32)	(-51, 4412.32)	(-3.14, 4460.18)
1200	(-86, 4377.32)	—	—

TABLE 3: ( $E_B(\text{MeV}), M_{P_c}(\text{MeV})$ ) for  $P_c(4380)$  and  $\Lambda = 800 \text{ MeV}$ .

$g_1$	$g = 0.51$	$g = 0.59$	$g = 0.67$
0.75	(-15.99, 4447.33)	(-15.80, 4447.52)	(-15.62, 4447.7)
0.94	—	(-15.47, 4447.85)	(-15.27, 4448.05)
1.95	—	(-14.01, 4449.32)	—

## 2. The Potential of Pentaquark $P_c$ and Its Expansion

Pentaquark is considered to be composed of one baryon and one meson. For pentaquark, with such a structure, the potential is given as follows [2]:

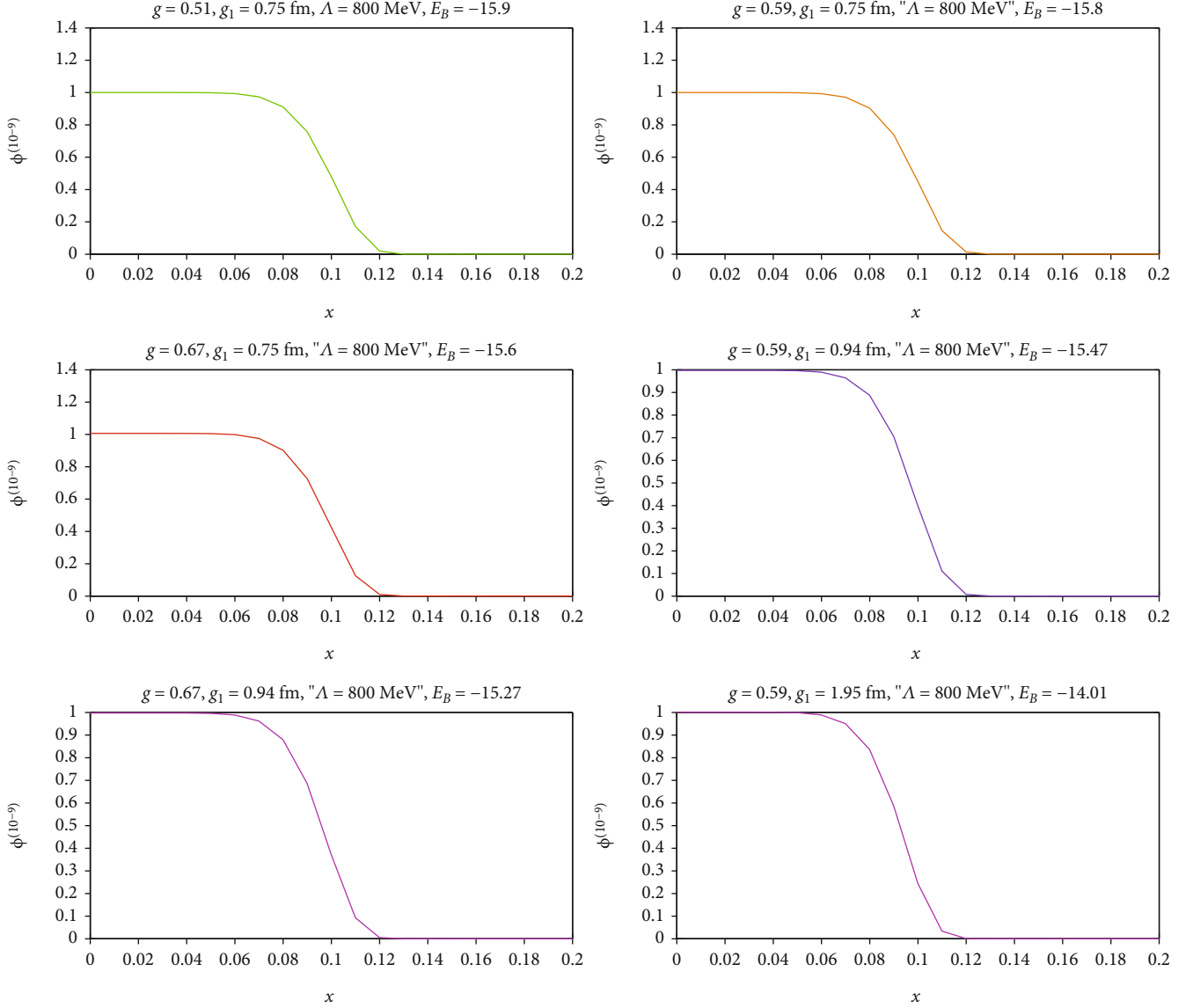
$$V_{\Sigma_c\bar{D}^*}(r) = \frac{1}{3} \frac{gg_1}{f_\pi} \nabla^2 Y(\Lambda, m_\pi, r) \mathcal{F}_0 \mathcal{G}_0, \quad (1)$$

where the coupling constant  $g = 0.59 \pm 0.07 \pm 0.01$  is extracted from the width of  $D^*$  [14, 15],  $g_1 = 0.75, 0.94, 1.95$  [6, 16]. Also, it is the mass of pion  $m_\pi = 135 \text{ MeV}$  and pion decay constant  $f_\pi = 132 \text{ MeV}$  [2]. The amount of phenomenological cutoff parameter is considered  $\Lambda = 0.8 \text{ GeV} - 2.5 \text{ GeV}$  [2, 12]. Finally, the  $Y(\Lambda, m_\pi, r)$  is [2]:

$$Y(\Lambda, m_\pi, r) = \frac{1}{4\pi r} (e^{-m_\pi r} - e^{-\Lambda r}) - \frac{\Lambda^2 - m_\pi^2}{8\pi\Lambda} e^{-\Lambda r}. \quad (2)$$

Now, we are calculating and expanding  $\nabla^2 Y$ :

$$\begin{aligned} \nabla^2 Y(\Lambda, m_\pi, r) &= \frac{m_\pi^2}{4\pi r} (e^{-m_\pi r} - e^{-\Lambda r}) - \frac{\Lambda^3 - m_\pi^2 \Lambda}{8\pi} e^{-\Lambda r} \\ &= \frac{1}{4\pi} (b_0 + b_1 r + b_2 r^2 + b_3 r^3 + b_4 r^4 + b_5 r^5 + b_6 r^6 + b_7 r^7 \\ &\quad + b_8 r^8 + b_9 r^9 + \dots), \end{aligned} \quad (3)$$

FIGURE 2:  $P_c(4380)$  at  $r$  in  $\Lambda = 800\text{MeV}$  for different values of  $g$  and  $g_1$ .

where

$$\begin{aligned}
 b_0 &= \left(-m^3 + \frac{\Lambda^3}{2} + \frac{m^2\Lambda}{2}\right); b_1 = \left(\frac{m^4}{2} - \frac{\Lambda^4}{2}\right), \\
 b_2 &= \left(-\frac{m^5}{3!} + \frac{\Lambda^5}{2 \times 2!} - \frac{m^2\Lambda^3}{6 \times 2!}\right); b_3 = \left(\frac{m^6}{4!} - \frac{\Lambda^6}{2 \times 3!} + \frac{m^2\Lambda^4}{4 \times 3!}\right), \\
 b_4 &= \left(-\frac{m^7}{5!} + \frac{\Lambda^7}{2 \times 4!} - \frac{3m^2\Lambda^5}{6 \times 4!}\right); b_5 = \left(\frac{m^8}{6!} - \frac{\Lambda^8}{2 \times 5!} + \frac{m^2\Lambda^6}{3 \times 5!}\right), \\
 b_6 &= \left(-\frac{m^9}{7!} + \frac{\Lambda^9}{2 \times 6!} - \frac{5m^2\Lambda^7}{14 \times 6!}\right); b_7 = \left(\frac{m^{10}}{8!} - \frac{\Lambda^{10}}{2 \times 7!} + \frac{3m^2\Lambda^8}{8 \times 7!}\right), \\
 b_8 &= \left(-\frac{m^{11}}{9!} + \frac{\Lambda^{11}}{2 \times 8!} - \frac{7m^2\Lambda^9}{18 \times 8!}\right); b_9 = \left(\frac{m^{12}}{10!} - \frac{\Lambda^{12}}{2 \times 9!} + \frac{2m^2\Lambda^{10}}{5 \times 9!}\right).
 \end{aligned} \tag{4}$$

### 3. Solving the Schrödinger Equation for Pentaquark $P_c$

To investigate the existence of one bound state of pentaquark, we solve the Schrödinger equation with calculated potential in previous section for pentaquark  $P_c$ .

The radial Schrödinger equation for two-body systems is

$$\left(\frac{d^2}{dr^2} + \frac{2}{r} \frac{d}{dr} - \frac{l(l+1)}{r^2}\right) R_{n,l}(r) + \frac{2\mu}{\hbar} (E - V(r)) R_{n,l}(r) = 0. \tag{5}$$

Taking  $\hbar = 1$  and changing the variable  $\phi(r) = rR_{n,l}(r)$ ,

Eq. (5) becomes

$$\frac{d^2}{dr^2} \phi(r) + 2\mu \left( E - V(r) - \frac{l(l+1)}{2\mu r^2} \right) \phi(r) = 0. \quad (6)$$

By placing the potential  $V(r) = V_{\Sigma_c \bar{D}^*}(r)$  and the expanded shape of  $\nabla^2 Y$  in Eq. (6), an equation is expressed as follows:

$$\begin{aligned} \frac{d^2}{dr^2} \phi(r) + 2\mu (E - C_0 - C_1 r - C_2 r^2 - C_3 r^3 - C_4 r^4 - C_5 r^5 \\ - C_6 r^6 - C_7 r^7 - C_8 r^8 - C_9 r^9 + \dots - \frac{l(l+1)}{2\mu r^2}) \phi(r) = 0, \end{aligned} \quad (7)$$

where

$$C_n = B_1 b_n; n = 0, 1, \dots, 9; B_1 = \frac{1}{12\pi} \frac{g g_1}{f_\pi^2} \mathcal{F}_0 \mathcal{G}_0. \quad (8)$$

In Eq. (8), for  $\Sigma_c \bar{D}^*$  with  $I = 1/2, J = 3/2$ , it is placing the numerical value of  $\mathcal{F}_0 \mathcal{G}_0 = 1$  product from literature [2].

By considering the following, the proposed reply (cf. [17, 18]) for the differential Eq. (7) yields

$$\phi(r) = N(r) e^{M(r)} = r^n e^{M(r)}. \quad (9)$$

Differentiating second degree of  $\phi$  in Eq.(9) gives

$$\phi''(r) = \left( n(n-1)r^{-2} + 2nM'r^{-1} + M'' + M'^2 \right) r^n e^M. \quad (10)$$

Here, we are solving differential equation (7) by considering expansion  $V(r)$  up to the  $10^{th}$  order for calculating binding energy  $E_B$  of pentaquark. Hence, an approximation was attempted up to the  $10^{th}$  order, which not only expanded the potential behavior up to the  $10^{th}$  order similar to the potential behavior in equation (1) but also the resulting of binding energy that has sufficient precision compared to numerical literature [2, 19]. This is indicating the adequacy of approximation.

Now, we can considered two position for  $\phi(r)$ . The first  $\phi(0) = 0$  is for  $n = 1$ , and the second  $\phi(0) = cte$  is considered for  $n = 0$  that  $cte$  means a constant. Thus, we study them in separate subsections.

**3.1. The Position  $\phi(0) = 0$ .** To considered  $\phi(0) = 0$  then  $M(r)$  yields [19]:

$$M(r) = a_1 r^2 + a_2 r^3 + a_3 r^4 + a_4 r^5 + a_5 r^6 + a_6 r^7 + a_7 r^8 + a_8 r^9 + a_9 r^{10}. \quad (11)$$

Replacing Eq. (11) into Eq. (10) and comparing two Eqs. of (7) and (10), the following expression (Eq.(12)) for  $r^{-2}$  is obtained in terms of  $l(l+1)$  in Eq.(8), as well as a system of

11 nonlinear equations expressed later:

$$n(n-1) = l(l+1). \quad (12)$$

In the base state, two values for  $n$ , namely,  $n = 0$  and  $n = 1$  are obtained that according to Eq. (9) and the condition  $\phi(0) = 0$ , the value  $n = 0$  could be unacceptable, and  $N(r) = r$  will be. Therefore,  $\phi(r)$  and  $\phi''(r)$  are obtained as follows:

$$\begin{aligned} \phi(r) &= r e^{M(r)}, \\ \phi''(r) &= \left( 2M' r^{-1} + M'' + M'^2 \right) r e^M. \end{aligned} \quad (13)$$

After replacing Eq. (11) in Eq. (13) and separately equal to the different powers of  $r$ , the following nonlinear equations are obtained:

$$\begin{aligned} 6a_1 &= -2\mu(E - C_0), \\ 12a_2 &= 2\mu C_1, \\ 20a_3 + 4a_1^2 &= 2\mu C_2, \\ 30a_4 + 12a_1 a_2 &= 2\mu C_3, \\ 42a_5 + 9a_2^2 + 16a_1 a_3 &= 2\mu C_4, \\ 56a_6 + 20a_1 a_4 + 24a_2 a_3 &= 2\mu C_5, \\ 72a_7 + 16a_3^2 + 24a_1 a_5 + 30a_2 a_4 &= 2\mu C_6, \\ 90a_8 + 28a_1 a_6 + 36a_2 a_5 + 40a_3 a_4 &= 2\mu C_7, \\ 110a_9 + 25a_4^2 + 32a_1 a_7 + 42a_2 a_6 + 48a_3 a_5 &= 2\mu C_8, \\ 132a_{10} + 36a_1 a_8 + 48a_2 a_7 + 56a_3 a_6 + 60a_4 a_5 &= 2\mu C_9. \end{aligned} \quad (14)$$

Here, by replacing the numerical values of constants for pentaquark  $P_c(4380)$ ,  $\Sigma_c = 2455 MeV$ , and  $\bar{D}^* = 2008.32 MeV$ , we obtained the binding energy of pentaquark [2]. In Tables 1 and 2, different values of binding energy from Eq. (14) for  $P_c(4380)$  have been shown.

In the tables above  $M_{P_c}$ , is calculated as follows:

$$M_{P_c} = M_{\Sigma_c} + M_{\bar{D}^*} + E_B. \quad (15)$$

According to the obtained values, it is observed that in  $g_1 = 0.75$ , the results for pentaquark mass are much closer to the  $M_{P_c(4380)}$ . Also, to check the results, one of the main differences between this paper and the other references [2, 20] is that the acceptable results are obtained for the  $M_{P_c(4380)}$  only in the  $800 MeV \leq \Lambda \leq 1200 MeV$ , and these cannot be found in  $\Lambda \geq 1200 MeV$ .

**3.2. The Position  $\phi(0) = cte$ .** Now, we considered  $\phi(0) = cte$ ; thus,  $M(r)$  will be as follows [19]:

$$M(r) = a_1 r + a_2 r^2 + a_3 r^3 + a_4 r^4 + a_5 r^5 + a_6 r^6 + a_7 r^7 + a_8 r^8 + a_9 r^9. \quad (16)$$

Here, replacing Eq. (15) into Eq. (10) and comparing it to Eq. (7), a similar equation is obtained by Eq. (12). In this position, i.e.,  $\phi(0) = cte$ , the value  $n = 0$  could be acceptable, and  $N(r) = 1$  will be. Therefore,  $\phi(r)$  and  $\phi''(r)$  are obtained as follows:

$$\begin{aligned}\phi(r) &= e^{M(r)}, \\ \phi''(r) &= \left(M'' + M'^2\right)e^M.\end{aligned}\quad (17)$$

The same as before, by replacing Eq.(15) in Eq.(16), 10 nonlinear equations are obtained, and we have

$$\begin{aligned}2a_2 + a_1^2 &= 2\mu(C_0 - E), \\ 6a_3 + 4a_1a_2 &= 2\mu C_1, \\ 12a_4 + 4a_2^2 + 6a_1a_3 &= 2\mu C_2, \\ 20a_5 + 8a_1a_4 + 12a_2a_3 &= 2\mu C_3, \\ 30a_6 + 9a_3^2 + 10a_1a_5 + 16a_2a_4 &= 2\mu C_4, \\ 42a_7 + 12a_1a_6 + 20a_2a_5 + 24a_3a_4 &= 2\mu C_5, \\ 56a_8 + 16a_4^2 + 14a_1a_7 + 24a_2a_6 + 30a_3a_5 &= 2\mu C_6, \\ 72a_9 + 16a_1a_8 + 28a_2a_7 + 36a_3a_6 + 40a_4a_5 &= 2\mu C_7, \\ 25a_5^2 + 18a_1a_9 + 32a_2a_8 + 42a_3a_7 + 48a_4a_6 &= 2\mu C_8, \\ 36a_2a_9 + 48a_3a_8 + 56a_4a_7 + 60a_5a_6 &= 2\mu C_9.\end{aligned}\quad (18)$$

Also, in this position for  $P_c(4380)$ , we obtained the binding energy of pentaquark and the numerical coefficients of wave function. Table 3 shows the amount of binding energy from Eq. (17) and  $\Lambda = 800\text{MeV}$  for  $P_c(4380)$ .

To confirm the existence of pentaquark states, binding energy must be negative, i.e.,  $E_B < 0$ . Also, the total mass of particles contributing of pentaquark (i.e., the sum of baryon  $\Sigma_c$  and meson  $\bar{D}^*$  masses) in addition to binding energy is closer to the mass of pentaquark  $P_c(4380)$ . Here, the obtained results indicate that the binding energy ranging  $-102 \leq E_B \leq -0.11$  for pentaquark  $P_c(4380)$  is negative. Also, it conforms to calculated results in the literatures [2, 20–23]. As mentioned above, obtained results are acceptable to a great extent, and they could be considered a clear evidence for the existence of a bound of five-quark state.

Figure 2 demonstrates the wave function's diagrams for pentaquark  $P_c$  in  $\Lambda = 800\text{MeV}$ , at different values of  $g$  and  $g_1$ . These charts tend to zero at the given value. As shown in the graphs, wave functions become zero in  $x \sim 0.12 - 0.13$ , indicating that the maximum pentaquark radius ranges from 23.67 to 25.64 fm.

## 4. Conclusions

In this article, the pentaquark  $P_c(4380)$  system consisting of baryon  $\Sigma_c$  and  $\bar{D}^*$  meson has been considered. The obtained potential for pentaquark in reference [2] was presented and expanded. Then, expanded potential was replaced in the Schrödinger equation, and that was solved as a bound state

of two-body systems. By solving this to analytically approach and according to the values of constants and cutoff, 10 nonlinear differential equations and binding energy  $E_B$  of pentaquark  $P_c$  and wave function coefficients were obtained. The resulting  $E_B$  and wave function were presented using tables and diagrams in the previous section, which could confirm the existence of a bound state of pentaquark  $P_c(4380)$ . Then, it is specified that the wave function plots tend to be zero at a given value. Therefore, the maximum radius of pentaquark  $P_c$  was found out which ranged from  $x = 23.67\text{fm}$  to  $x = 25.64\text{fm}$ . We observed that the calculated values matches with the findings of others regarding the mass of  $P_c(4380)$ . Also, the advantage of this paper lies in its method, which other references are numerically calculated, and this paper delivers the obtained results analytically. Hence, the results are more comprehensive and complete compared to them.

## Data Availability

The authors confirm that the data supporting the findings of this study are available within the article.

## Disclosure

This research was not receive specific funding; thus, funding agencies have no role in the design of this study, in analysis, or interpretation of the data in writing the manuscript, or in the decision to publish the results.

## Conflicts of Interest

The authors also declare that there is no conflict of interests regarding the publication of this paper.

## References

- [1] M. Gell-Mann, "A schematic model of baryons and mesons," *Physics Letters*, vol. 8, no. 3, pp. 214-215, 1964.
- [2] R. Chen, L. Xiang, L. Xue-Qian, and Z. Shi-Lin, "Identifying exotic hidden-charm pentaquarks," *Physical review letters*, vol. 115, no. 13, article 132002, 2015.
- [3] J. He, "D<sup>-</sup>Σc\* and D<sup>-</sup>\*Σc interactions and the LHCb hidden-charmed pentaquarks," *Physics Letters B*, vol. 753, pp. 547–551, 2016.
- [4] M. Karliner and J. L. Rosner, "New exotic meson and baryon resonances from doubly heavy hadronic molecules," *Physical review letters*, vol. 115, no. 12, article 122001, 2015.
- [5] J. J. Wu, R. Molina, E. Oset, and B. S. Zou, "Prediction of narrow N\* and Λ\* resonances with hidden charm above 4 GeV," *Physical review letters*, vol. 105, no. 23, article 232001, 2010.
- [6] Z. C. Yang, Z. F. Sun, J. He, X. Liu, and S. L. Zhu, "A note on the B\* B, B\* B\*, D\* D, D\* D\*, molecular states," *Chinese Physics C*, vol. 36, no. 6, 2012.
- [7] T. Uchino, W. H. Liang, and E. Oset, "Baryon states with hidden charm in the extended local hidden gauge approach," *The European Physical Journal A*, vol. 52, no. 3, pp. 1–6, 2016, <https://arxiv.org/abs/1504.05726>.
- [8] T. Nakano, D. S. Ahn, J. K. Ahn et al., "Evidence for a narrow S=+1 baryon resonance in photoproduction from the

- neutron," *Physical Review Letters*, vol. 91, no. 1, article 012002, 2003.
- [9] K. H. Hicks, "Experimental search for pentaquarks," *Progress in Particle and Nuclear Physics*, vol. 55, no. 2, pp. 647–676, 2005.
- [10] T. Liu, Y. Mao, and B. Q. Ma, "Present status on experimental search for pentaquarks," *International Journal of Modern Physics A*, vol. 29, no. 13, article 1430020, 2014.
- [11] C. Gignoux, B. Silvestre-Brac, and J. M. Richard, "Possibility of stable multiquark baryons," *Physics Letters B*, vol. 193, no. 2-3, pp. 323–326, 1987.
- [12] D. O. Riska and N. N. Scoccola, "Anti-charm and anti-bottom hyperons," *Physics Letters B*, vol. 299, no. 3-4, pp. 338–341, 1993.
- [13] X. Q. Li and X. Liu, "A possible global group structure for exotic states," *The European Physical Journal C*, vol. 74, no. 12, article 3198, 2014.
- [14] C. Isola, M. Ladisa, G. Nardulli, and P. Santorelli, "Charming penguin contributions in  $B \rightarrow K^* \pi, K(\rho, \omega, \phi)$  decays," *Physical Review D*, vol. 68, no. 11, article 114001, 2003.
- [15] X. Liu, Y.-R. Liu, W.-Z. Deng, and S.-L. Zhu, " $Z^+(4430)$  as  $a_1 D^*(D_1 D^*)$  molecular state," *Physical Review D*, vol. 77, no. 9, article 094015, 2008.
- [16] W. L. Wang, F. Huang, Z. Y. Zhang, and B. S. Zou, " $\Sigma_c D^-$  and  $\Lambda_c D^-$  states in a chiral quark model," *Physical Review C*, vol. 84, no. 1, article 015203, 2011.
- [17] F. Chezani Sharahi, M. Monemzadeh, and A. Abdoli Arani, "Bound state energy and wave function of tetraquark  $\bar{b}\bar{b}ud$  from lattice QCD potential," *Modern Physics Letters A*, vol. 34, article 1950220, no. 27, 2019.
- [18] F. Chezani Sharahi, M. Monemzadeh, and A. Abdoli Arani, "The Calculate of binding energy and wave function of tetraquark  $b\bar{b}s\bar{s}$  from lattice QCD potential with analytically approach," *Journal of Research on Many-body Systems*, vol. 9, no. 4, 2020.
- [19] E. Kreyszig, "Advanced engineering mathematics," John Wiley and Sons, 2010.
- [20] Y. Shimizu, S. Daiki, and H. Masayasu, "Coupled channel analysis of molecule picture of  $P_c(4380)$ ," *Physical Review D*, vol. 93, no. 11, article 114003, 2016.
- [21] M. Monemzadeh, N. Tazimi, and S. Babaghodrat, "Calculating masses of pentaquarks composed of baryons and mesons," *Advances in High Energy Physics*, vol. 2016, 4 pages, 2016.
- [22] M. Radin, S. Babaghodrat, and M. Monemzadeh, "Estimation of heavy baryon masses  $\Omega_{ccc}^{++}$  and  $\Omega_{bbb}^{-}$  by solving the Faddeev equation in a three-dimensional approach," *Physical review D*, vol. 90, no. 4, article 047701, 2014.
- [23] M. Monemzadeh, M. Hadizadeh, and N. Tazimi, "Identification of the mass and stability interval of strong potential in heavy mesons," *International Journal of Theoretical Physics*, vol. 50, no. 3, pp. 737–743, 2011.

## Research Article

# Study of Production of (Anti-)deuteron Observed in Au+Au Collisions at $\sqrt{s_{NN}} = 14.5, 62.4, \text{ and } 200 \text{ GeV}$

Ying Yuan <sup>1,2</sup>

<sup>1</sup>Mathematics and Physics Teaching and Research Section, College of Pharmacy, Guangxi University of Chinese Medicine, Nanning 530200, China

<sup>2</sup>Guangxi Key Laboratory of Nuclear Physics and Nuclear Technology, Guangxi Normal University, Guilin 541004, China

Correspondence should be addressed to Ying Yuan; wawayubao@qq.com

Received 18 June 2020; Revised 9 October 2020; Accepted 27 February 2021; Published 15 March 2021

Academic Editor: Bhartendu K. Singh

Copyright © 2021 Ying Yuan. This is an open access article distributed under the Creative Commons Attribution License, which permits unrestricted use, distribution, and reproduction in any medium, provided the original work is properly cited. The publication of this article was funded by SCOAP<sup>3</sup>.

Transverse momentum distributions of deuterons and antideuterons in Au + Au collisions at  $\sqrt{s_{NN}} = 14.5, 62.4, \text{ and } 200 \text{ GeV}$  with different centrality are studied in the framework of the multisource thermal model. Transverse momentum spectra are conformably and approximately described by the Tsallis distribution. The dependence of parameters (average transverse momenta, effective temperature, and entropy index) on event centrality is obtained. It is found that the parameters  $T$  increase and  $q$  decrease with increase of the average number of particles involved in collisions, which reveals the transverse excitation degree increases with collision centrality.

## 1. Introduction

The study of strongly interacting matter at extreme temperatures and densities is provided a chance by heavy ion collisions at ultrarelativistic energies [1–5]. The production mechanism of nuclei in ultrarelativistic heavy ion collisions deserves more investigation since it may give important message on the quantum chromodynamics (QCD) phase transition from quark-gluon plasma (QGP) to hadron gas (HG) [6, 7]. The RHIC is scheduled to run at the energies which are around the critical energy of phase transition from hadronic matter to QGP [8]. The theoretical study of nuclei and anti-nuclei has been undertaken for many years, for example, the thermal model and coalescence model [9–13]. In particular, the study of transport phenomena is major important to the understanding of many fundamental properties [14]. The spectra of transverse momentum of particles produced in high energy collisions are of high interest as soon as they provide us with an important information of the kinetic freeze-out state of the interacting system [15]. At the stage of kinetic freeze-out, the effective temperature is not a real temperature, and it describes the sum of excitation degree of the interacting system and the effect of transverse flow [16].

In this paper, using the Tsallis distribution [17–19] in the multisource thermal model to simulate the transverse momentum distributions of (anti-)deuterons in Au + Au collisions at RHIC, we compare them with experiment data taken from the STAR Collaboration [20]. The main purpose of this work is to extract the information on effective temperature, because it allows us to extract the kinetic freeze-out temperature.

## 2. The Model and Method

The model used in the present work is the multisource thermal model [21–23]. In this model, many emission sources are formed in high-energy nucleus-nucleus collisions. The different distributions can describe the emission sources and particle spectra, such as the Tsallis distribution, the standard (Boltzmann, Fermi-Dirac, and Bose-Einstein) distributions, the Tsallis+standard distributions [24–29], and the Erlang distribution [21]. The Tsallis distribution can be described by two or three standard distributions.

The experimental data of the transverse momentum spectrum of the particles are fitted by using the Tsallis distribution which can describe the temperature fluctuation in a

TABLE 1: Values of  $\mu$  corresponding to the curves in Au + Au collisions at  $\sqrt{s_{\text{NN}}} = 14.5$  GeV,  $\sqrt{s_{\text{NN}}} = 62.4$  GeV, and  $\sqrt{s_{\text{NN}}} = 200$  GeV for 0-10%, 10-20%, 20-40%, 40-60%, and 60-80% centralities.

$\sqrt{s_{\text{NN}}}$ (GeV)	Cross section	$\mu$ (MeV)
14.5	0-10%	$288.9 \pm 12.9$
	10-20%	$284.9 \pm 12.9$
	20-40%	$278.7 \pm 12.8$
	40-60%	$256.0 \pm 12.4$
	60-80%	$227.3 \pm 1.08$
62.4	0-10%	$66.1 \pm 5.3$
	10-20%	$65.4 \pm 5.2$
	20-40%	$60.7 \pm 5.2$
	40-60%	$54.1 \pm 5.2$
	60-80%	$44.6 \pm 5.9$
200	0-10%	$28.4 \pm 5.5$
	10-20%	$27.7 \pm 5.1$
	20-40%	$27.4 \pm 4.9$
	40-60%	$22.9 \pm 4.9$
	60-80%	$18.2 \pm 4.5$

few sources to give an average value. The Tsallis distribution has many function forms [17–19, 24–31]. In the rest frame of a considered source, we choose a simplified form of the joint probability density function of transverse momentum ( $p_T$ ) and rapidity ( $y$ ) [8],

$$f(p_T, y) \propto \frac{d^2N}{dydp_T} = \frac{gV}{(2\pi)^2} p_T \sqrt{p_T^2 + m_0^2} \cosh y \times \left[ 1 + \frac{q-1}{T} \left( \sqrt{p_T^2 + m_0^2} \cosh y - \mu \right) \right]^{-q/(q-1)}. \quad (1)$$

Here,  $N$  is the particle number,  $g$  is the degeneracy factor,  $V$  is the volume of emission sources,  $m_0$  is the rest mass of the studied particle,  $T$  is the temperature which describes averagely a few sources (local equilibrium states),  $q$  is the entropy index which describes the degree of nonequilibrium among different states, and  $\mu$  is the chemical potential which is related to  $\sqrt{s_{\text{NN}}}$  [32]. In the RHIC energy region, the values of  $\mu$  are shown in Table 1 [33]. We can extract the values of  $T$ ,  $q$ , and  $V$  from reproducing the particle spectra, where  $T$  and  $q$  are fitted independently for the studied particle and  $V$  is related to other parameters.

The Monte Carlo distribution generating method is used to obtain  $p_T$ . Let  $r_1$  denote the random numbers distributed uniformly in  $[0, 1]$ . A series of values of  $p_T$  can be obtained by

$$\int_0^{p_T} f_{p_T}(p_T) dp_T < r_1 < \int_0^{p_T+dp_T} f_{p_T}(p_T) dp_T. \quad (2)$$

Here,  $f_{p_T}$  is the transverse momentum probability density function which is an alternative representation of the Tsallis distribution as follows:

$$f_{p_T}(p_T) = \frac{1}{N} \frac{dN}{dp_T} = \int_{y_{\min}}^{y_{\max}} f(p_T, y) dy, \quad (3)$$

where  $y_{\max}$  and  $y_{\min}$  are the maximum and minimum rapidity, respectively.

Under the assumption of isotropic emission in the source rest frame, we use the Monte Carlo method to acquire the polar angle:

$$\theta = 2 \arcsin \sqrt{r_2}. \quad (4)$$

Here,  $r_2$  denotes the random numbers distributed uniformly in  $[0, 1]$ . Thus, we can obtain a series of values of momentum and energy due to the momentum  $p = p_T/\sin \theta$  and the energy  $E = \sqrt{p^2 + m_0^2}$ . Therefore, the corresponding values of rapidity can be obtained according to the definition of rapidity.

### 3. Results and Discussion

**3.1. Transverse Momentum Spectra.** Figure 1 demonstrates midrapidity ( $|y| < 0.3$ ) transverse momentum spectra for deuterons in Au + Au collisions at  $\sqrt{s_{\text{NN}}} = 14.5$  GeV for 0-10%, 10-20%, 20-40%, 40-60%, and 60-80% centralities. The symbols represent the experimental data of STAR Collaboration [20]. The solid lines are our calculated results fitted by using the Tsallis distribution based on eq. (1) in the region of midrapidity. The values of the related parameters  $T$  and  $q$  are given in Table 2 along with the  $\chi^2/\text{dof}$  ( $\chi^2$  and number of degree of freedom). It is found that the calculations of the Tsallis distribution are in keeping with the experimental data well.

In Figures 2 and 3, the curves and symbols are similar to Figure 1. Figure 2 demonstrates midrapidity ( $|y| < 0.3$ ) transverse momentum spectra for deuterons in Au + Au collisions at  $\sqrt{s_{\text{NN}}} = 200$  GeV for 0-10%, 10-20%, 20-40%, 40-60%, and 60-80% centralities. The values of the related parameters  $T$  and  $q$  are given in Tables 3 and 4 along with the  $\chi^2/\text{dof}$ . It is found that the calculations of the Tsallis distribution are in keeping with the experimental data well.

In Figures 4–6 demonstrates midrapidity ( $|y| < 0.3$ ) transverse momentum spectra for antideuterons in Au + Au collisions at  $\sqrt{s_{\text{NN}}} = 14.5$ , 62.4, and 200 GeV for 0-10%, 10-20%, 20-40%, 40-60%, and 60-80% centralities. The curves and symbols are similar to Figure 1. One can see that the calculations also can describe approximately the experimental data of antideuterons with different centrality intervals of event. The values of the related parameters  $T$  and  $q$  are given in Tables 2–4.

**3.2. Average Transverse Momenta.** Figure 7 presents the centrality dependence of deuterons and antideuterons average transverse momenta ( $\langle p_T \rangle$ ) at the midrapidity ( $|y| < 0.3$ ) for  $\sqrt{s_{\text{NN}}} = 14.5$ , 62.4, and 200 GeV. The hollow symbols are the experiment data taken from the Figures 1–6, and the solid

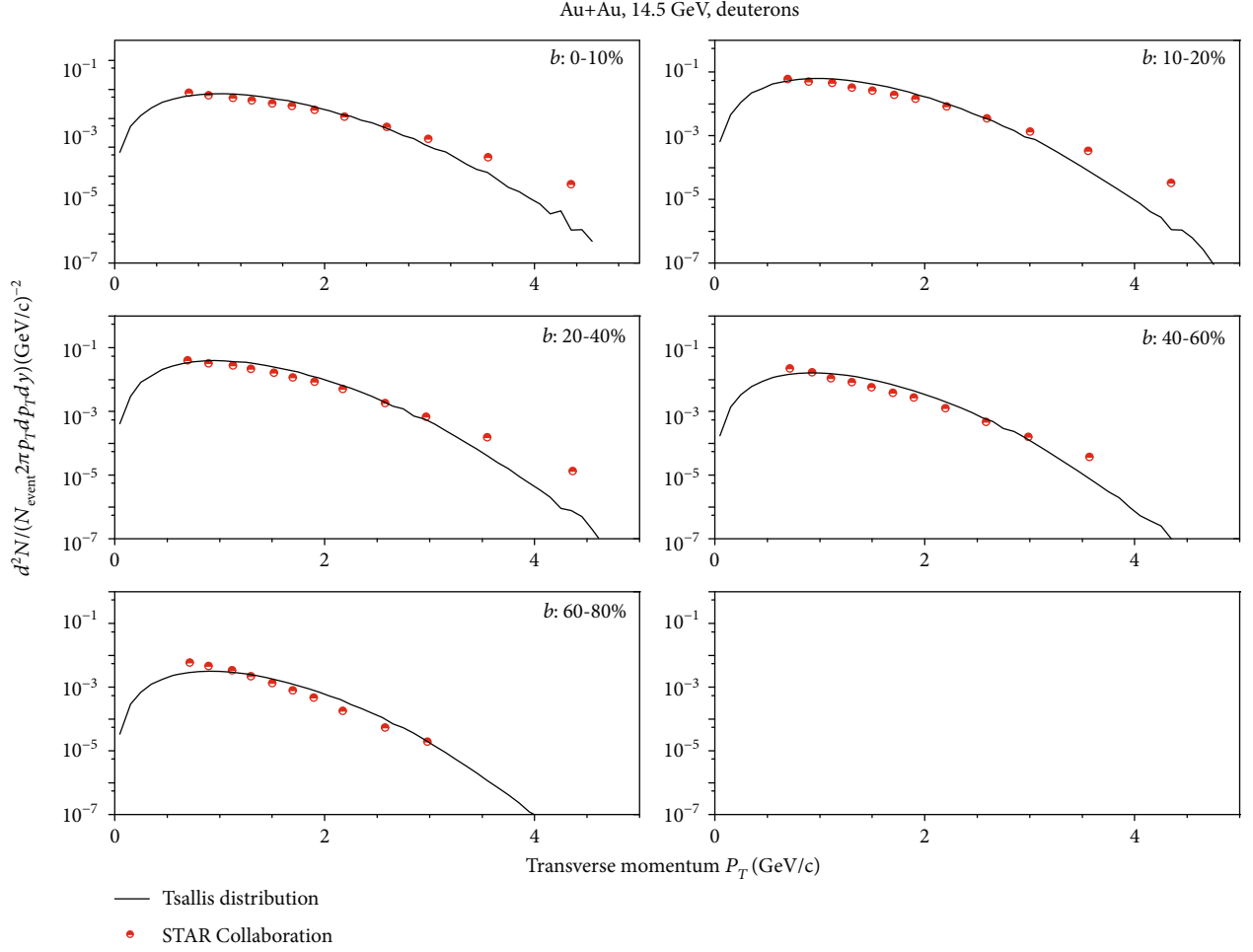


FIGURE 1: Deuteron transverse momentum spectra in Au + Au collisions at  $\sqrt{s_{NN}} = 14.5$  GeV for 0-10%, 10-20%, 20-40%, 40-60%, and 60-80% centralities. Calculations are shown by the solid lines. Experimental data taken from the STAR Collaboration [20] are represented by the symbols.

TABLE 2: Values of  $T$ ,  $q$ , and  $\chi^2/\text{dof}$  corresponding to the curves in Au + Au collisions at  $\sqrt{s_{NN}} = 14.5$  GeV for 0-10%, 10-20%, 20-40%, 40-60%, and 60-80% centralities. The “Ratios” is the average ratios of experimental data to model.

Figure	Type 1	Type 2	$T$ (GeV)	$q$	$\chi^2/\text{dof}$	Ratios
Figure 1	$d$	0-10%	$0.507 \pm 0.002$	$1.125 \pm 0.017$	0.055	0.805
		10-20%	$0.487 \pm 0.011$	$1.145 \pm 0.166$	0.053	0.742
		20-40%	$0.467 \pm 0.054$	$1.165 \pm 0.084$	0.119	0.788
		40-60%	$0.427 \pm 0.008$	$1.185 \pm 0.045$	0.150	0.848
		60-80%	$0.407 \pm 0.001$	$1.205 \pm 0.007$	0.639	1.191
Figure 4	$\bar{d}$	0-10%	$0.507 \pm 0.001$	$1.105 \pm 0.001$	0.564	0.884
		10-20%	$0.487 \pm 0.001$	$1.125 \pm 0.001$	0.239	1.005
		20-40%	$0.447 \pm 0.001$	$1.145 \pm 0.001$	0.331	0.939
		40-60%	$0.387 \pm 0.001$	$1.165 \pm 0.001$	0.619	0.914
		60-80%	$0.347 \pm 0.001$	$1.185 \pm 0.001$	1.508	0.960

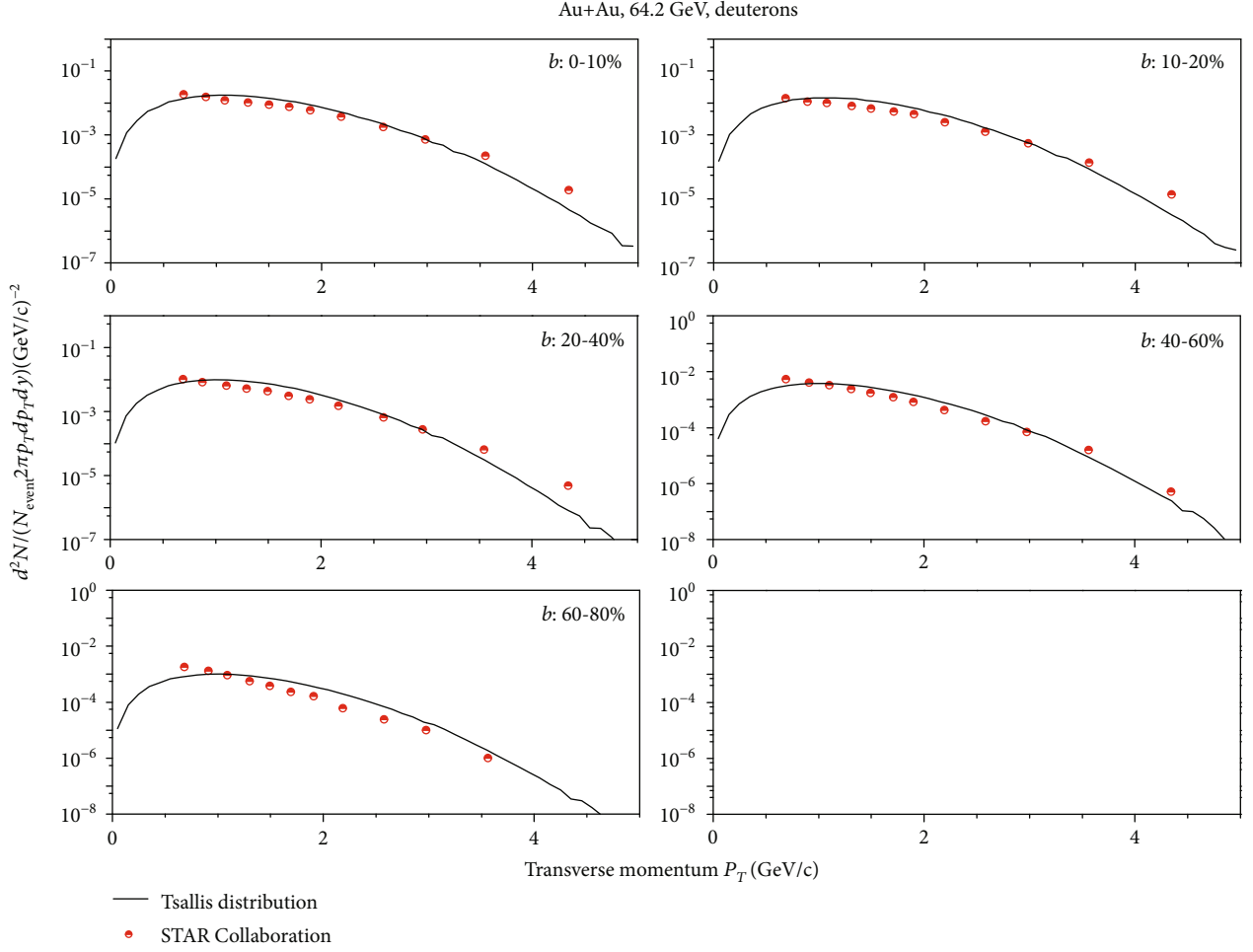


FIGURE 2: Deuteron transverse momentum spectra in Au + Au collisions at  $\sqrt{s_{\text{NN}}} = 62.4$  GeV for 0-10%, 10-20%, 20-40%, 40-60%, and 60-80% centralities. Calculations are shown by the solid lines. Experimental data taken from the STAR Collaboration [20] are represented by the symbols.

symbols are the calculations of the Tsallis distribution. The calculations can be obtained by

$$\langle p_T \rangle = \frac{\sum p_{T1} \alpha}{\sum \alpha}. \quad (5)$$

Here,  $p_{T1}$  is the value of transverse momentum corresponding to the experimental data, and  $\alpha$  is the value of  $d^2N / N_{\text{event}} 2\pi p_T dp_T dy$  that corresponds to the  $p_{T1}$ . In this figure, one sees that the calculations can describe the experimental data well in the range of the errors permitted. For deuterons, the values of average transverse momenta in the different incident energy get closer with decrease of centrality percentage. It has indicated that the transverse excitation degree increases with collision centrality.

**3.3. Dependence of Parameters on Number of Participating Nucleons.** Figures 8 and 9 give the change trends of parameters ( $T$  and  $q$ ) with the average number of participants for deuterons and antideuterons produced in Au + Au collision

at the midrapidity ( $|y| < 0.3$ ) for  $\sqrt{s_{\text{NN}}} = 14.5, 62.4,$  and  $200$  GeV. The symbols represent the parameter values extracted from Figures 1–6 and listed in Tables 2–4.

From Figures 8 and 9, we can see that the values of  $T$  parameters increase with decrease of centrality percentage, and the values of  $q$  parameters increase with increase of centrality percentage. Entropy is a physical quantity that represents the degree of chaos in the system. When a central collision occurs, the motion law of the final state particles is complex, and the whole system is in a higher state of order, so the entropy value is small. In the central region where the collision occurs, with the increase of the intensity of the collision, the corresponding effective temperature increases. The dependence of effective temperature on collision energy increases with the increase of collision energy. Under the same collision parameters, the entropy increases with the increase of collision energy, indicating that the higher the collision energy is, the more different microscopic states the particle may have, and the more disordered the system becomes. The kinetic freeze-out temperature can be extracted

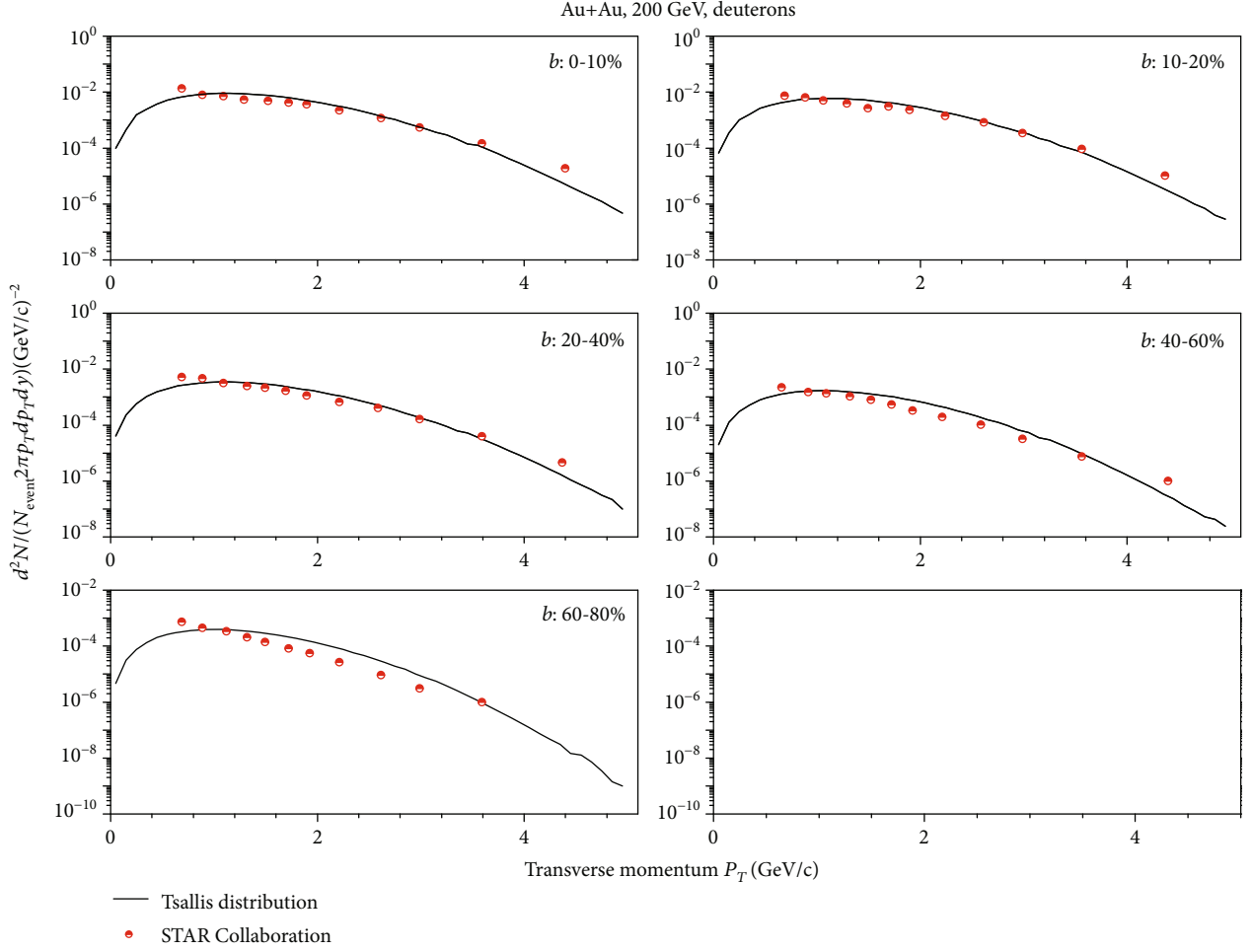


FIGURE 3: Deuteron transverse momentum spectra in Au + Au collisions at  $\sqrt{s_{\text{NN}}} = 200$  GeV for 0-10%, 10-20%, 20-40%, 40-60%, and 60-80% centralities. Calculations are shown by the solid lines. Experimental data taken from the STAR Collaboration [20] are represented by the symbols.

TABLE 3: Values of  $T$ ,  $q$ , and  $\chi^2/\text{dof}$  corresponding to the curves in Au + Au collisions at  $\sqrt{s_{\text{NN}}} = 62.4$  GeV for 0-10%, 10-20%, 20-40%, 40-60%, and 60-80% centralities. The “Ratios” is the average ratios of experimental data to model.

Figure	Type 1	Type 2	$T$ (GeV)	$q$	$\chi^2/\text{dof}$	Ratios
Figure 2	$d$	0-10%	$0.607 \pm 0.008$	$1.135 \pm 0.051$	0.037	0.785
		10-20%	$0.587 \pm 0.004$	$1.155 \pm 0.038$	0.061	0.711
		20-40%	$0.527 \pm 0.006$	$1.175 \pm 0.022$	0.124	0.731
		40-60%	$0.507 \pm 0.003$	$1.195 \pm 0.010$	0.107	0.887
		60-80%	$0.487 \pm 0.001$	$1.215 \pm 0.003$	0.274	0.910
Figure 5	$\bar{d}$	0-10%	$0.607 \pm 0.001$	$1.135 \pm 0.005$	2.527	0.712
		10-20%	$0.567 \pm 0.001$	$1.155 \pm 0.005$	1.464	0.834
		20-40%	$0.527 \pm 0.001$	$1.175 \pm 0.003$	2.231	0.833
		40-60%	$0.507 \pm 0.001$	$1.195 \pm 0.003$	2.099	1.095
		60-80%	$0.407 \pm 0.002$	$1.215 \pm 0.001$	3.303	0.966

TABLE 4: Values of  $T$ ,  $q$ , and  $\chi^2/\text{dof}$  corresponding to the curves in Au + Au collisions at  $\sqrt{s_{\text{NN}}} = 200$  GeV for 0-10%, 10-20%, 20-40%, 40-60%, and 60-80% centralities. The ‘‘Ratios’’ is the average ratios of experimental data to model.

Figure	Type 1	Type 2	$T$ (GeV)	$q$	$\chi^2/\text{dof}$	Ratios
Figure 3	$d$	0-10%	$0.667 \pm 0.004$	$1.145 \pm 0.021$	0.069	0.889
		10-20%	$0.647 \pm 0.004$	$1.175 \pm 0.017$	0.040	0.847
		20-40%	$0.627 \pm 0.008$	$1.195 \pm 0.036$	0.004	0.989
		40-60%	$0.567 \pm 0.001$	$1.215 \pm 0.006$	0.048	0.782
		60-80%	$0.507 \pm 0.001$	$1.235 \pm 0.003$	0.063	0.906
Figure 6	$\bar{d}$	0-10%	$0.667 \pm 0.001$	$1.145 \pm 0.005$	0.086	0.795
		10-20%	$0.647 \pm 0.001$	$1.165 \pm 0.005$	0.047	0.770
		20-40%	$0.627 \pm 0.001$	$1.195 \pm 0.004$	0.048	0.802
		40-60%	$0.607 \pm 0.001$	$1.215 \pm 0.002$	0.055	0.853
		60-80%	$0.597 \pm 0.001$	$1.255 \pm 0.001$	0.206	1.183

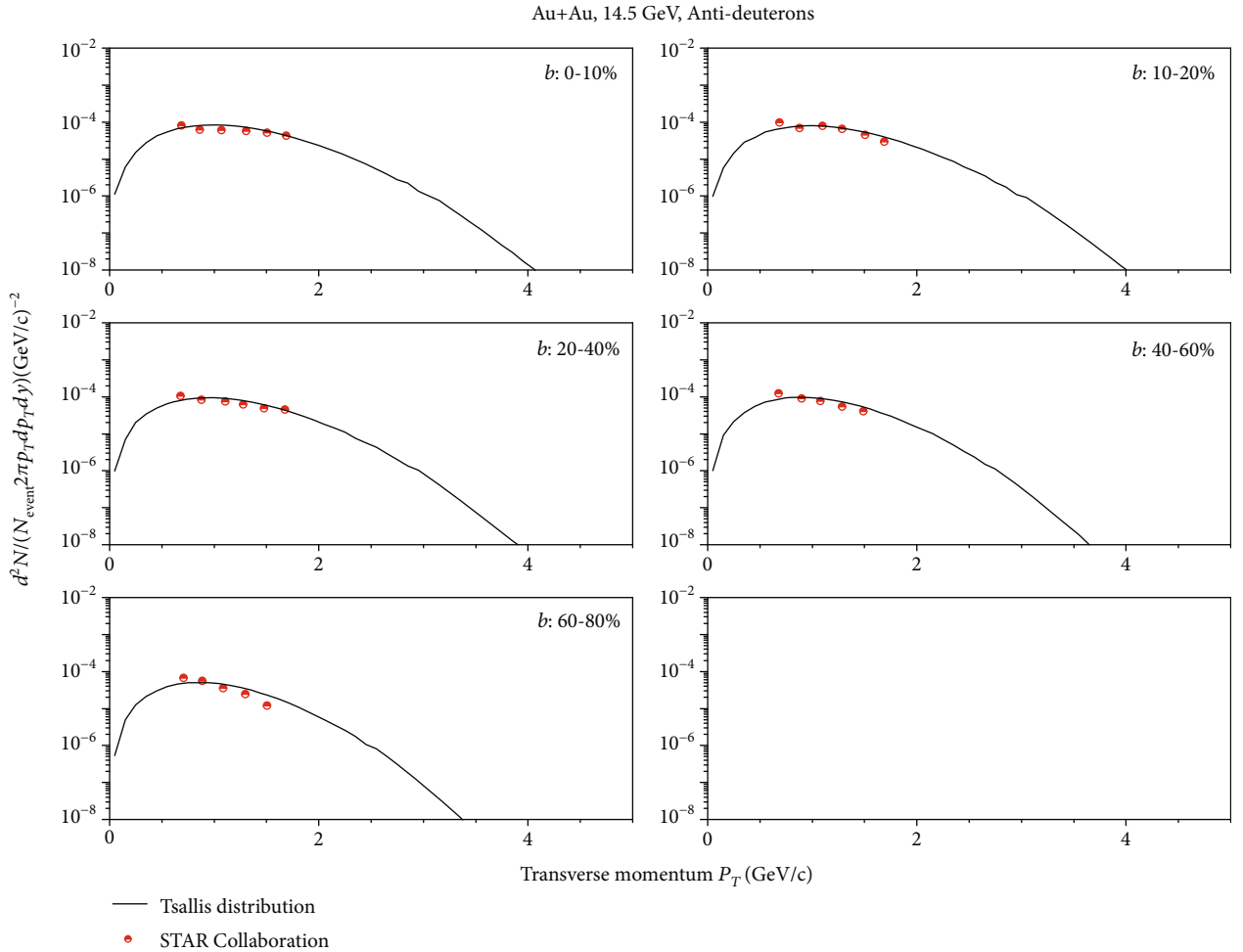


FIGURE 4: Antideuteron transverse momentum spectra in Au + Au collisions at  $\sqrt{s_{\text{NN}}} = 14.5$  GeV for 0-10%, 10-20%, 20-40%, 40-60%, and 60-80% centralities. Calculations are shown by the solid lines. Experimental data taken from the STAR Collaboration [20] are represented by the symbols.

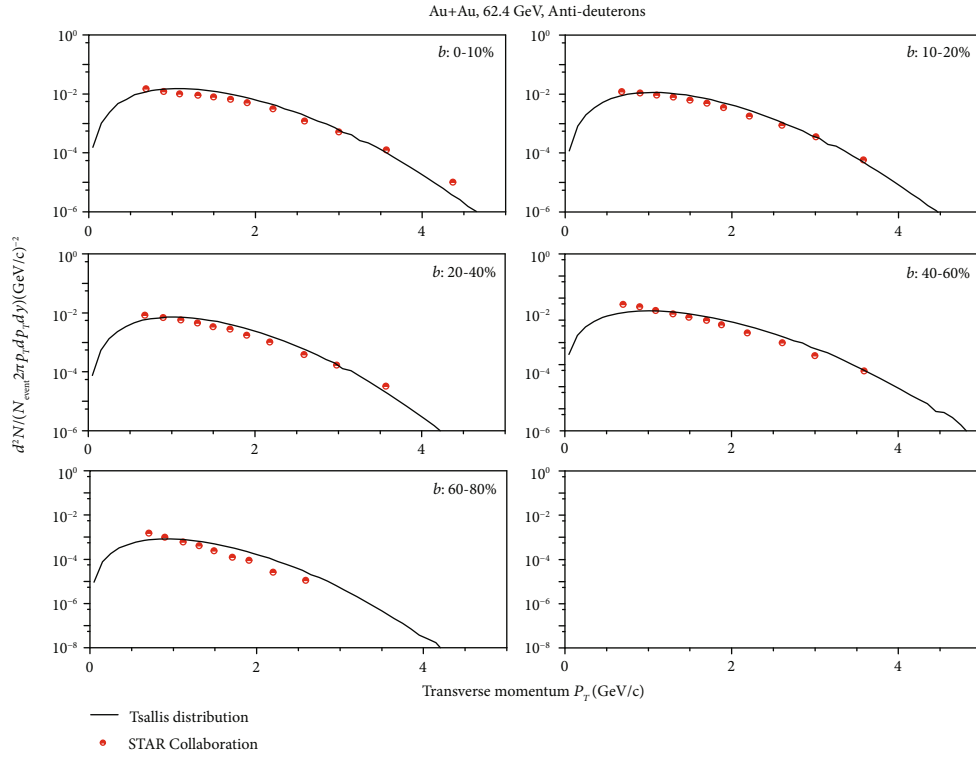


FIGURE 5: Antideuteron transverse momentum spectra in Au + Au collisions at  $\sqrt{s_{NN}} = 62.4$  GeV for 0-10%, 10-20%, 20-40%, 40-60%, and 60-80% centralities. Calculations are shown by the solid lines. Experimental data taken from the STAR Collaboration [20] are represented by the symbols.

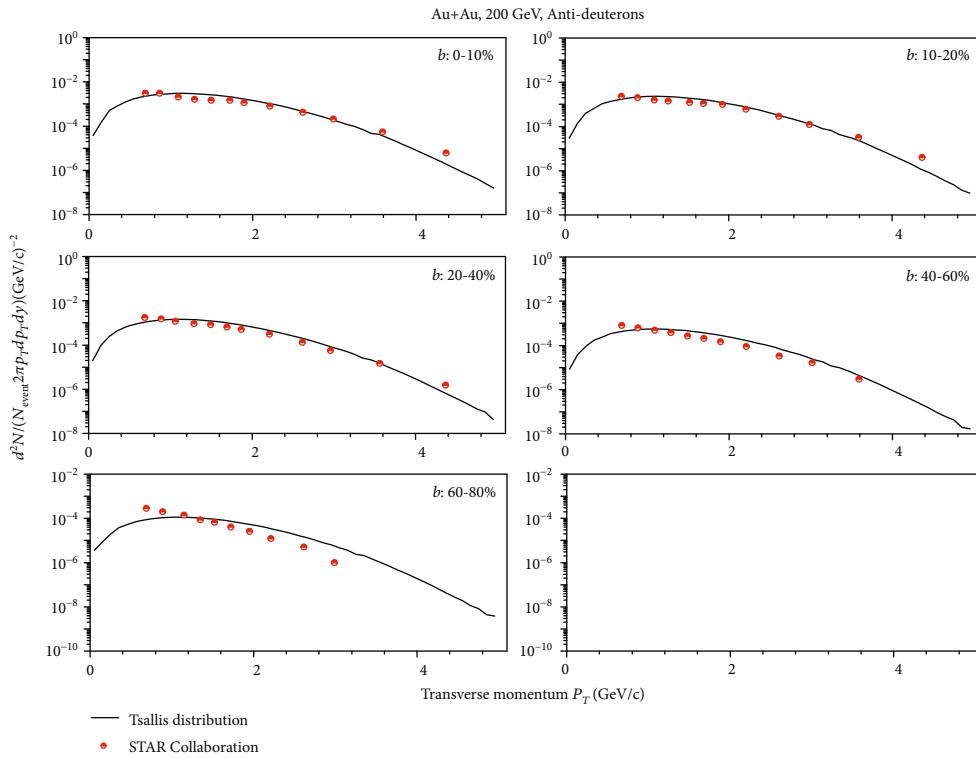


FIGURE 6: Antideuteron transverse momentum spectra in Au + Au collisions at  $\sqrt{s_{NN}} = 200$  GeV for 0-10%, 10-20%, 20-40%, 40-60%, and 60-80% centralities. Calculations are shown by the solid lines. Experimental data taken from the STAR Collaboration [20] are represented by the symbols.

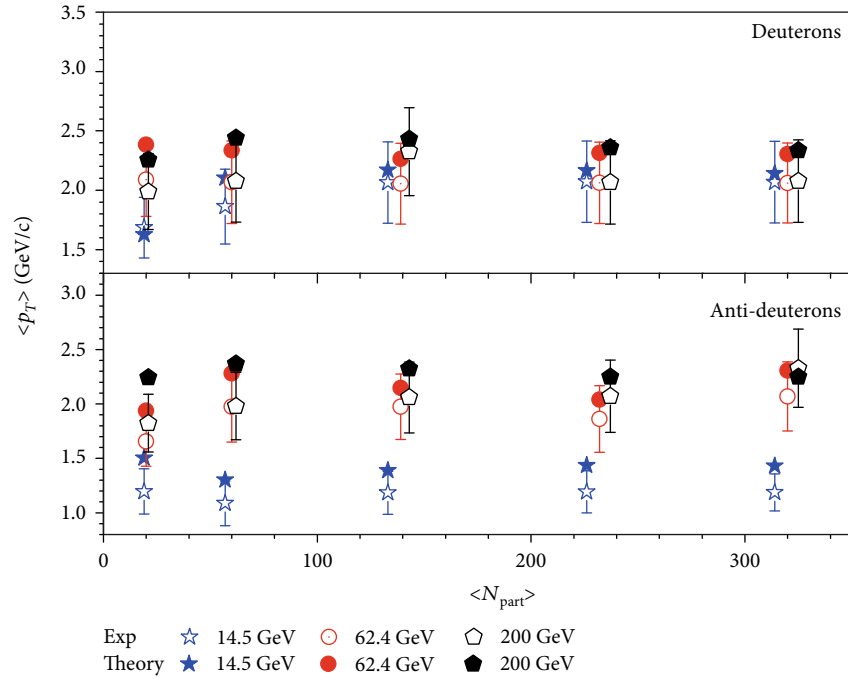


FIGURE 7: Deuterons and antideuterons average transverse momenta ( $\langle p_T \rangle$ ) as a function of ( $\langle N_{part} \rangle$ ) at midrapidity ( $|y| < 0.3$ ) for  $\sqrt{s_{NN}} = 14.5, 62.4,$  and  $200$  GeV. Calculations are shown by the solid symbols. Experimental data taken from the Figures 1–6 are represented by the hollow symbols.

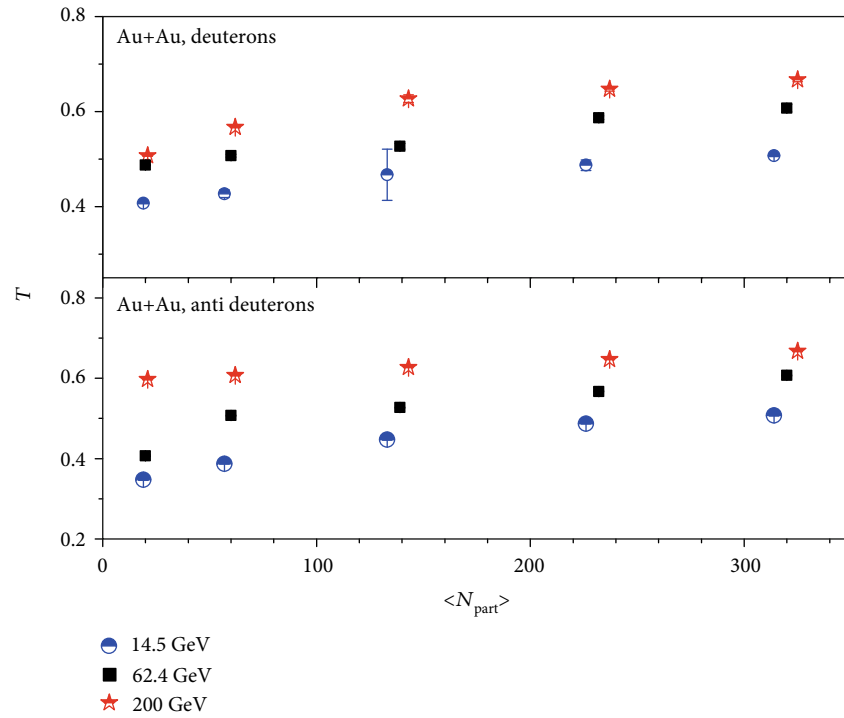


FIGURE 8: Dependence of  $T$  on the average number of participants for deuterons and antideuterons in events with different centrality intervals. The symbols represent the parameter values listed in Tables 2–4.

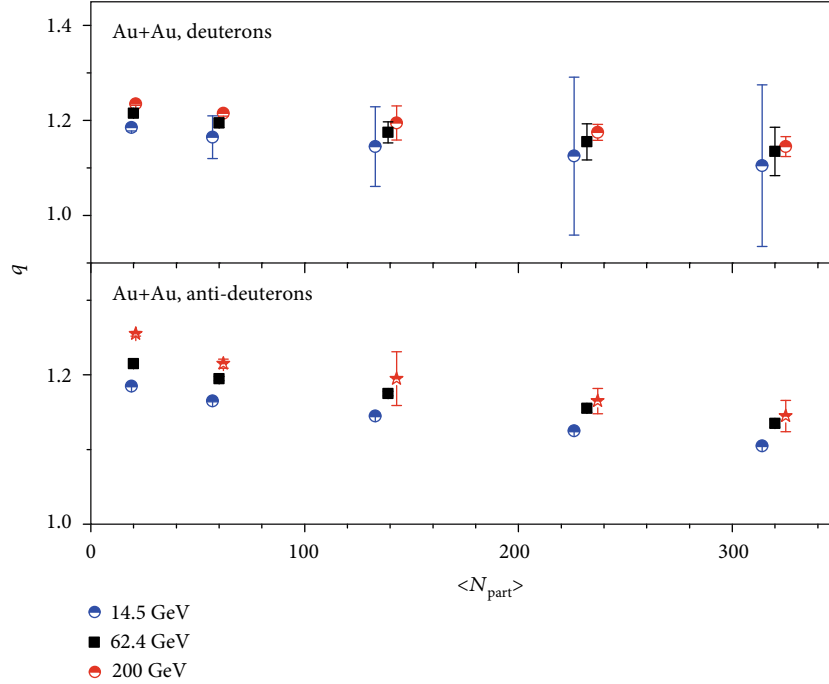


FIGURE 9: Dependence of  $q$  on the average number of participants for deuterons and antideuterons in events with different centrality intervals. The symbols represent the parameter values listed in Tables 2–4.

from the effective temperature; the correlation between Kinetic freeze-out temperature and centrality will be focused in the future work.

#### 4. Summary and Outlook

In summary, we have presented the transverse momentum distributions of (anti-)deuterons in Au + Au collisions at  $\sqrt{s_{NN}} = 14.5, 62.4,$  and  $200$  GeV for 0-10%, 10-20%, 20-40%, 40-60%, and 60-80% centralities. The Tsallis distribution in the multisource thermal model has been used in all calculations. Based on this model, we have investigated transverse momentum distributions of (anti-)deuterons and the law about effective temperature and entropy with the centrality of collision. In conclusion, it can give the agreement between calculation results and the experimental data. The effective temperature extracted from  $d$  and  $\bar{d}$  increases with decrease of centrality percentage at the same incident energy, and the entropy index decreases with decrease of centrality percentage at the same incident energy. And at the same collision centrality, they increase with increase of incident energy. But the Kinetic freeze-out temperature and the evolution of time during the collision have yet to be studied in depth.

#### Data Availability

The data used to support the findings of this study are included within the article and are cited at relevant places within the text as references.

#### Conflicts of Interest

The author declares that there is no conflict of interests regarding the publication of this paper.

#### Acknowledgments

This work was supported by the Introduction of Doctoral Starting Funds of Scientific Research of Guangxi University of Chinese Medicine under Grant No. 2018BS024, the Natural Science Foundation of Guangxi Zhuangzu Autonomous Region of China under Grant no. 2012GXNSFBA053011, the Research support project of Guangxi institutions of higher learning (No. 200103YB071), and the Open Project of Guangxi Key Laboratory of Nuclear Physics and Nuclear Technology (No. NLK2020-03).

#### References

- [1] C. Alt, T. Anticic, B. Baatar et al., “Energy dependence of  $\Lambda$  and  $\Xi$  production in central Pb+Pb collisions at 20A, 30A, 40A, 80A, and 158A GeV measured at the CERN Super Proton Synchrotron,” *Physical Review C*, vol. 78, no. 3, article 034918, 2008.
- [2] J. X. Sun, F. H. Liu, and E. Q. Wang, “Pseudorapidity distributions of charged particles and contributions of leading nucleons in Cu-Cu collisions at high energies,” *Chinese Physics Letters*, vol. 27, no. 3, article 032503, 2010.
- [3] E. Q. Wang, F. H. Liu, M. A. Rahim, S. Fakhraddin, and J. X. Sun, “Singly and doubly charged projectile fragments in nucleus-emulsion collisions at Dubna energy in the framework of the multi-source model,” *Chinese Physics Letters*, vol. 28, no. 8, article 082501, 2011.

- [4] B. C. Li and M. Huang, "Strongly coupled matter near phase transition," *Journal of Physics G: Nuclear and Particle Physics*, vol. 36, no. 6, article 064062, 2009.
- [5] F. H. Liu, "Anisotropic emission of charged mesons and structure characteristic of emission source in heavy ion collisions at 1–2A GeV," *Chinese Physics B*, vol. 17, no. 8, pp. 883–895, 2008.
- [6] R. Arsenescu, C. Baglin, H. P. Beck et al., "An investigation of the antinuclei and nuclei production mechanism in Pb + Pb collisions at 158 A GeV," *New Journal of Physics*, vol. 5, p. 150, 2003.
- [7] Q. F. Li, Y. J. Wang, X. B. Wang, and C. W. Shen, "Helium-3 production from Pb+Pb collisions at SPS energies with the UrQMD model and the traditional coalescence afterburner," *Science China: Physics, Mechanics and Astronomy*, vol. 59, no. 3, article 632002, 2016.
- [8] H.-L. Lao, H.-R. Wei, F.-H. Liu, and R. A. Lacey, "An evidence of mass-dependent differential kinetic freeze-out scenario observed in Pb-Pb collisions at 2.76 TeV," *The European Physical Journal A*, vol. 52, no. 7, p. 203, 2016.
- [9] S. Mrówczyński and P. Słoń, "Hadron-deuteron correlations and production of light nuclei in relativistic heavy-ion collisions," *Acta Physica Polonica B*, vol. 51, no. 8, article 1739, 2020.
- [10] S. Mrówczyński, "Production of light nuclei in the thermal and coalescence models," *Acta Physica Polonica B*, vol. 48, no. 4, pp. 707–716, 2017.
- [11] S. Bazak and S. Mrówczyński, "<sup>4</sup>He versus <sup>4</sup>Li and production of light nuclei in relativistic heavy-ion collisions," *Modern Physics Letters A*, vol. 33, no. 25, article 1850142, 2018.
- [12] P. Liu, J. H. Chen, Y. G. Ma, and S. Zhang, "Production of light nuclei and hypernuclei at High Intensity Accelerator Facility energy region," *Nuclear Science and Techniques*, vol. 28, no. 4, p. 55, 2017.
- [13] F. X. Liu, G. Chen, Z. L. Zhe, D. M. Zhou, and Y. L. Xie, "Light (anti) nuclei production in Cu+Cu collisions at  $\sqrt{s_{NN}}=200$  GeV," *The European Physical Journal A*, vol. 55, p. 160, 2019.
- [14] B. C. Li, Y. Y. Fu, L. L. Wang, and F. H. Liu, "Dependence of elliptic flows on transverse momentum and number of participants in Au+Au collisions at  $\sqrt{s_{NN}} = 200$  GeV," *Journal of Physics G: Nuclear and Particle Physics*, vol. 40, no. 2, article 025104, 2013.
- [15] Y. H. Chen, F. H. Liu, and E. K. Sarkisyan-Grinbaum, "Event patterns from negative pion spectra in proton-proton and nucleus-nucleus collisions at SPS," *Chinese Physics C*, vol. 42, no. 10, article 104102, 2018.
- [16] M. Waqas, F. H. Liu, L. L. Li, and H. M. Alfanda, "Analysis of effective temperature and kinetic freeze-out volume in high energy nucleus-nucleus and proton-proton collisions," 2020, <http://arxiv.org/abs/hep-ph/2001.06796v1>.
- [17] C. Tsallis, "Possible generalization of Boltzmann-Gibbs statistics," *Journal of Statistical Physics*, vol. 52, no. 1-2, pp. 479–487, 1988.
- [18] T. S. Biró, G. Purcsel, and K. Ürmösy, "Non-extensive approach to quark matter," *The European Physical Journal A*, vol. 40, no. 3, p. 325, 2009.
- [19] J. Cleymans and D. Worku, "Relativistic thermodynamics: transverse momentum distributions in high-energy physics," *The European Physical Journal A*, vol. 48, no. 11, p. 160, 2012.
- [20] STAR Collaboration, "Beam energy dependence of (anti-)deuteron production in Au+Au collisions at RHIC," *Physical Review C*, vol. 99, no. 6, article 064905, 2019.
- [21] F. H. Liu, Y. Q. Gao, and H. R. Wei, "On descriptions of particle transverse momentum spectra in high energy collisions," *Advances in High Energy Physics*, vol. 2014, Article ID 293873, 12 pages, 2014.
- [22] F. H. Liu, Y. Q. Gao, T. Tian, and B. C. Li, "Unified description of transverse momentum spectrums contributed by soft and hard processes in high-energy nuclear collisions," *European Physical Journal A*, vol. 50, no. 6, p. 94, 2014.
- [23] F. H. Liu and J. S. Li, "Isotopic production cross section of fragments in <sup>56</sup>Fe + p and <sup>136</sup>Xe (<sup>124</sup>Xe)+Pb reactions over an energy range from 300 A to 1500 A MeV," *Physical Review C*, vol. 78, no. 4, article 044602, 2008.
- [24] F. Büyükkiliç and D. Demirhan, "A fractal approach to entropy and distribution functions," *Physics Letters A*, vol. 181, no. 1, pp. 24–28, 1993.
- [25] J. Chen, Z. Zhang, G. Su, L. Chen, and Y. Shu, "q-generalized Bose-Einstein condensation based on Tsallis entropy," *Physics Letters A*, vol. 300, no. 1, pp. 65–70, 2002.
- [26] J. M. Conroy and H. G. Miller, "Color superconductivity and Tsallis statistics," *Physical Review D*, vol. 78, no. 5, article 054010, 2008.
- [27] F. Pennini, A. Plastino, and A. R. Plastino, "Tsallis entropy and quantal distribution functions," *Physics Letters A*, vol. 208, no. 4-6, pp. 309–314, 1995.
- [28] A. M. Teweldeberhan, A. R. Plastino, and H. G. Miller, "On the cut-off prescriptions associated with power-law generalized thermostatics," *Physics Letters A*, vol. 343, no. 1-3, pp. 71–78, 2005.
- [29] J. M. Conroy, H. G. Miller, and A. R. Plastino, "Thermodynamic consistency of the  $_q$ -deformed Fermi-Dirac distribution in nonextensive thermostatics," *Physics Letters A*, vol. 374, no. 45, pp. 4581–4584, 2010.
- [30] H. Zheng and L. Zhu, "Comparing the Tsallis distribution with and without thermodynamical description in collisions," *Advances in High Energy Physics*, vol. 2016, Article ID 9632126, 10 pages, 2016.
- [31] H. Zheng and L. Zhu, "Can Tsallis distribution fit all the particle spectra produced at RHIC and LHC?," *Advances in High Energy Physics*, vol. 2015, Article ID 180491, 9 pages, 2015.
- [32] A. Andronic, P. Braun-Munzinger, and J. Stachel, "The horn, the hadron mass spectrum and the QCD phase diagram - the statistical model of hadron production in central nucleus-nucleus collisions," *Nuclear Physics A*, vol. 834, no. 1-4, pp. 237c–240c, 2010.
- [33] STAR Collaboration, "Bulk properties of the medium produced in relativistic heavy-ion collisions from the Beam Energy Scan Program," *Physical Review C*, vol. 96, no. 4, article 044904, 2017.

## Research Article

# Event Shape and Multiplicity Dependence of Freeze-Out Scenario and System Thermodynamics in Proton+Proton Collisions at $\sqrt{s} = 13$ TeV Using PYTHIA8

Sushanta Tripathy <sup>1</sup>, Ashish Bisht <sup>1</sup>, Raghunath Sahoo <sup>1</sup>, Arvind Khuntia <sup>2</sup>,  
and Malavika Panikkassery Salvan <sup>3</sup>

<sup>1</sup>Department of Physics, Indian Institute of Technology Indore, Simrol, Indore 453552, India

<sup>2</sup>Institute of Nuclear Physics, Polish Academy of Science (PAS), IFJ PAN, Krakow, Poland

<sup>3</sup>National Institute of Technology Tiruchirappalli, Tiruchirappalli, Tamil Nadu, India

Correspondence should be addressed to Raghunath Sahoo; [raghunath.sahoo@cern.ch](mailto:raghunath.sahoo@cern.ch)

Received 24 September 2020; Revised 28 December 2020; Accepted 18 January 2021; Published 23 February 2021

Academic Editor: Mariana Frank

Copyright © 2021 Sushanta Tripathy et al. This is an open access article distributed under the Creative Commons Attribution License, which permits unrestricted use, distribution, and reproduction in any medium, provided the original work is properly cited. The publication of this article was funded by SCOAP<sup>3</sup>.

Recent observations of QGP-like conditions in high-multiplicity pp collisions from ALICE experiment at the LHC warrant an introspection whether to use pp collisions as a baseline measurement to characterize heavy-ion collisions for the possible formation of a Quark-Gluon Plasma. A double differential study of the particle spectra and thermodynamics of the produced system as a function of charged-particle multiplicity and transverse sphericity in pp collisions would shed light on the underlying event dynamics. Transverse sphericity, one of the event shape observables, allows to separate the events in terms of jetty and isotropic events. We analyse the identified particle transverse momentum ( $p_T$ ) spectra as a function of charged-particle multiplicity and transverse sphericity using Tsallis nonextensive statistics and Boltzmann-Gibbs Blast-Wave (BGBW) model in pp collisions at  $\sqrt{s} = 13$  TeV using PYTHIA8 event generator. The extracted parameters such as temperature ( $T$ ), radial flow ( $\beta$ ), and nonextensive parameter ( $q$ ) are shown as a function of charged-particle multiplicity for different sphericity classes. We observe that the isotropic events approach thermal equilibrium while the jetty ones remain far from equilibrium. We argue that, while studying the QGP-like conditions in small systems, one should separate the isotropic events from the sphericity-integrated events, as the production dynamics are different.

## 1. Introduction

Although it was envisaged long back that central heavy-ion collisions at ultrarelativistic energies could produce a deconfined state of partons called Quark-Gluon Plasma (QGP) [1, 2], the unprecedented collision energies available at the Large Hadron Collider (LHC) at CERN, Switzerland, has brought up new challenges in characterizing the proton+proton (pp) collisions to understand a possible formation of QGP droplets in these hadronic collisions. There are various signatures of QGP, which are already observed in pp collisions at the LHC. These include strangeness enhancement [3], hardening of  $p_T$ -spectra [4, 5], and the

thermal effective temperature being comparable to that observed in heavy-ion collisions [3], degree of collectivity [6], etc. In view of these observations in pp collisions, it has become more challenging to understand the system formed in pp collisions, although pp has been considered as a baseline measurement to understand nuclear effects like  $R_{AA}$  and suppression of  $J/\psi$ . The new measurements at the LHC keeping in mind that the final state multiplicity drives the particle production (excellent scaling observed) necessitate a closer look into the underlying physics mechanisms of particle production in pp collisions. The phenomena like color reconnection, multipartonic interactions, rope hadronization, and string fragmentation have done a wonderful job

TABLE 1: V0 multiplicity classes and the corresponding charged particle multiplicities.

V0M class	I	II	III	IV	V	VI	VII	VIII	IX	X
$N_{ch}$	50-140	42-49	36-41	31-35	27-30	23-26	19-22	15-18	10-14	0-9

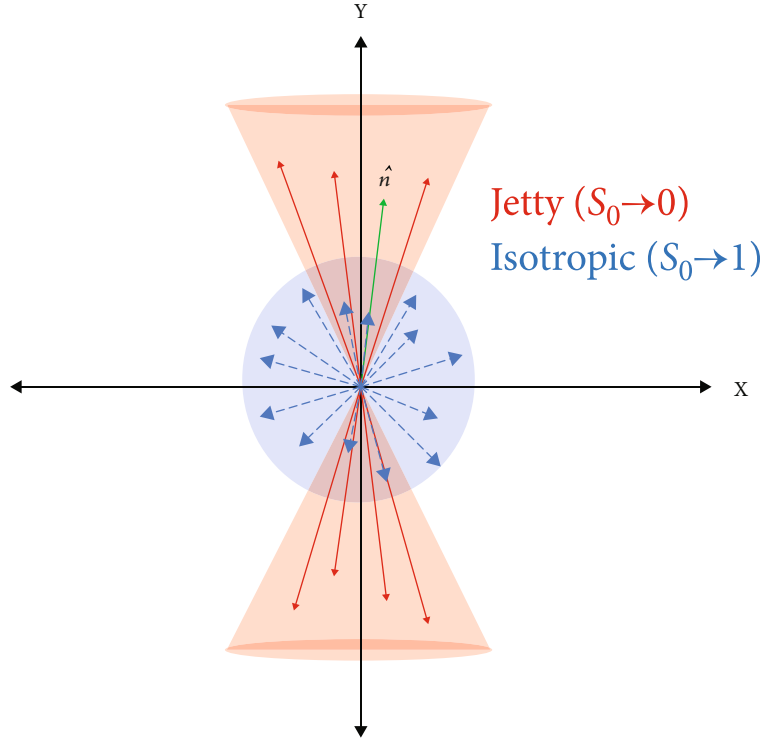


FIGURE 1: (Color online) Figure showing jetty and isotropic events in the transverse plane.

in explaining various new heavy-ion-like observations in pp collisions.

Event shape engineering has given a new direction to underlying events in pp collisions to have a differential study taking various observables. The transverse sphericity successfully separates jetty events from isotropic ones in pp collisions. As is clearly understandable, the particle production mechanism in jetty events is different from isotropic ones. When the former one involves high- $p_T$  phenomena, the latter is soft-physics dominated. In view of this, recently, we have carried out a double differential study of particle ratios in pp collisions at the LHC energies, taking transverse sphericity, transverse momentum, and multiplicity [7]. A natural question which pops up is whether the thermodynamics of jetty events are different from the isotropic ones. To quantify this, in the present study, we have taken pQCD-inspired PYTHIA8 event generator which includes multiparton interactions (MPI) along with color reconnection (CR), to study the event shape and multiplicity dependence of freeze-out scenario and system thermodynamics in pp collisions at  $\sqrt{s} = 13$  TeV. It has been reported that the MPI scenario is crucial to explain the underlying events, multiplicity distributions, and flow-like patterns in terms

of color reconnection [8]. Thus, it is a preferable tune to study the possible thermodynamics in small systems, as experimental data are not available yet. It should be worth noting that PYTHIA8 does not have inbuilt thermalization. However, as reported in Ref. [8], the color reconnection (CR) mechanism along with the multiparton interactions (MPI) in PYTHIA8 produces the properties which arise from the thermalization of a system such as radial flow and mass dependent rise of mean transverse momentum. In the PYTHIA model, a single string connecting two partons follows the movement of the partonic endpoints, and this movement gives a common boost to the string fragments (final state hadrons). With CR along with MPI, two partons from independent hard scatterings can reconnect and they increase the transverse boost. This microscopic treatment of final state particle production is quite successful in explaining the similar features which arise from a macroscopic picture via hydrodynamical description of high-energy collisions. Thus, it is apparent to say that the PYTHIA8 model with MPI and CR has a plausible ability to produce the features of thermalization. The current results, which use PYTHIA8 with MPI and CR to obtain event shape and multiplicity dependence of freeze-out scenario and

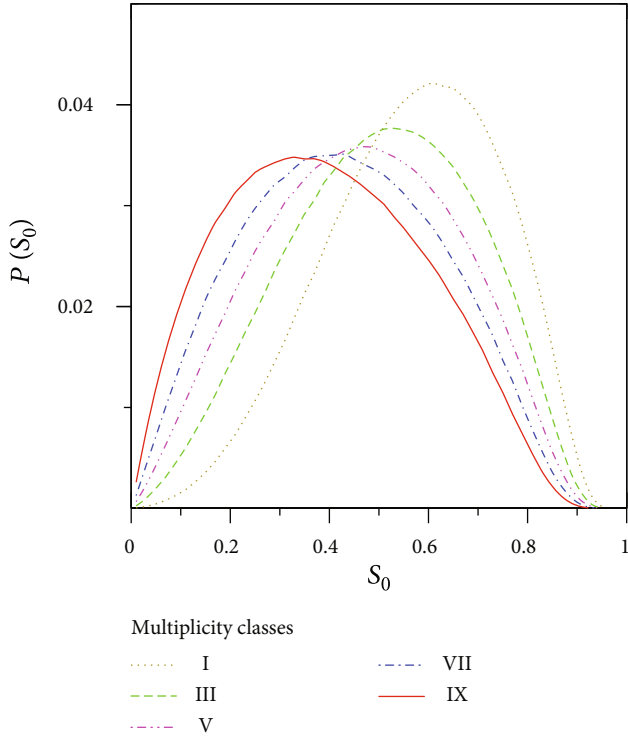


FIGURE 2: (Color online) Sphericity distribution for different multiplicity classes in pp collisions at  $\sqrt{s} = 13$  TeV using PYTHIA8. Different colors and line styles are for different multiplicity classes.

system thermodynamics, will help to compare with the upcoming experimental data. Such a study has also been done for heavy flavor particles like  $J/\psi$  in Ref. [9]. This paper is intended solely for presenting a noble and unique study, which would give an outlook on similarities/differences between jetty and isotropic events in LHC pp events and their multiplicity dependence. This will help in making a proper bridge in understanding the particle production from hadronic to heavy-ion collisions.

Furthermore, the spacetime evolution of hadronic and heavy-ion collisions at the LHC energies could be thought of following a cosmological expansion of the produced fireball. In this scenario, as the fireball expands and cools down, it leaves a temperature profile with time. Different identified particles decouple from the fireball giving the signature of a mass-dependent particle freeze-out—higher mass particles decoupling from the system earlier in time. In this work, we have considered such a scenario and have performed a differential study taking final state event multiplicity and event topology.

The paper is organized as follows. After the introduction and identification of the problem under consideration, we discuss the methodology of event generation and data analysis in Section 2. In Section 3, we discuss the identified  $p_T$ -spectra in pp collisions to extract the thermodynamic parameters. Finally, we summarize the work in Section 4 with important findings, which could be tested when experimental data become available.

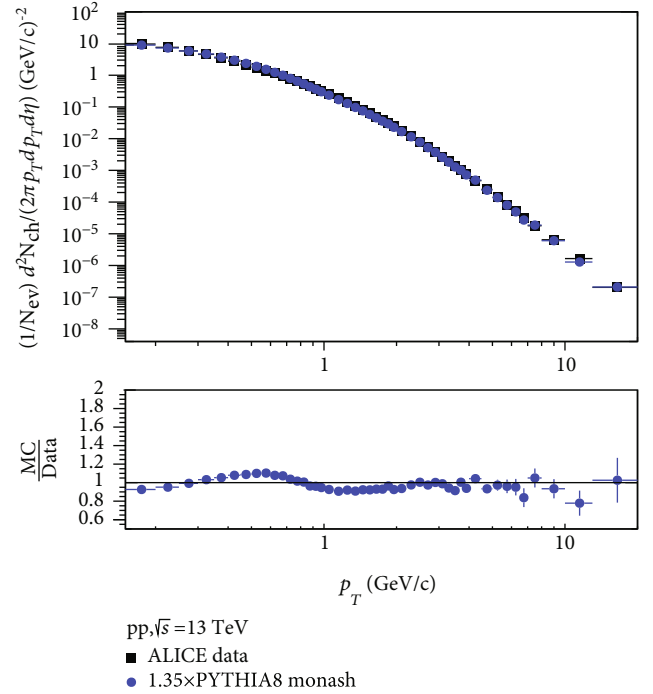


FIGURE 3: (Color online) Upper panel: comparison of charged particle  $p_T$  spectra in pp collisions at  $\sqrt{s} = 13$  TeV between ALICE data [19] and PYTHIA8 simulation, which is used for this analysis. Lower panel: the ratio between scaled simulated data and experimental data.

## 2. Event Generation and Analysis Methodology

PYTHIA, one of the popular and most useful event generators in the LHC era, is used to simulate ultrarelativistic collision events among the elementary particles like  $e^\pm$ ,  $p$ , and  $\bar{p}$ . It is incorporated with many known physics mechanisms like hard and soft interactions, parton distributions, initial- and final-state parton showers, multipartonic interactions, string fragmentation, color reconnection, and resonance decays [10].

In our present study, we have used PYTHIA 8.235 to generate pp collisions at  $\sqrt{s} = 13$  TeV with Monash 2013 Tune (Tune:14) [11]. PYTHIA 8.235 is an advanced version of PYTHIA 6 which includes the multipartonic interaction (MPI) scenario as one of the key improvements. The detailed physics processes in PYTHIA 8.235 can be found in Ref. [12]. We have implemented the inelastic, nondiffractive component of the total cross-section for all soft QCD processes with the switch SoftQCD: all = on. This analysis is carried out with around 250 million minimum bias events at  $\sqrt{s} = 13$  TeV, and we have chosen MPI-based scheme of default color reconnection mode (ColorReconnection:mode(0)). Here, the minimum bias events are those events where no selection on charged-particle multiplicity and/or sphericity is applied. For the generated events, we let all the resonances to decay except the ones used in our study with the switch HadronLevel:Decay = on. Throughout the analysis, the event selection criteria are such that only those events were chosen

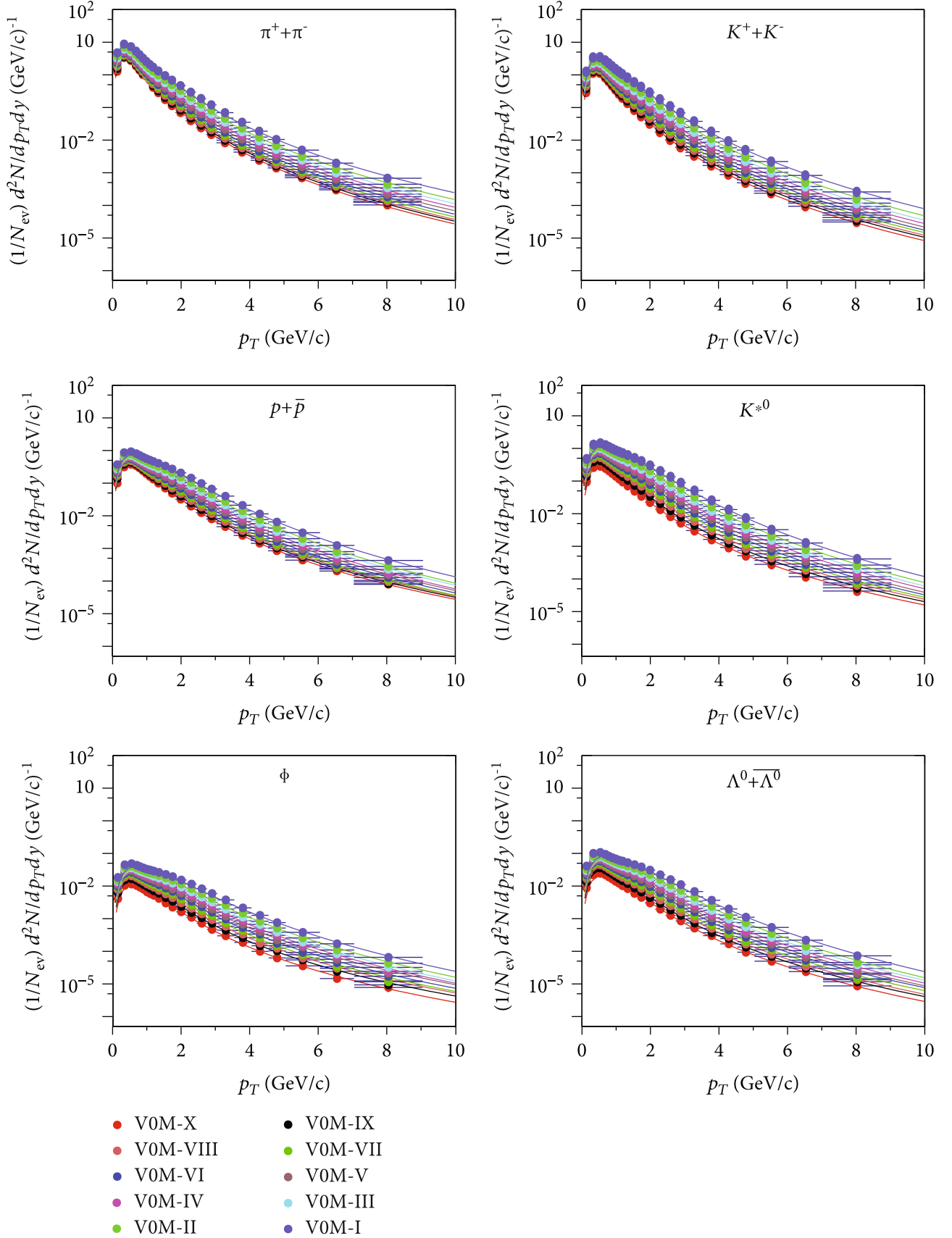


FIGURE 4: (Color online) Fitting of generated  $p_T$ -spectra of identified hadrons from PYTHIA8 using Tsallis distribution for sphericity integrated events in various multiplicity classes as shown in Table 1.

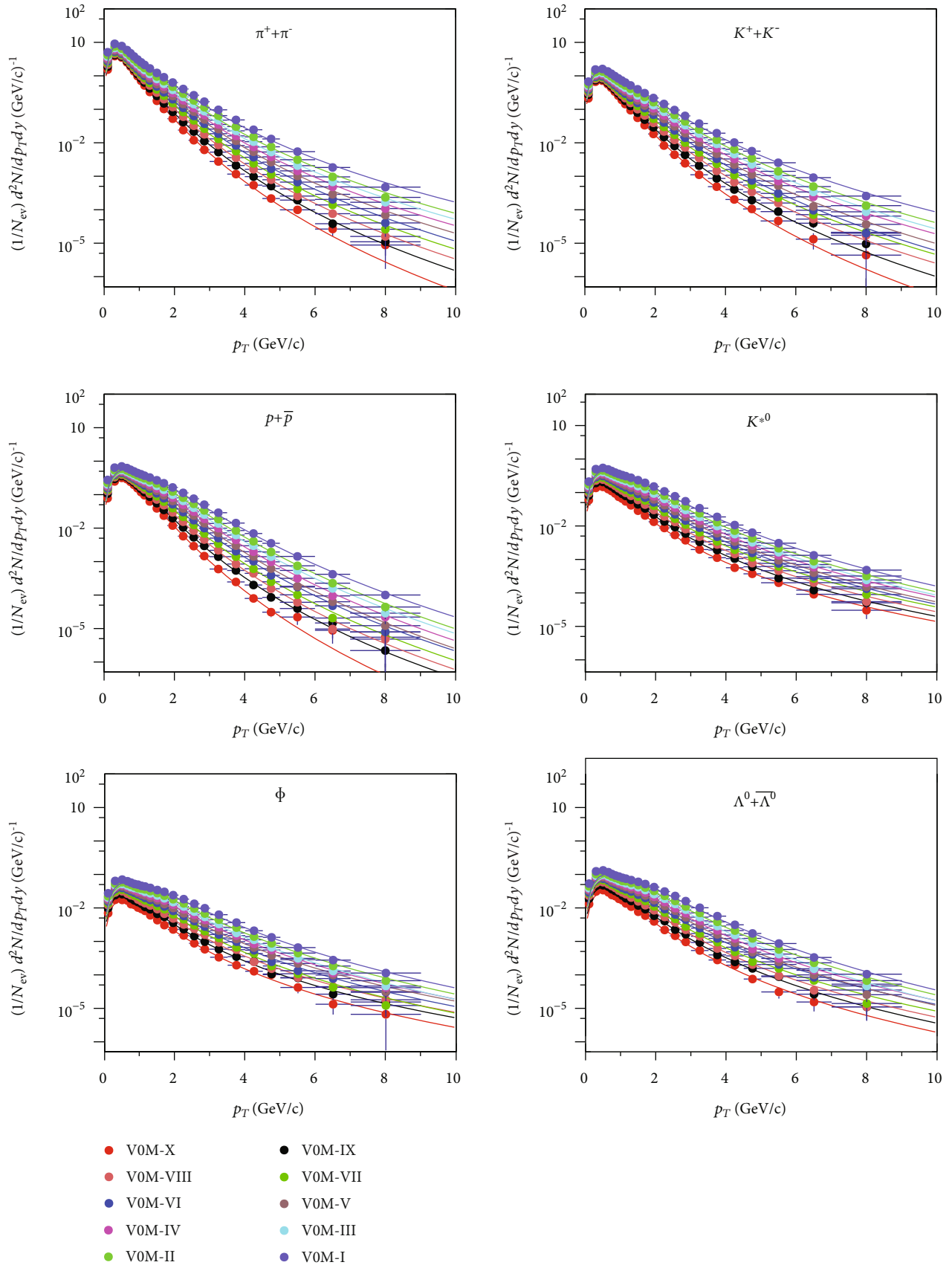


FIGURE 5: (Color online) Fitting of generated  $p_T$ -spectra of identified hadrons from PYTHIA8 using Tsallis distribution for isotropic events in various multiplicity classes as shown in Table 1.

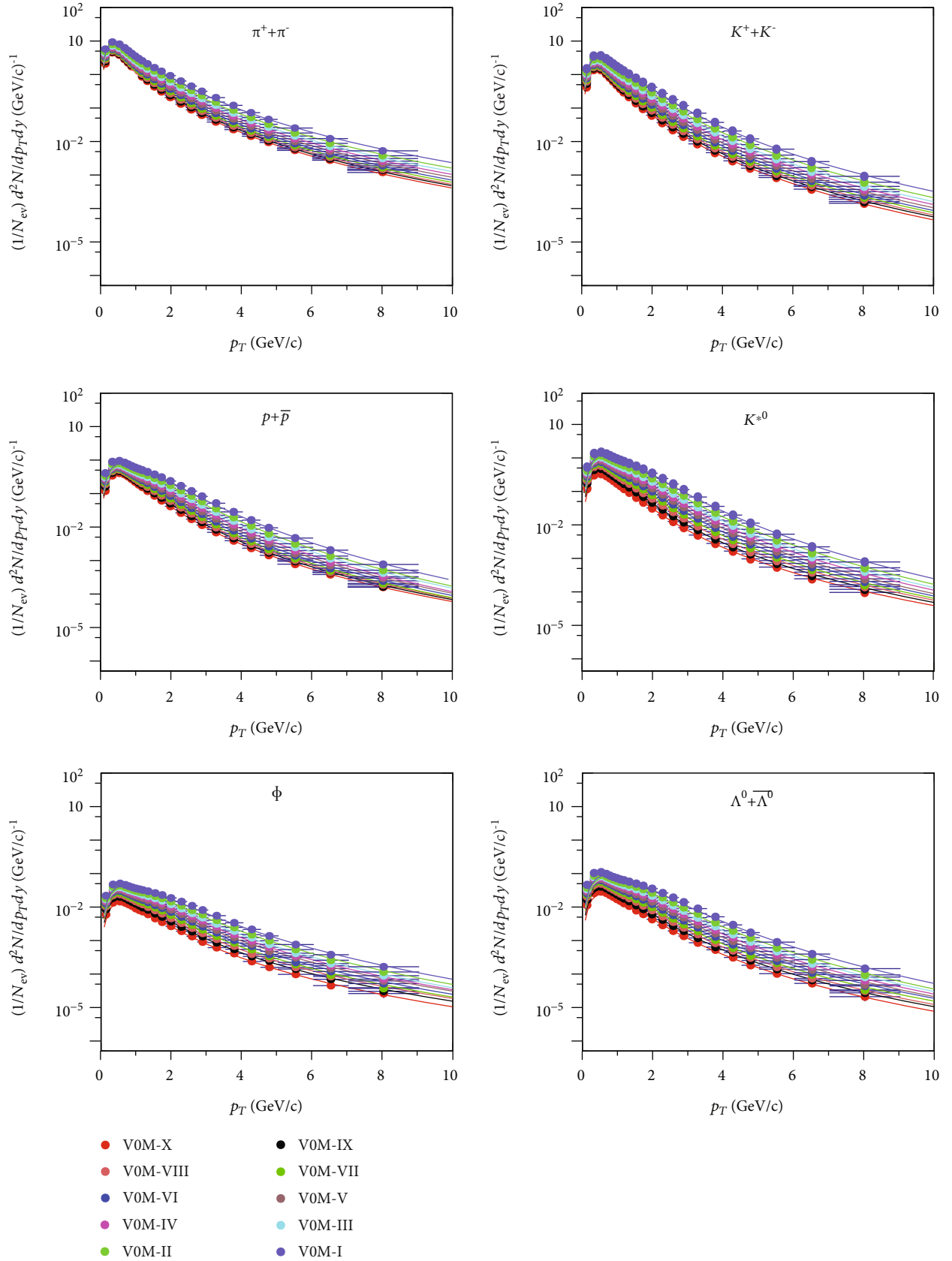


FIGURE 6: (Color online) Fitting of generated  $p_T$ -spectra of identified hadrons from PYTHIA8 using Tsallis distribution for jetty events in various multiplicity classes as shown in Table 1.

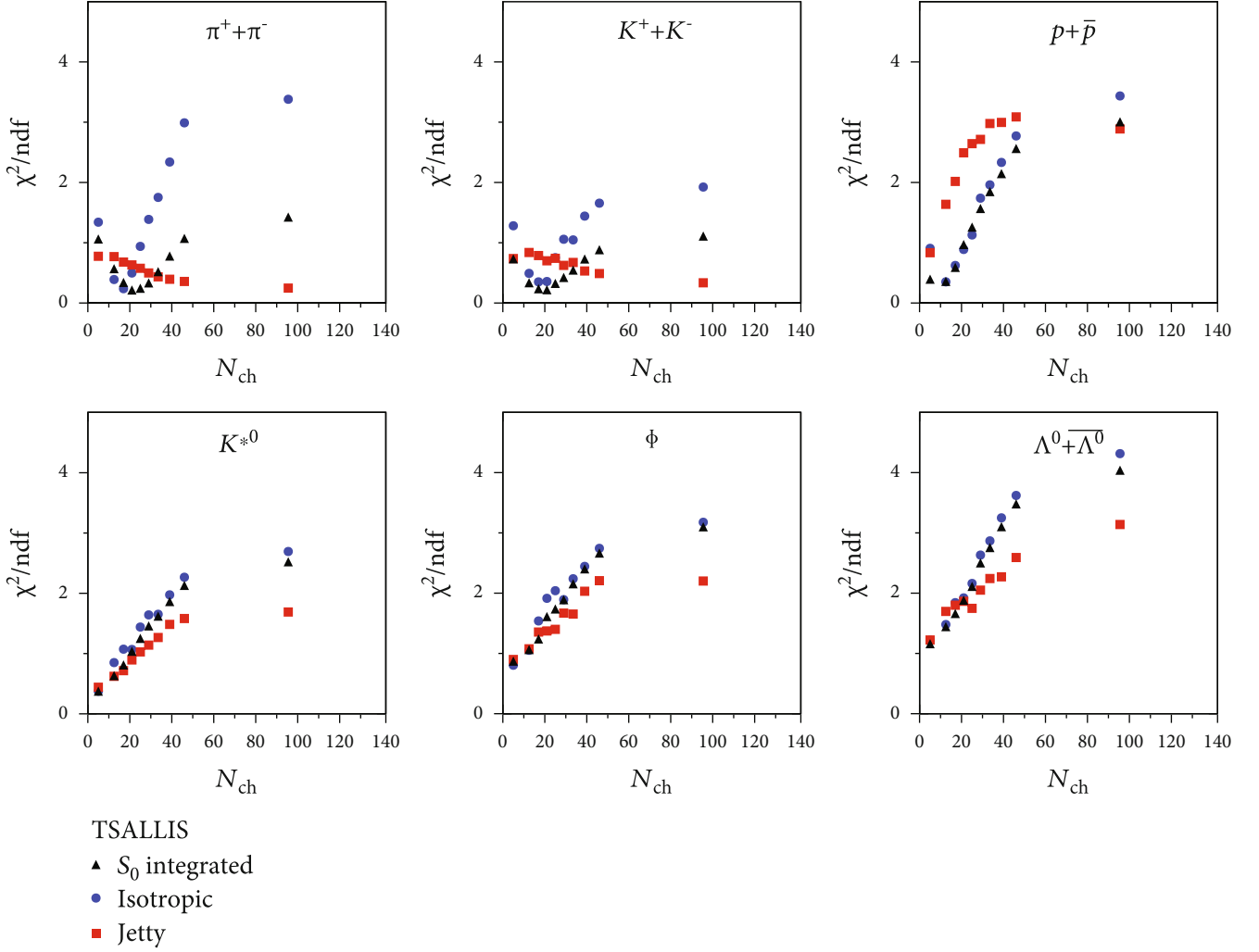


FIGURE 7: (Color online)  $\chi^2/\text{NDF}$  for the fitting of generated  $p_T$ -spectra of identified hadrons using Tsallis distribution in different sphericity and multiplicity classes.

which have at least 5 charged particles. To match with experimental conditions, charged particle multiplicities ( $N_{\text{ch}}$ ) have been chosen in the acceptance of V0 detector in ALICE at the LHC with pseudorapidity coverage of V0A ( $2.8 < \eta < 5.1$ ) and V0C ( $-3.7 < \eta < -1.7$ ) [13]. The generated events are categorized in ten V0 multiplicity (V0M) bins, each with 10% of the total number of events. The number of charged particle multiplicities in an event in different V0 multiplicity classes is listed in Table 1.

For an event, transverse sphericity is defined for a unit vector  $\hat{n}(n_T, 0)$  which minimizes the ratio [14–16]:

$$S_0 = \frac{\pi^2}{4} \left( \frac{\sum_i |\vec{p}_{T_i} \times \hat{n}|}{\sum_i p_{T_i}} \right)^2. \quad (1)$$

By restricting it to the transverse plane, transverse sphericity becomes infrared and collinear safe [17], and by

construction, the extreme limits of transverse sphericity are related to specific configurations of events in the transverse plane. The value of transverse sphericity ranges from 0 to 1. Transverse sphericity becoming 0 means that the events are pencil-like (back-to-back structure) while 1 would mean the events are isotropic as shown in Figure 1. The pencil-like events are usually the hard events, while the isotropic events are the result of soft processes. Here onwards, for the sake of simplicity, the transverse sphericity is referred to as sphericity. To disentangle the jetty and isotropic events from the average-shaped events, we have applied sphericity cuts on our generated events. In this analysis, the sphericity distributions are selected in the pseudorapidity range of  $|\eta| < 0.8$  with a minimum constraint of 5 charged particles with  $p_T > 0.15$  GeV/c. The jetty events are those having  $0 \leq S_0 < 0.29$  with lowest 20 percent ( $\approx 50$  M events), and the isotropic events are those having  $0.64 < S_0 \leq 1$  with highest 20 percent ( $\approx 50$  M events) of the total events [18].

To assure the quality of the generated events, we show in Figure 2, the correlation between the sphericity with

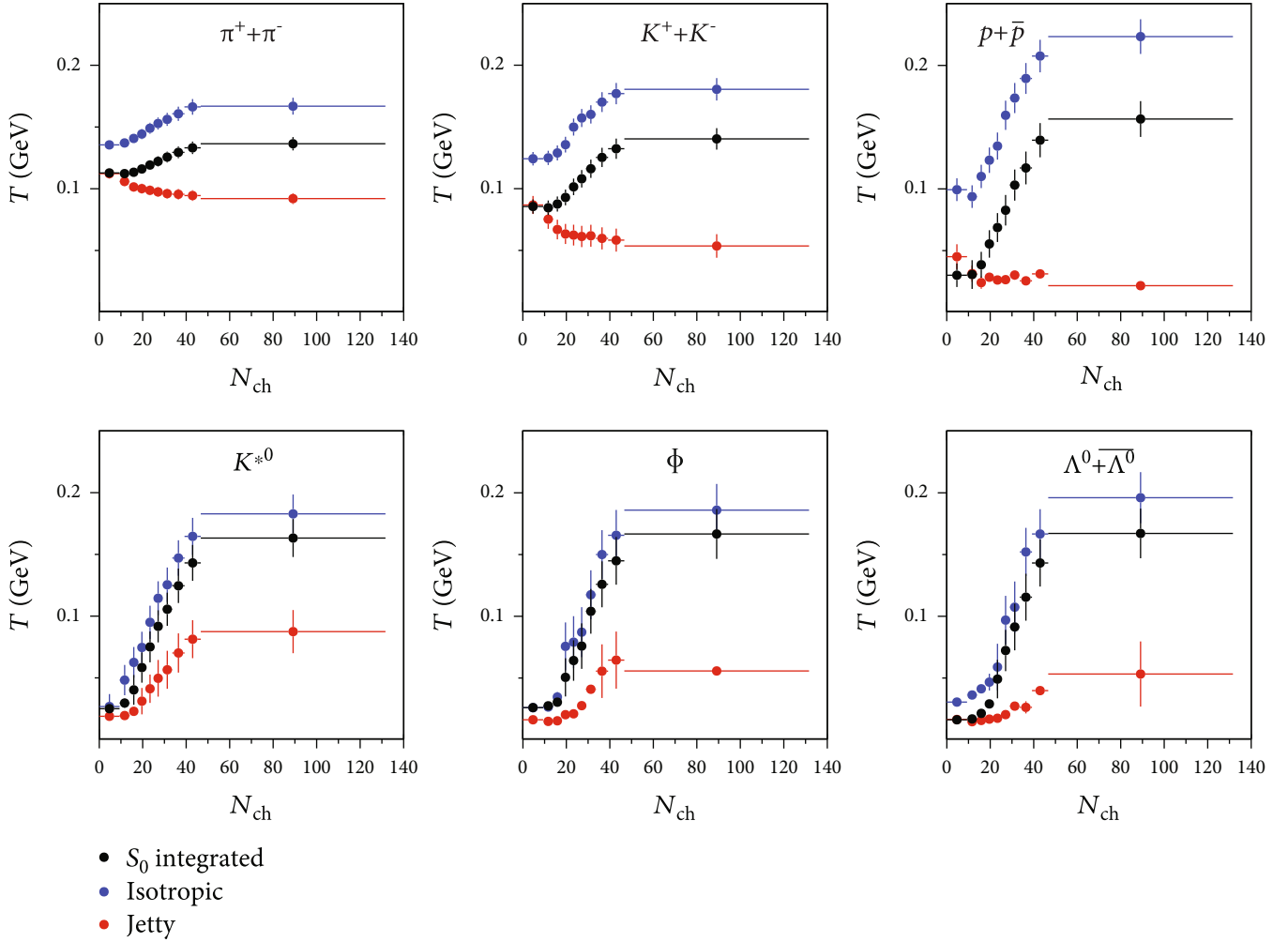


FIGURE 8: (Color online) Multiplicity dependence of  $T$  in different sphericity classes from the fitting of Tsallis distribution using Eq. (4).

charged-particle multiplicity. As expected, the high multiplicity pp collisions are dominated by isotropic events, while the low multiplicity events are dominated by the jetty ones. From our earlier event shape analysis [7], it is evident that sphericity along with the charged particle multiplicity (which is correlated with nMPI) should be preferred for a better selectivity of events.

### 3. Transverse Momentum Spectra of Identified Particles

To check the compatibility of PYTHIA8 simulated data with the experimental data, we have compared the charged particle  $p_T$  spectra for pp collisions at  $\sqrt{s} = 13$  TeV from ALICE data [19]. The comparison is shown in Figure 3. The lower panel shows the ratio of the predictions from PYTHIA8 to experimental data. In order to see the agreement of spectral shapes, we have used an arbitrary scaling factor (1.35) to scale the simulated data. The used scaling factor is to check the matching of the spectral shape, and it bears no physical significance. We found that the scaled simulated data agree

with the spectral shape from experimental data within (10-20)% at low- $p_T$  and consistent to unity for intermediate and high- $p_T$ .

For the first time, we combine sphericity with event multiplicity and study the freeze-out scenario and thermodynamics of the system formed in pp collisions at  $\sqrt{s} = 13$  TeV. We use experimentally motivated thermodynamically consistent Tsallis nonextensive distribution function [20] for analysing the complete range of the  $p_T$ -spectra, whereas to extract the kinetic freeze-out temperature and the possible collective radial flow we use the Boltzmann-Gibbs Blast-Wave model [21, 22] taking  $p_T \leq 2$  GeV/c. We begin with the fitting and analysis procedure with a short description on Tsallis nonextensive statistics and Boltzmann-Gibbs Blast-Wave model. Here onwards,  $(\pi^+ + \pi^-)$ ,  $(K^+ + K^-)$ ,  $(p + \bar{p})$ ,  $(K^{*0} + \bar{K}^{*0})$ , and  $(\Lambda^0 + \bar{\Lambda}^0)$  are denoted as pion ( $\pi$ ), kaon ( $K$ ), proton ( $p$ ),  $K^{*0}$ , and  $\Lambda$ , respectively.

*3.1. Experimentally Motivated Tsallis Nonextensive Statistics.* The  $p_T$ -spectra of produced particles in high-energy

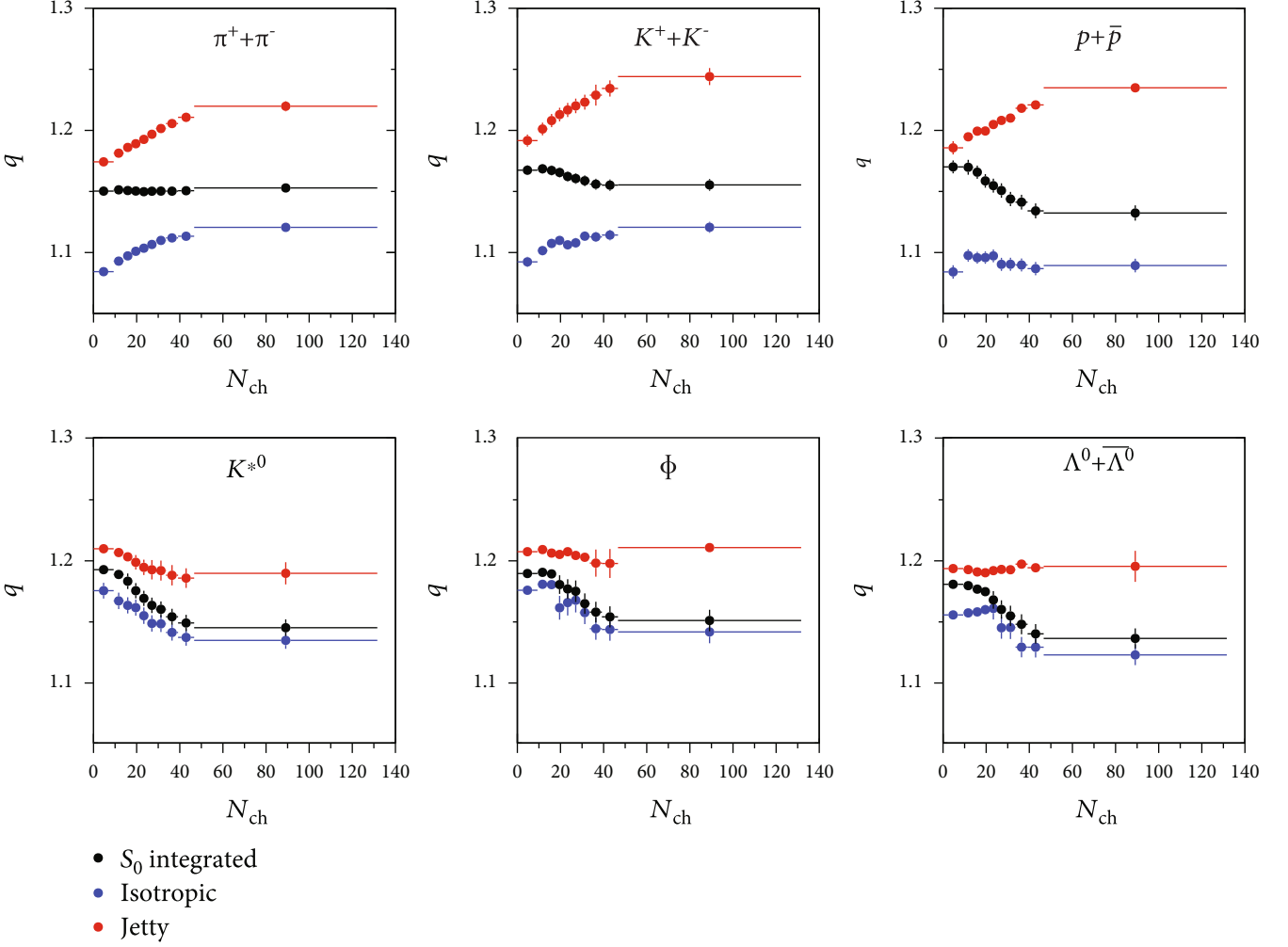


FIGURE 9: (Color online) Multiplicity dependence of  $q$  in different spherocity classes from the fitting of Tsallis distribution using Eq. (4).

collisions have been proposed to follow a thermalised Boltzmann type of distribution given as [23],

$$E \frac{d^3\sigma}{d^3p} \simeq C \exp\left(-\frac{p_T}{T_{kin}}\right). \quad (2)$$

Here,  $C$  is the normalisation constant, and  $T_{kin}$  is the kinetic freeze-out temperature. Due to possible QCD contributions at high- $p_T$ , the identified particle spectra at RHIC and LHC do not follow the above distribution, while the low- $p_T$ -region can be explained by incorporating the radial flow ( $\beta$ ) into the Boltzmann-Gibbs distribution function, which is known as Boltzmann-Gibbs Blast-Wave (BGBW) model [22]. One can extract  $T_{kin}$  and radial flow ( $\beta$ ) by fitting the identified particle transverse momentum spectra at low- $p_T$ . The detailed description along with the fitting of the Boltzmann-Gibbs Blast-Wave model to the identified particle spectra is discussed in the next subsection.

To describe the complete  $p_T$ -spectra, one has to account for the power-law contribution at high- $p_T$  [24–26], which

empirically takes care of the possible QCD contributions. A combination of both low and high- $p_T$  aspects has been proposed by Hagedorn, which describes the experimental data over a wide  $p_T$ -range [27]. The distribution proposed by Hagedorn is given by

$$E \frac{d^3\sigma}{d^3p} = C \left(1 + \frac{p_T}{p_0}\right)^{-n} \rightarrow \begin{cases} \exp\left(-\frac{np_T}{p_0}\right) & \text{for } p_T \rightarrow 0, \\ \left(\frac{p_0}{p_T}\right)^n & \text{for } p_T \rightarrow \infty. \end{cases} \quad (3)$$

Here,  $C$ ,  $p_0$ , and  $n$  are fitting parameters. The above expression acts as an exponential and a power-law function for low and high- $p_T$ , respectively. However, deviations are observed by experiments at RHIC [28, 29] and LHC [30–33] while describing the  $p_T$ -spectra of identified particles using a Boltzmann-Gibbs distribution function, even if the domain of temperature of the produced systems are high enough. On

the other hand, Tsallis statistics with its nonextensivity features can be regarded as a generalization of Boltzmann-Gibbs statistics, and it gives a better description of systems, which have not yet reached equilibration. Its low- $p_T$  exponential and high- $p_T$  power-law behavior gives a complete spectral description of identified secondaries produced in pp collisions. In addition, a nonextensive entropic  $q$ -parameter shows the extent of nonequilibrium of any particle in a thermal bath. There are few different versions of Tsallis distribution, which are being used by experimentalists and theoreticians. However, we use a thermodynamically consistent Tsallis nonextensive distribution function as shown in Ref. [20]. By saying thermodynamically consistent, we mean that the used distribution function satisfies all the standard thermodynamic relations for entropy, temperature, energy, pressure, and number density. The Tsallis distribution function at midrapidity is given by,

$$\frac{1}{p_T} \left. \frac{d^2 N}{dp_T dy} \right|_{y=0} = \frac{gV m_T}{(2\pi)^2} \left[ 1 + (q-1) \frac{m_T}{T} \right]^{-q/(q-1)}, \quad (4)$$

where  $g$  is the degeneracy factor,  $V$  is the system volume,  $m_T = \sqrt{p_T^2 + m^2}$  is the transverse mass, and  $q$  is the nonextensive parameter. In the limit of  $q \rightarrow 1$ , Tsallis distribution (Eq. (4)) reduces to the standard Boltzmann-Gibbs distribution (Eq. (2)). It should be noted here that the use of the Tsallis nonextensive distribution function is purely motivated by its excellent description of experimental particle spectra in high-energy collisions [34–38] starting from elementary  $e^+ + e^-$  and hadronic to heavy-ion collisions [28, 29, 39–52]. Recently, few comprehensive studies have been carried out using Tsallis distribution for pions and quarkonium spectra in pp collisions [53, 54]. In this subsection, we employ the Tsallis nonextensive distribution function as shown in Eq. (4) to describe the  $p_T$ -spectra. It should be noted here that the used Tsallis distribution function of Eq. (4) [55] has an extra power  $q$ , compared to the original distribution function proposed by Tsallis [56]. However, this form of the distribution function is thermodynamically consistent, which makes no major change in the observables as the values of  $q$  in hadronic collisions lie between,  $1 \leq q \leq 1.22$  [57]. While Tsallis nonextensive statistics makes a connection between entropy and thermodynamics of a system, the dynamics of the system in terms of long-range correlations and fluctuations ( $(q-1)$  being the strength of the fluctuation [58]) are encoded in the entropic parameter,  $q$ .

Figures 4–6 show the fitting of  $p_T$ -spectra of pions, kaons, protons,  $K^{*0}$ ,  $\phi$ , and  $\Lambda$  as a function of charged-particle multiplicity using Tsallis distribution function (Eq. (4)) for spherocity-integrated, isotropic, and jetty events, respectively. We observe that the Tsallis distribution fits the generated data till  $p_T \approx 10$  GeV/c. Figure 7 shows the quality of fitting in terms of the reduced- $\chi^2$ ,  $\chi^2/\text{NDF}$  as a function of multiplicity for different sphero-

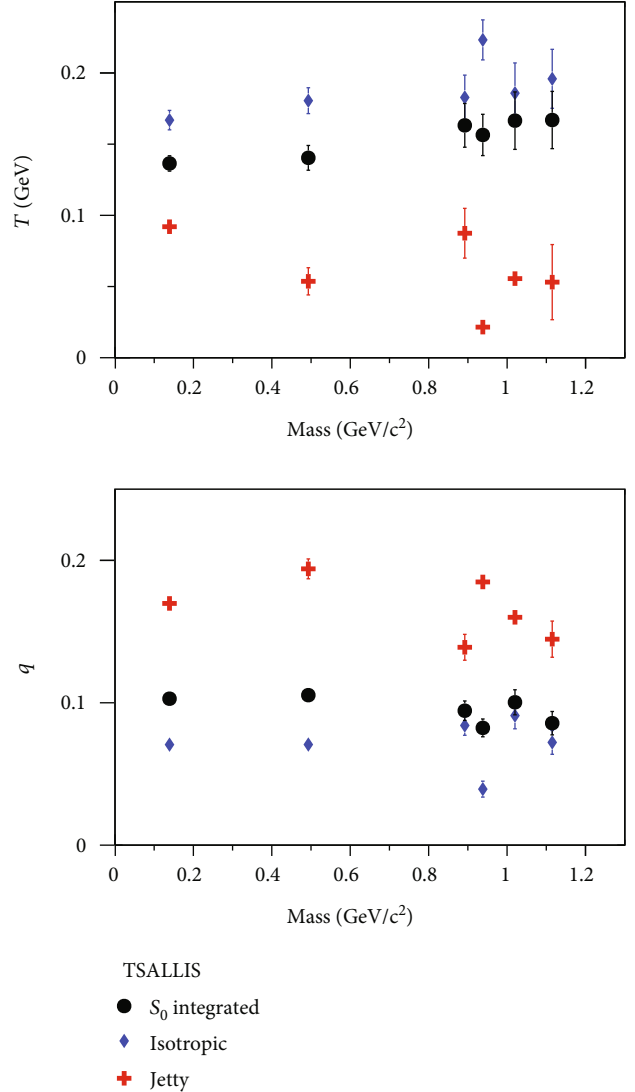


FIGURE 10: (Color online) Mass dependence of  $T$  and  $q$  in different spherocity classes for the highest multiplicity class.

city classes. The values of  $\chi^2/\text{NDF}$  show that the quality of fitting is reasonably good for all the multiplicity and spherocity classes.

Figures 8 and 9 show the extracted parameters from the fitting of Tsallis distribution using Eq. (4) as a function of charged-particle multiplicity for different spherocity classes. Figure 8 shows that the temperature parameter increases with charged-particle multiplicity for spherocity-integrated and isotropic events. However, the jetty events seem to show a reverse trend for pions, kaons, and protons. For  $K^{*0}$ ,  $\phi$ , and  $\Lambda$ , the temperature parameter shows an increase with multiplicity for jetty events. For all cases, the temperature for jetty events is lower compared to the other spherocity classes. We also observe that the temperature for lighter particles does not change significantly with multiplicity, while with the increase in mass, the temperature increases steeply as a function of multiplicity. Figure 9 shows that

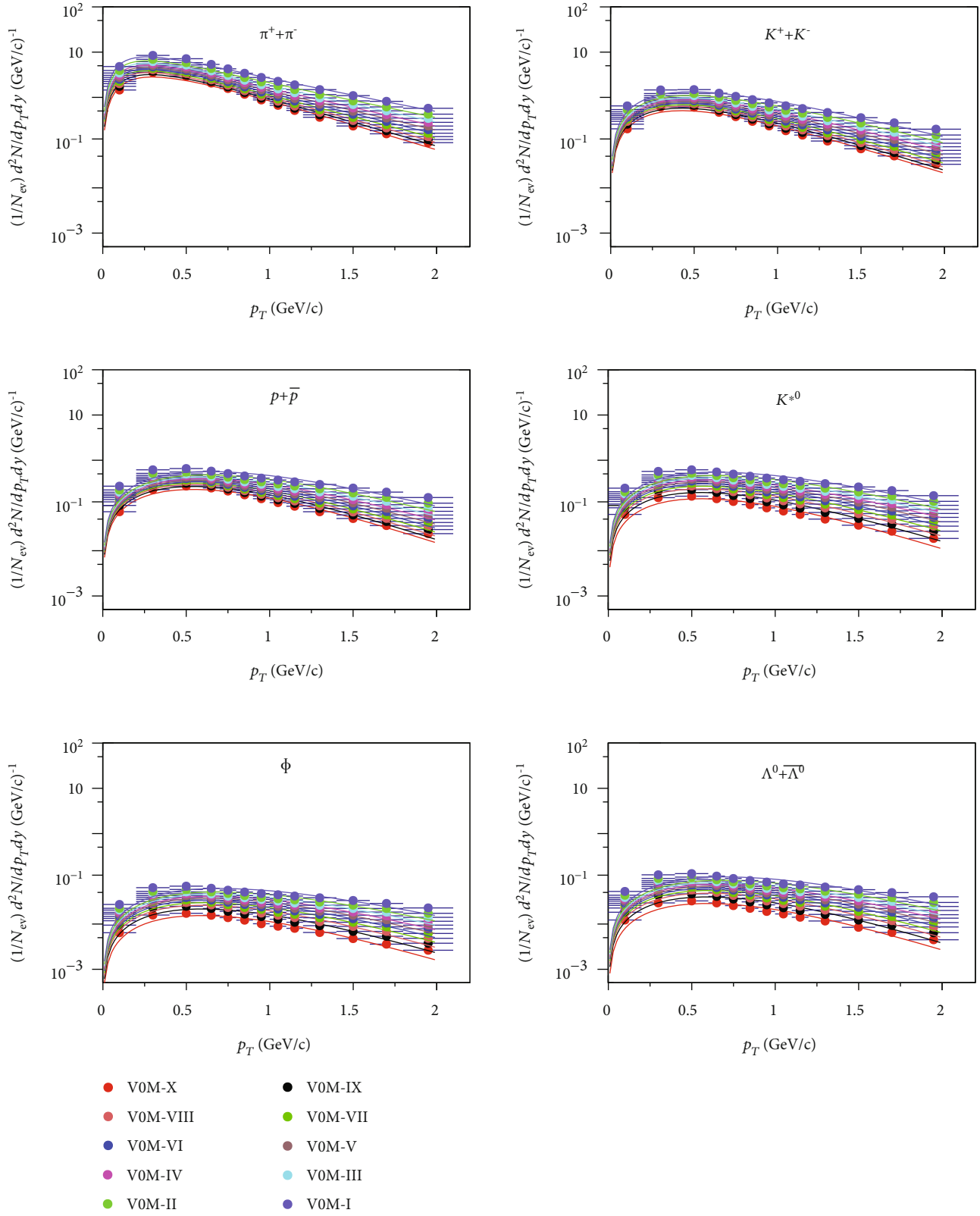


FIGURE 11: (Color online) Fitting of generated  $p_T$ -spectra of identified hadrons from PYTHIA8 using BGBW model for sphericity integrated events in various multiplicity classes as shown in Table 1.

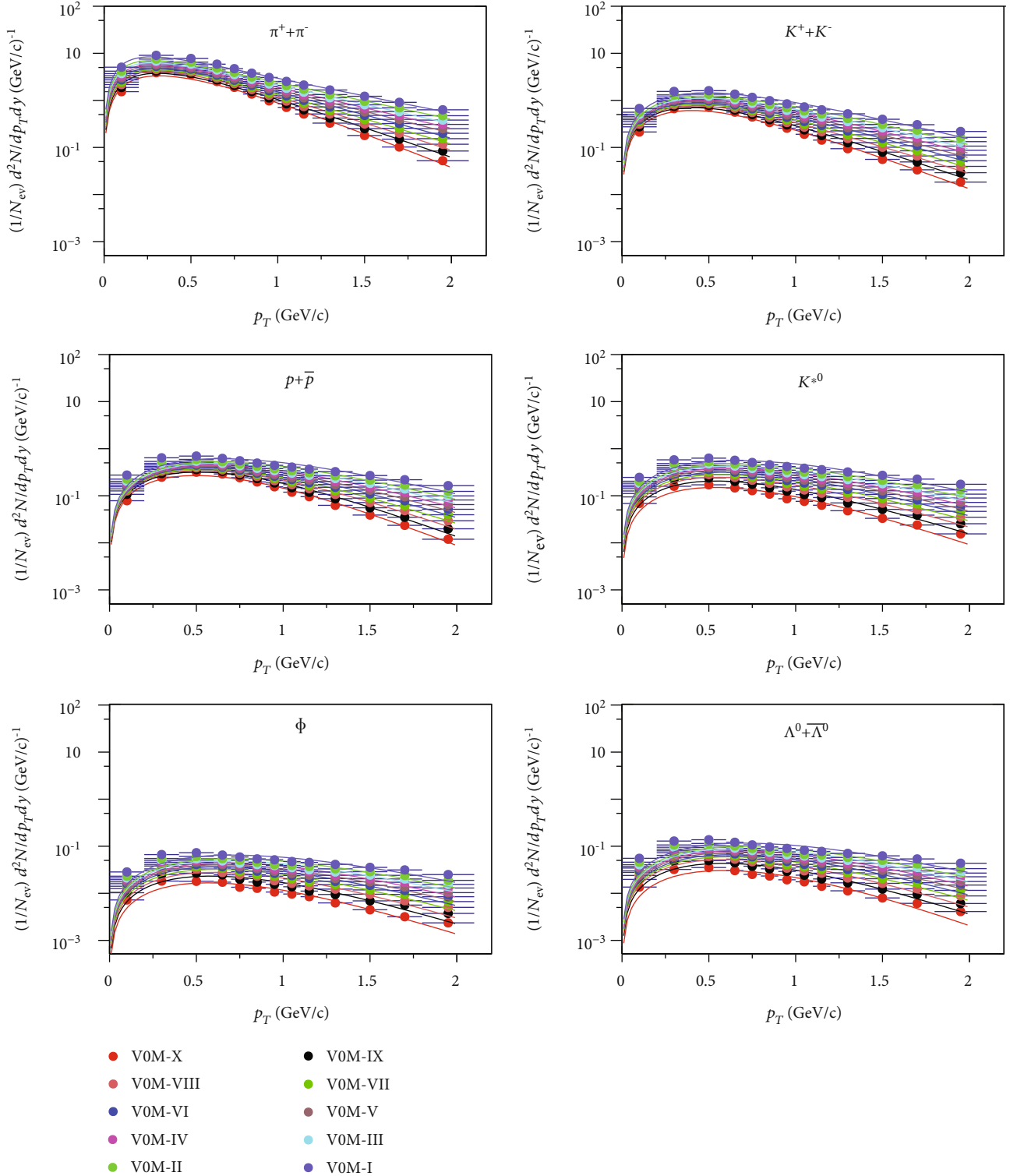


FIGURE 12: (Color online) Fitting of generated  $p_T$ -spectra of identified hadrons from PYTHIA8 using the BGBW model for isotropic events in various multiplicity classes as shown in Table 1.

for isotropic events, the nonextensive parameter,  $q$  values remain lower compared to the spherocity-integrated events, which suggests that isotropic events have got a higher

degree of equilibration compared to spherocity-integrated events. This indicates that while studying the QGP-like conditions in small systems, one should separate the isotropic

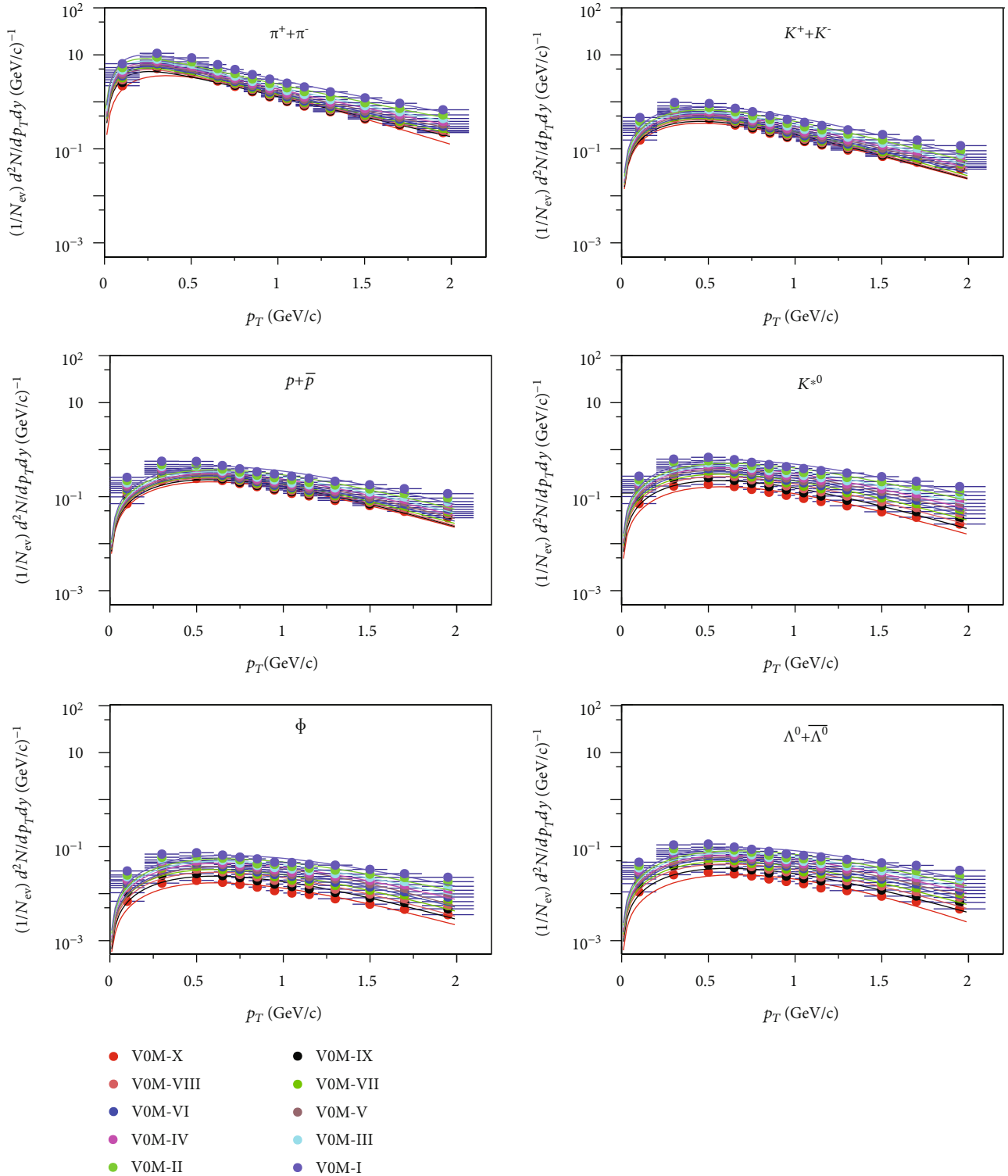


FIGURE 13: (Color online) Fitting of generated  $p_T$ -spectra of identified hadrons from PYTHIA8 using the BGBW model for jetty events in various multiplicity classes as shown in Table 1.

events from the sphericity-integrated events, as the production dynamics are different. On the contrary, the  $q$ -values for jetty are always higher compared to sphericity-

integrated events, indicating that the jetty events remain far away from equilibrium. The present study is very useful in understanding the microscopic features of degrees of

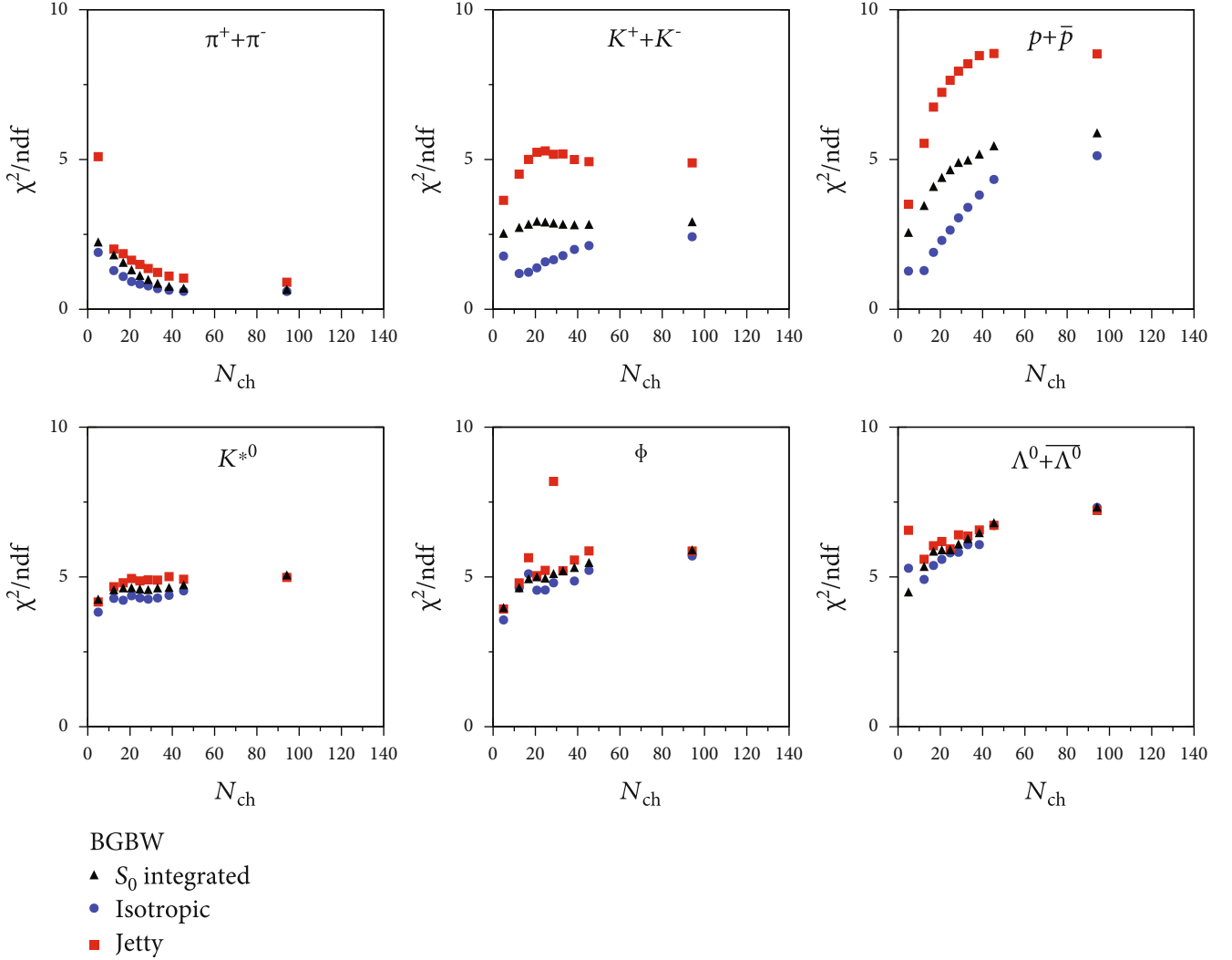


FIGURE 14: (Color online)  $\chi^2/\text{NDF}$  for the fitting of generated  $p_T$ -spectra of identified hadrons using the BGBW model in different spherocity and multiplicity classes.

equilibration and their dependencies on the number of particles in the system and on the geometrical shape of an event. It would be interesting to study the particle mass dependence of these thermodynamic parameters. In order to do that, we have taken the events with the highest multiplicity class and done the same spherocity analysis, taking different particles as discussed here, which is shown in Figure 10. For the isotropic and spherocity-integrated events in high multiplicity pp collisions, the temperature remains higher for particles with higher masses, which supports a differential freeze-out scenario. This suggests that massive particles freeze-out early from the system. However, the jetty events show a reverse trend.

To explore the flow-like features in small systems, one needs to focus on the low- $p_T$  of the particle spectra with Boltzmann-Gibbs Blast-Wave (BGBW) model, which is discussed in the next subsection. As we saw an indication of a differential freeze-out scenario, in the following section,

we consider making individual spectral analysis using BGBW, instead of a simultaneous fitting, which is usually necessitated by a single freeze-out scenario.

**3.2. Boltzmann-Gibbs Blast-Wave Model.** The expression for invariant yield in Boltzmann-Gibbs Blast-Wave (BGBW) model is given by [21, 22]

$$E \frac{d^3 N}{dp^3} = D \int d^3 \sigma_\mu p^\mu \exp \left( -\frac{p^\mu u_\mu}{T} \right). \quad (5)$$

Here, the four-velocity denoting flow velocities in space-time is given by  $u^\mu = \cosh \rho (\cosh \eta, \tanh \rho \cos \phi_r, \tanh \rho \sin \phi_r, \sinh \eta)$ , and the particle four-momentum is  $p^\mu = (m_T \cosh y, p_T \cos \phi, p_T \sin \phi, m_T \sinh y)$ , while the kinetic freeze-out surface is given by  $d^3 \sigma_\mu = (\cosh \eta, 0, 0, -$

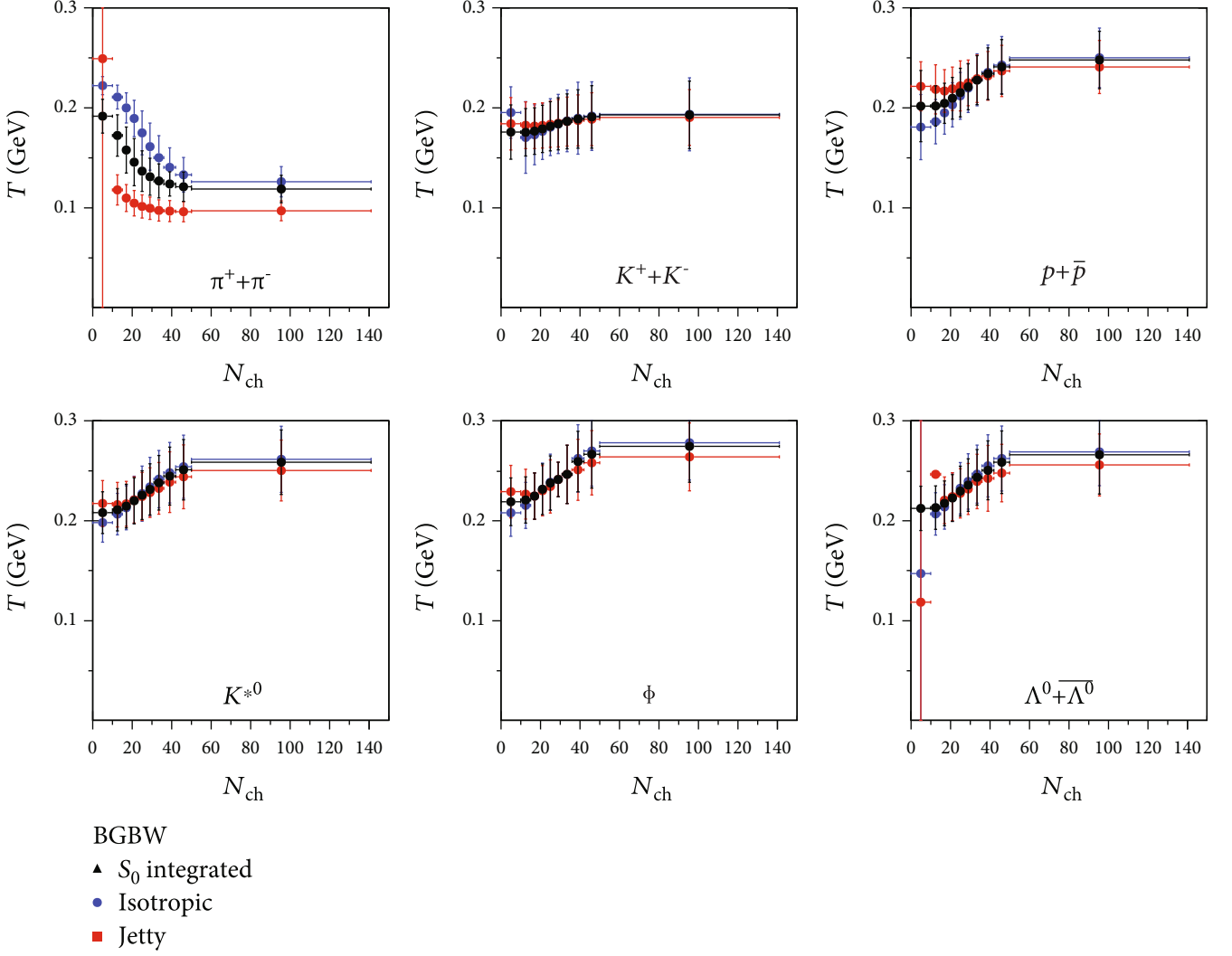


FIGURE 15: (Color online) Multiplicity dependence of  $T$  in different sphericity classes from the fitting of the BGBW model.

$\sinh \eta) \tau r dr d\eta d\phi$ . Here,  $\eta$  is the space-time rapidity and assuming Bjorken correlation in rapidity, i.e.,  $y = \eta$  [59], Eq. (5) can be expressed as

$$\left. \frac{d^2 N}{dp_T dy} \right|_{y=0} = D \int_0^{R_0} r dr K_1 \left( \frac{m_T \cosh \rho}{T} \right) I_0 \left( \frac{p_T \sinh \rho}{T} \right). \quad (6)$$

Here,  $D = gVm_T/2\pi^2$ , where  $g$  is the degeneracy factor,  $V$  is the system volume, and  $m_T = \sqrt{p_T^2 + m^2}$  is the transverse mass. Here,  $I_0(p_T \sinh \rho/T)$  and  $K_1(m_T \cosh \rho/T)$  are the modified Bessel's functions. They are given by

$$K_1 \left( \frac{m_T \cosh \rho}{T} \right) = \int_0^\infty \cosh y \exp \left( -\frac{m_T \cosh y \cosh \rho}{T} \right) dy, \quad (7)$$

$$I_0 \left( \frac{p_T \sinh \rho}{T} \right) = \frac{1}{2\pi} \int_0^{2\pi} \exp \left( \frac{p_T \sinh \rho \cos \phi}{T} \right) d\phi. \quad (8)$$

Here,  $\rho$  is a parameter given by  $\rho = \tanh^{-1} \beta$ .  $\beta = \beta_{\max} (\xi)^n$  [22, 60–62] is the radial flow, where  $\beta_{\max}$  is the maximum surface velocity and  $\xi = (r/R_0)$  with  $r$  as the radial distance. In the BGBW model, the particles closer to the center of the fireball move slower than the ones at the edges and the average of the transverse velocity can be evaluated as [63]

$$\langle \beta \rangle = \frac{\int \beta_{\max} \xi^n \xi d\xi}{\int \xi d\xi} = \left( \frac{2}{2+n} \right) \beta_{\max}. \quad (9)$$

In our calculation, for the sake of simplicity, we use a linear velocity profile, i.e.,  $n=1$ , and  $R_0$  is the

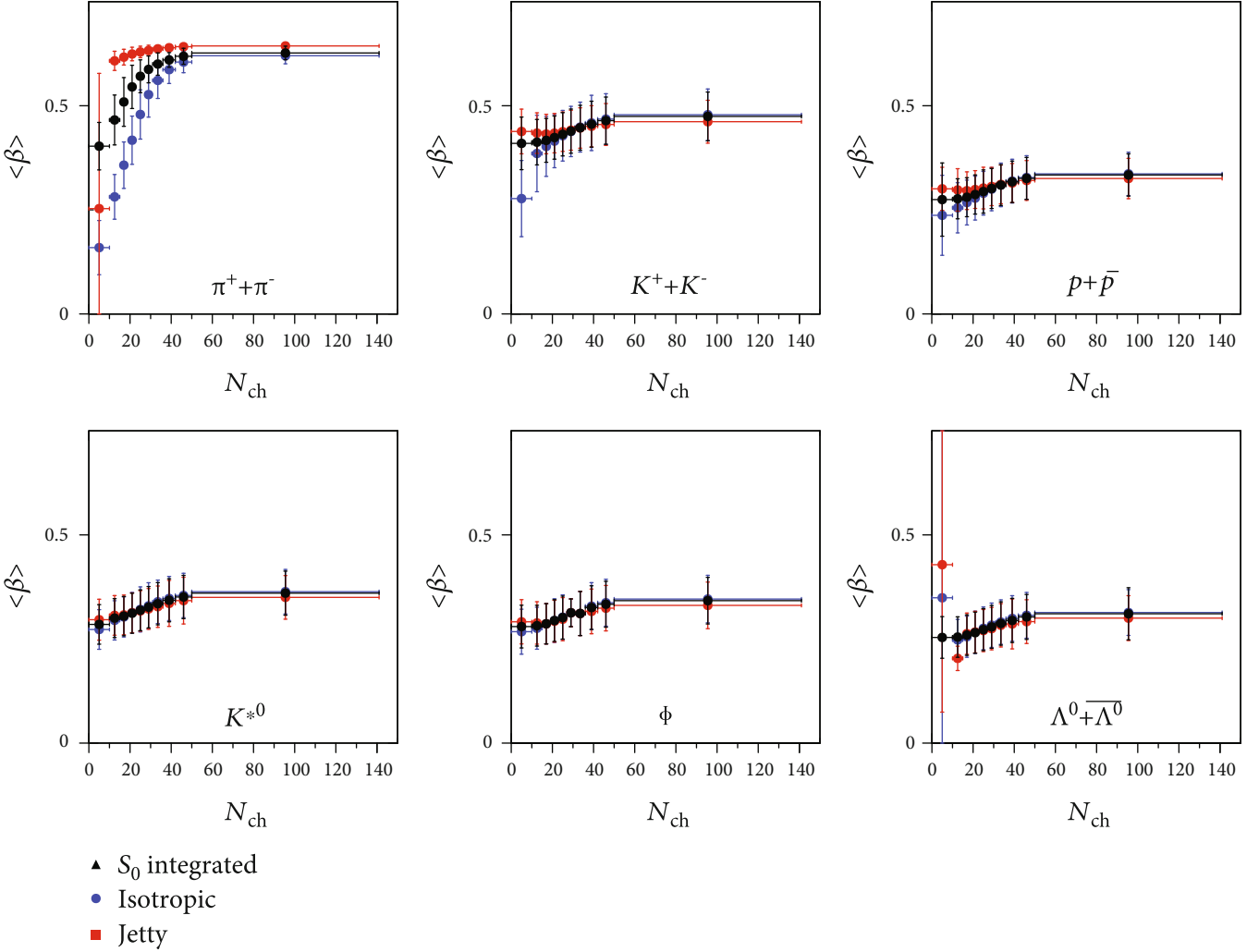


FIGURE 16: (Color online) Multiplicity dependence of  $\langle\beta\rangle$  in different sphericity classes from the fitting of the BGBW model.

maximum radius of the expanding source at freeze-out ( $0 < \xi < 1$ ).

Figures 11–13 show the fitting of  $p_T$ -spectra of pions, kaons, protons,  $K^{*0}$ ,  $\phi$ , and  $\Lambda$  as a function of charged-particle multiplicity using BGBW distribution using Eq. (6) for sphericity-integrated, isotropic, and jetty events, respectively. The BGBW distribution fits the spectra for identified hadrons till  $p_T \approx 2$  GeV/c. Figure 14 shows the  $\chi^2/\text{NDF}$  for the fitting of generated  $p_T$ -spectra of identified hadrons using BGBW model in different sphericity and multiplicity classes. For pions, the  $\chi^2/\text{NDF}$  is relatively lower compared to kaons and protons, indicating pions are better described by the BGBW model. The decrease of  $\chi^2/\text{NDF}$  for pions with increasing charged-particle multiplicity is due to the fact that the number of particles is less in the lower multiplicity classes, which makes the fitting worse. As expected, the fitting for jetty events is worse compared to isotropic and sphericity-integrated events, indicating that the jetty events remain far from equilibrium and a BGBW description, hence, becomes less significant.

It is interesting to note that since BGBW analysis is in the soft sector of particle production, as expected, we do not see any difference between jetty, isotropic, and sphericity-integrated events so far the multiplicity dependence of kinetic freeze-out temperature and the radial flow velocity are concerned, except pions. This is depicted in Figures 15 and 16. For all the discussed particles except the pions, the kinetic freeze-out temperature shows a linear increase with final state multiplicity. The radial flow velocity also shows a monotonic increase with multiplicity class for all the particles. Taking the highest multiplicity class, let us now look into the particle mass dependence of the freeze-out parameters. Figure 17 shows that the temperature increases with mass for the highest multiplicity pp collisions, indicating a differential freeze-out scenario. As seen in the previous subsection, the temperature from the BGBW model also suggests that the particles with heavier mass freeze-out early in time. The radial flow velocity is seen to decrease with particle mass, which supports a hydrodynamical behavior. We observe  $\langle\beta\rangle \approx 0.62$  for pions, whereas it is 0.31 for  $\Lambda$ .

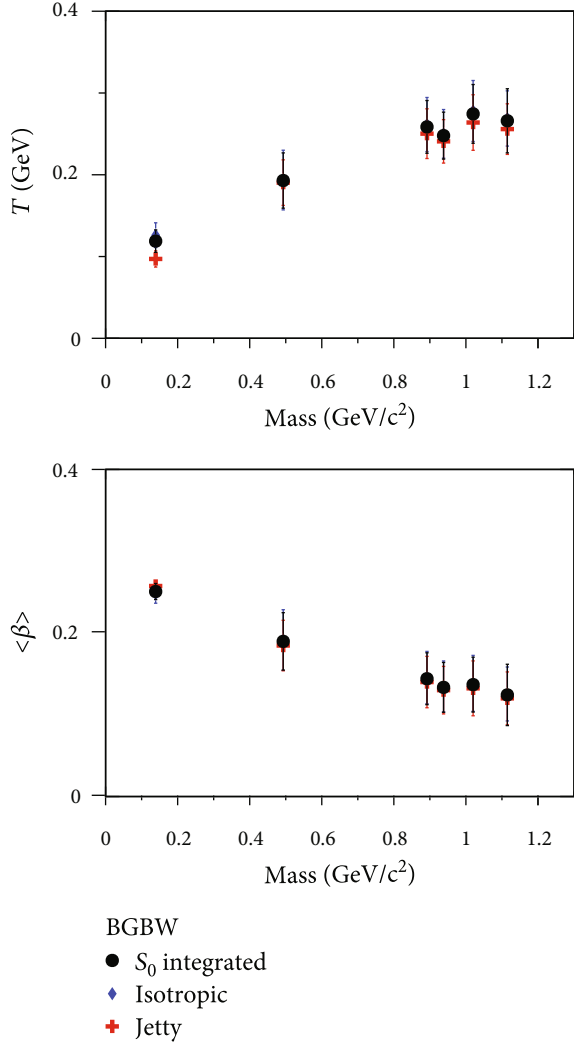


FIGURE 17: (Color online) Mass dependence of  $T$  and  $\langle\beta\rangle$  in different sphericity classes for the highest multiplicity class using BGBW fit up to  $p_T \sim 2 \text{ GeV}/c$ .

#### 4. Summary and Conclusion

We perform a double differential study of the identified particle spectra and the system thermodynamics as a function of charged-particle multiplicity and transverse sphericity in pp collisions at  $\sqrt{s} = 13 \text{ TeV}$  using PYTHIA8. In order to understand the production dynamics of particles in high-multiplicity pp collisions, an event shape-dependent study becomes inevitable. Furthermore, to study the event topology dependence of the kinetic freeze-out properties, we have taken a cosmological expansion scenario of the produced fireball with a differential particle freeze-out. This work would shed light into the underlying event dynamics and help in understanding the possible differences and/or similarities in freeze-out parameters, when the hadronic collisions are compared with heavy-ion collisions. For the analysis of the identified particle  $p_T$ -spectra as a function of charged-particle multiplicity and trans-

verse sphericity, we use the thermodynamically consistent and experimentally motivated Tsallis nonextensive distribution function. In the soft sector of particle production, which corresponds to low- $p_T$ , Boltzmann-Gibbs Blast-Wave (BGBW) model is used to extract the kinetic freeze-out temperature and the radial flow velocity to study the particle mass and event multiplicity dependence. The important findings of this work are summarized below:

- (i) We observe that the temperature parameter obtained by fitting the full range of the  $p_T$ -spectra using Tsallis distribution function is dependent on sphericity class, and it increases with multiplicity for isotropic events, showing a steeper increase for higher mass particles
- (ii) The entropic parameter  $q$  is found to be sphericity and multiplicity dependent. The jetty events have a tendency of staying away from equilibrium. For isotropic events, the  $q$  values remain lower compared to the sphericity-integrated events, which suggests that isotropic events approach more towards equilibrium compared to sphericity-integrated events. This hints for separating isotropic events from sphericity-integrated ones while studying the QGP-like conditions in small systems. This is because the production dynamics are different. In addition, while taking pp collisions as the baseline measurement to study any possible system formation in heavy-ion collisions at the LHC energies, the technique of transverse sphericity would be very useful
- (iii) From BGBW analysis, it is observed that the higher mass particles show higher freeze-out temperature, which is an indication of a differential freeze-out scenario
- (iv) The radial flow velocity is found to be mass dependent: higher for lighter mass particles—an indication of a hydrodynamic behavior in small systems. The obtained average flow velocities indicate a substantial collectivity in small systems in high multiplicity pp events at the LHC energies
- (v) The kinetic freeze-out temperature and the radial flow velocity obtained in the BGBW framework are observed to be independent of sphericity class, except for pions

The present study is very useful in understanding the microscopic features of degrees of equilibration and their dependencies on the number of particles in the system and on the geometrical shape of an event. In the absence of sphericity-dependent experimental data, the present study should give an outlook on similarities/differences between jetty and isotropic events in LHC pp events and their multiplicity dependence. This will help in making a proper bridge in understanding the particle production from hadronic to heavy-ion collisions.

## Data Availability

The paper is based on an event generator baseline study paving a way to do similar analysis in experimental data. Data will not be deposited.

## Conflicts of Interest

The authors declare that they have no conflicts of interest.

## Acknowledgments

The authors acknowledge the financial supports from ALICE Project No. SR/MF/PS-01/2014-IITI(G) of Department of Science & Technology, Government of India. ST acknowledges the financial support by DST-INSPIRE program of the Government of India. RS acknowledges the financial supports from DAE-BRNS Project No. 58/14/29/2019-BRNS of Government of India. Fruitful discussions with Suman Deb and Rutuparna Rath are highly appreciated. The authors would like to acknowledge the usage of resources of the LHC grid computing facility at VECC, Kolkata.

## References

- [1] J. C. Collins and M. J. Perry, "Superdense matter: neutrons or asymptotically free quarks?," *Physical Review Letters*, vol. 34, no. 21, pp. 1353–1356, 1975.
- [2] N. Cabibbo and G. Parisi, "Exponential hadronic spectrum and quark liberation," *Physics Letters B*, vol. 59, no. 1, pp. 67–69, 1975.
- [3] ALICE Collaboration, "Enhanced production of multi-strange hadrons in high-multiplicity proton–proton collisions," *Nature Physics*, vol. 13, pp. 535–539, 2017.
- [4] S. Tripathy and ALICE Collaboration, "Energy dependence of  $\phi$  (1020) production at mid-rapidity in pp collisions with ALICE at the LHC," *Nuclear Physics A*, vol. 982, pp. 180–182, 2019.
- [5] A. K. Dash and ALICE Collaboration, "Multiplicity dependence of strangeness and hadronic resonance production in pp and p-Pb collisions with ALICE at the LHC," *Nuclear Physics A*, vol. 982, pp. 467–470, 2019.
- [6] A. Khuntia, H. Sharma, S. Kumar Tiwari, R. Sahoo, and J. Cleymans, "Radial flow and differential freeze-out in proton-proton collisions at  $\sqrt{s} = 7$  TeV at the LHC," *European Physical Journal A: Hadrons and Nuclei*, vol. 55, no. 1, p. 3, 2019.
- [7] A. Khuntia, S. Tripathy, A. Bisht, and R. Sahoo, "Event shape engineering and multiplicity dependent study of identified particle production in proton+proton collisions at  $\sqrt{s} = 13$  TeV using PYTHIA8," *Journal of Physics G: Nuclear and Particle Physics*, vol. 48, article 035102, 2021.
- [8] A. Ortiz Velasquez, P. Christiansen, E. Cuautle Flores, I. Maldonado Cervantes, and G. Paic, "Color reconnection and flowlike patterns in pp collisions," *Physical Review Letters*, vol. 111, no. 4, article 042001, 2013.
- [9] A. Khatun, D. Thakur, S. Deb, and R. Sahoo, "J/ψ production dynamics: event shape, multiplicity and rapidity dependence in proton+proton collisions at LHC energies using PYTHIA8," *Journal of Physics G: Nuclear and Particle Physics*, vol. 47, no. 5, article 055110, 2020.
- [10] T. Sjöstrand, S. Mrenna, and P. Z. Skands, "PYTHIA 6.4 physics and manual," *Journal of High Energy Physics*, vol. 605, p. 26, 2006.
- [11] P. Skands, S. Carrazza, and J. Rojo, "Tuning PYTHIA 8.1: the Monash 2013 tune," *European Physical Journal C: Particles and Fields*, vol. 74, no. 8, p. 3024, 2014.
- [12] Pythia8, <http://home.thep.lu.se/Pythia/>.
- [13] ALICE Collaboration, "Performance of the ALICE experiment at the CERN LHC," *International Journal of Modern Physics A*, vol. 29, article 1430044, 2014.
- [14] E. Cuautle, R. Jimenez, I. Maldonado, A. Ortiz, G. Paic, and E. Perez, "Disentangling the soft and hard components of the pp collisions using the sphero(i)city approach," <http://arxiv.org/abs/1404.2372>.
- [15] A. Ortiz, G. Paic, and E. Cuautle, "Mid-rapidity charged hadron transverse sphericity in pp collisions simulated with Pythia," *Nuclear Physics A*, vol. 941, pp. 78–86, 2015.
- [16] A. Ortiz, "Experimental results on event shapes at hadron colliders," *Advanced Series on Directions in High Energy Physics*, vol. 29, p. 343, 2018.
- [17] G. P. Salam, "Towards jetography," *European Physical Journal C: Particles and Fields*, vol. 67, no. 3-4, pp. 637–686, 2010.
- [18] G. Bencédi and ALICE Collaboration, "Event-shape-and multiplicity-dependent identified particle production in pp collisions at 13 TeV with ALICE at the LHC," *Nuclear Physics A*, vol. 982, pp. 507–510, 2019.
- [19] ALICE Collaboration, "Pseudorapidity and transverse-momentum distributions of charged particles in proton–proton collisions at  $\sqrt{s} = 13$  TeV," *Physics Letters B*, vol. 753, pp. 319–329, 2016.
- [20] J. Cleymans and D. Worku, "The Tsallis distribution in proton–proton collisions at  $\sqrt{s} = 0.9$  TeV at the LHC," *Journal of Physics G: Nuclear and Particle Physics*, vol. 39, no. 2, article 025006, 2012.
- [21] F. Cooper and G. Frye, "Single-particle distribution in the hydrodynamic and statistical thermodynamic models of multiparticle production," *Physical Review D*, vol. 10, no. 1, pp. 186–189, 1974.
- [22] E. Schnedermann, J. Sollfrank, and U. W. Heinz, "Thermal phenomenology of hadrons from 200AGeV S+S collisions," *Physical Review C*, vol. 48, no. 5, pp. 2462–2475, 1993.
- [23] R. Hagedorn, "Statistical thermodynamics of strong interactions at high energies," *Il Nuovo Cimento*, vol. 3, pp. 147–186, 1965.
- [24] C. Michael and L. Vanryckeghem, "Consequences of momentum conservation for particle production at large transverse momentum," *Journal of Physics G: Nuclear Physics*, vol. 3, no. 8, pp. L151–L156, 1977.
- [25] C. Michael, "Large transverse momentum and large mass production in hadronic interactions," *Progress in Particle and Nuclear Physics*, vol. 2, pp. 1–39, 1979.
- [26] UA1 Collaboration, "Transverse momentum spectra for charged particles at the CERN proton-antiproton collider," *Physics Letters B*, vol. 118, no. 1-3, p. 167, 1982.
- [27] R. Hagedorn, "Multiplicities,  $p_T$  distributions and the expected hadron→quark-gluon phase transition," *La Rivista del Nuovo Cimento*, vol. 6, no. 10, p. 1, 1983.
- [28] STAR Collaboration, "Strange particle production in p + p collisions at  $\sqrt{s} = 200$  GeV," *Physical Review C*, vol. 75, article 064901, 2007.

- [29] PHENIX Collaboration, “Identified charged hadron production in  $p + p$  collisions at  $\sqrt{s} = 200$  and 62.4 GeV,” *Physical Review C*, vol. 83, article 064903, 2011.
- [30] ALICE Collaboration, “Production of pions, kaons and protons in pp collisions at  $\sqrt{s} = 900$  GeV with ALICE at the LHC,” *The European Physical Journal C*, vol. 71, article 1655, 2011.
- [31] ALICE Collaboration, “Neutral pion and  $\eta$  meson production in proton–proton collisions at  $\sqrt{s} = 0.9$  TeV and  $\sqrt{s} = 7$  TeV,” *Physics Letters B*, vol. 717, no. 1-3, pp. 162–172, 2012.
- [32] ALICE Collaboration, “Multi-strange baryon production in pp collisions at  $\sqrt{s} = 7$  TeV with ALICE,” *Physics Letters B*, vol. 712, p. 309, 2012.
- [33] ALICE Collaboration, “Study of the inclusive production of charged pions, kaons, and protons in pp collisions at  $\sqrt{s} = 0.9, 2.76,$  and 7 TeV,” *The European Physical Journal C*, vol. 72, article 2164, 2012.
- [34] T. Bhattacharyya, P. Garg, R. Sahoo, and P. Samantray, “Time evolution of temperature fluctuation in a non-equilibrated system,” *European Physical Journal A: Hadrons and Nuclei*, vol. 52, no. 9, p. 283, 2016.
- [35] T. Bhattacharyya, J. Cleymans, A. Khuntia, P. Pareek, and R. Sahoo, “Radial flow in non-extensive thermodynamics and study of particle spectra at LHC in the limit of small ( $q - 1$ ),” *European Physical Journal A: Hadrons and Nuclei*, vol. 52, no. 2, p. 30, 2016.
- [36] H. Zheng and L. Zhu, “Can Tsallis distribution fit all the particle spectra produced at RHIC and LHC?,” *Advances in High Energy Physics*, vol. 2015, Article ID 180491, 9 pages, 2015.
- [37] Z. Tang, Y. Xu, L. Ruan, G. van Buren, F. Wang, and Z. Xu, “Spectra and radial flow in relativistic heavy ion collisions with Tsallis statistics in a blast-wave description,” *Physical Review C*, vol. 79, no. 5, article 051901, 2009.
- [38] B. De, “Non-extensive statistics and understanding particle production and kinetic freeze-out process from  $p_T$ -spectra at 2.76 TeV,” *European Physical Journal A: Hadrons and Nuclei*, vol. 50, no. 9, p. 138, 2014.
- [39] I. Bediaga, E. M. F. Curado, and J. M. de Miranda, “A nonextensive thermodynamical equilibrium approach in  $e^+e^- \rightarrow$  hadrons,” *Physica A*, vol. 286, no. 1-2, pp. 156–163, 2000.
- [40] G. Wilk and Z. Włodarczyk, “Quasi-power law ensembles,” *Acta Physica Polonica B*, vol. 46, no. 6, article 1103, 2015.
- [41] K. Ürmössy, G. G. Barnaföldi, and T. S. Biró, “Generalised Tsallis statistics in electron–positron collisions,” *Physics Letters B*, vol. 701, no. 1, pp. 111–116, 2011.
- [42] K. Ürmössy, G. G. Barnaföldi, and T. S. Biró, “Microcanonical jet-fragmentation in proton–proton collisions at LHC energy,” *Physics Letters B*, vol. 718, no. 1, pp. 125–129, 2012.
- [43] P. K. Khandai, P. Sett, P. Shukla, and V. Singh, “Hadron spectra in  $p+p$  collisions at RHIC and LHC energies,” *International Journal of Modern Physics A*, vol. 28, no. 16, article 1350066, 2013.
- [44] B.-C. Li, Y.-Z. Wang, and F.-H. Liu, “Formulation of transverse mass distributions in Au–Au collisions at  $\sqrt{s_{NN}} = 200$  GeV/nucleon,” *Physics Letters B*, vol. 725, no. 4-5, pp. 352–356, 2013.
- [45] L. Marques, J. Cleymans, and A. Deppman, “Description of high-energy pp collisions using Tsallis thermodynamics: transverse momentum and rapidity distributions,” *Physical Review D*, vol. 91, article 054025, 2015.
- [46] PHENIX collaboration, “Measurement of neutral mesons in  $p + p$  collisions at  $\sqrt{s} = 200$  GeV and scaling properties of hadron production,” *Physical Review D*, vol. 83, article 052004, 2011.
- [47] ALICE collaboration, “Transverse momentum spectra of charged particles in proton–proton collisions at  $\sqrt{s} = 900$  GeV with ALICE at the LHC,” *Physics Letters B*, vol. 693, no. 2, pp. 53–68, 2010.
- [48] ALICE collaboration, “Production of pions, kaons and protons in pp collisions at  $\sqrt{s} = 200$  GeV with ALICE at the LHC,” *The European Physical Journal C*, vol. 71, article 1655, 2011.
- [49] CMS collaboration, “Transverse-momentum and pseudorapidity distributions of charged hadrons in pp collisions at  $\sqrt{s} = 0.9$  and 2.36 TeV,” *Journal of High Energy Physics*, vol. 2, p. 41, 2010.
- [50] CMS collaboration, “Transverse-momentum and pseudorapidity distributions of charged hadrons in pp collisions at  $\sqrt{s} = 7$  TeV,” *Physical Review Letters*, vol. 105, article 022002, 2010.
- [51] ATLAS collaboration, “Charged-particle multiplicities in pp interactions measured with the ATLAS detector at the LHC,” *New Journal of Physics*, vol. 13, article 053033, 2011.
- [52] ALICE collaboration, “Pion, kaon, and proton production in central Pb-Pb collisions at  $\sqrt{s_{NN}} = 2.76$  TeV,” *Physical Review Letters*, vol. 109, article 252301, 2012.
- [53] S. Grigoryan, “Using the Tsallis distribution for hadron spectra in pp collisions: pions and quarkonia at  $\sqrt{s} = 5$ –13000 GeV,” *Physical Review D*, vol. 95, no. 5, article 056021, 2017.
- [54] A. S. Parvan, O. V. Teryaev, and J. Cleymans, “Systematic comparison of Tsallis statistics for charged pions produced in pp collisions,” *European Physical Journal A: Hadrons and Nuclei*, vol. 53, no. 5, p. 102, 2017.
- [55] J. Cleymans, G. I. Lykasov, A. S. Parvan, A. S. Sorin, O. V. Teryaev, and D. Worku, “Systematic properties of the Tsallis distribution: energy dependence of parameters in high energy p-p collisions,” *Physics Letters B*, vol. 723, no. 4-5, pp. 351–354, 2013.
- [56] C. Tsallis, *Introduction to Nonextensive Statistical Mechanics*, Springer, 2009.
- [57] C. Beck, “Superstatistics: theory and applications,” *Continuum Mechanics and Thermodynamics*, vol. 16, no. 3, pp. 293–304, 2004.
- [58] G. Wilk and Z. Włodarczyk, “Interpretation of the nonextensivity parameter  $q$  in some applications of Tsallis statistics and Lévy distributions,” *Physical Review Letters*, vol. 84, no. 13, pp. 2770–2773, 2000.
- [59] J. D. Bjorken, “Highly relativistic nucleus-nucleus collisions: the central rapidity region,” *Physical Review D*, vol. 27, no. 1, pp. 140–151, 1983.
- [60] P. Huovinen, P. F. Kolb, U. W. Heinz, P. V. Ruuskanen, and S. A. Voloshin, “Radial and elliptic flow at RHIC: further predictions,” *Physics Letters B*, vol. 503, no. 1-2, pp. 58–64, 2001.
- [61] P. Braun-Munzinger, J. Stachel, J. P. Wessels, and N. Xu, “Thermal equilibration and expansion in nucleus-nucleus collisions at the AGS,” *Physics Letters B*, vol. 344, p. 43, 1995.
- [62] Z.-B. Tang, L. Yi, L.-J. Ruan et al., “The statistical origin of constituent-quark scaling in QGP hadronization,” *Chinese Physics Letters*, vol. 30, no. 3, article 031201, 2013.
- [63] PHENIX Collaboration, “Single identified hadron spectra from  $\sqrt{s_{NN}} = 130$  GeV Au+Au collisions,” *Physical Review C*, vol. 69, article 024904, 2004.